

AALBORG UNIVERSITY ESBJERG

Modelling of a Two Phase Water Hammer

M.Sc. Thesis

PECT10-1-F18

7/6/2018



AALBORG UNIVERSITY
STUDENT REPORT



AALBORG UNIVERSITY
STUDENT REPORT

Title:

Modelling of a Two Phase Water Hammer

Theme:

Master's Thesis

Project period:

Spring Semester 2018

Project group:

PECT10-1-F18

Members:

Jensen, Rune Kjerrumgaard
Larsen, Jesper Kær
Lassen, Kasper Lindgren

Supervisor:

Matthias Mandø

Contact person:

Anders Andreasen - Rambøll

No. of Pages: 100

No. of Appendix Pages: 41

Total no. of pages: 149

Completed: 07-06/18

Abstract:

A two phase water hammer has been simulated with Method of Characteristics (MOC) and Computational Fluid Dynamics (CFD). MOC is performed in 1D with the Discrete Vapour Cavity Model (DVCM) and the Discrete Gas Cavity Model (DGCM). The CFD model is performed in 2D with an axisymmetric pipe. MOC and CFD are compared with 4 different experiments found from literature, which covers a range of different dimensions and flow conditions. The Rayleigh-Plesset equation was investigated with the purpose of implementation in MOC, but because of time step size complications and time limitations, this did not succeed. DGCM was found as the overall best two phase water hammer model, as it gave an accurate estimation of the pressure, robustness with large void fractions, and an accurate estimation of the timing of the oscillation.

CONTENTS

1. Previous and Continued Work	1
1.1. Report reading	1
2. Water Hammer Phenomenon	2
3. Cavitation	4
4. Experiments	7
4.1. Soares et al. (Case 1 and 2)	7
4.2. Bergant et al. (Case 3 and 4)	9
5. 1D Modelling of Water Hammer	12
5.1. Method of Characteristics	12
5.2. Grid Type	17
5.3. Friction models	18
6. CFD Modelling of Single Phase Flow	23
6.1. Continuity Equation	23
6.2. Momentum Equation	23
6.3. Turbulence Models	23
6.4. CFD Simulation of Single Phase Water Hammer	25
7. Modelling of a Two Phase Flow using the Method of Characteristics	30
7.1. Discrete Vapour Cavity Model	33
7.2. Discrete Gas Cavity Model	35
7.3. MOC Settings - Two Phase Soares	38
7.4. MOC Settings - Two Phase Bergant et al. - Low Velocity	55
7.5. MOC Settings - Two Phase Bergant - High Velocity	61
7.6. MOC Settings - Summary	66
8. 1D Two Phase Water Hammer with Bubble Dynamics	67
8.1. Governing Equations	67
8.2. Bubble Dynamics	67
8.3. Implementation	74
9. CFD Modelling of Two Phase Flow	75
9.1. Multiphase Model	75
9.2. Cavitation Model	76
9.3. CFD Simulation of Soares et al. Experiment	77
9.4. CFD Simulation of Bergant et al. Experiments	82
10. Results	86
10.1. Soares et al. Experiment	86

10.2. Bergant et al. Low Velocity Experiment	89
10.3. Bergant et al. High Velocity Experiment	91
11. Discussion	94
12. Conclusion	97
Bibliography	98
Appendix	101
A. Rayleigh-Plesset Equation Derivation	101
A.1. Mass Conservation	101
A.2. Momentum Conservation	102
A.3. Bubble Boundary Condition	103
B. User Defined Function	104
C. Grid Independency Analysis	105
C.1. Bergant et al. - Low Velocity Experiment	105
C.2. Bergant et al. - High Velocity Experiment	112
D. Matlab code	115

NOMENCLATURE

Symbol	Definition	Unit
A	Cross sectional area	m^2
a	Single phase wave speed	m/s
a'	Two phase wave speed	m/s
B	Pipe constant	s/m^2
c_1	Poisson's ratio dependent constant	–
D	Inner pipe diameter	m
E	Young's modulus	Pa
e	Thickness of the pipe wall	m
f	Darcy's friction factor	–
g	Gravitational acceleration	m/s^2
H	Piezometric head	m
H_r	Piezometric head at the reservoir	m
$i \ \& \ j$	Index notation	–
J	Friction term	m/s^2
K	Bulk modulus	Pa
k	Brunone's friction coefficient or turbulent kinetic energy	– or m^2/s^2
L	Length of the pipe	m
M	Mass transfer rate through the surface	kg/m^3s
m	Mass or closure coefficient	kg or –
N	Bubble number density	$1/m^3$
n	Number of reaches (divisions of the pipes)	–
P	Pressure	Pa
Q	Volumetric flow rate	m^3/s
$R \ \& \ r$	Radius	m
Re	Reynolds number	–
S	Surface tension	N/m
T	Temperature	K
t	Time	s
u	Velocity	m/s
V	Volume	m^3
W	Weighting function	–
x	Spatial coordinate	m
z	Elevation of the pipe from datum	m

GREEK SYMBOLS

Symbol	Definition	Unit
α	Void fraction	–
Δ	Difference	–
ϵ	Rate of dissipation of turbulent kinetic energy	m^2/s^3
θ	Inclination of the pipe	<i>deg</i>
μ	Dynamic viscosity	$kg/m \cdot s$
ν	Kinematic viscosity	m^2/s
ν_p	Poisson's ratio	–
ρ	Density	kg/m^3
τ	Dimensionless time	–
τ_v	Dimensionless closure time	–
ψ	Weighting factor	–
ω	Specific rate of dissipation of turbulent kinetic energy	$1/s$
*	Convolution operator	–

SUBSCRIPTS

Symbol	Definition
A	Node to the left of node P at $t = t - \Delta t$
B	Node to the right of node P at $t = t - \Delta t$
b	Bubble
cav	Vapour cavity
g	Gas
i	Index notation
j	Index notation
l	Liquid
m	Mixture
P	Node of interest
$P0$	Node P at $t = t - 2\Delta t$
qs	Quasi-steady friction term
us	Unsteady friction term
v	Vapour
∞	Reference or far away (ambient)
0	Initial or steady state

1. PREVIOUS AND CONTINUED WORK

On the 9th semester the group did a project in cooperation with Rambøll to write a program to simulate a one dimensional and single phase water hammer. The water hammer was simulated with the Method of Characteristics (MOC) with steady, quasi steady, convolution based and instantaneous acceleration based friction models. The different friction models were compared with three experiments found from literature. The experiments were chosen so that the friction models could be tested under different flow conditions and pipe materials to investigate if one was more reliable than the others and if some performed better under certain conditions. The Vardy & Brown convolution based friction model was found as the overall most accurate when describing the dampening of the pressure and the behaviour of the pressure wave.

An article was written for the internal CES conference at Aalborg University. For the master's thesis project, it was decided with Rambøll to investigate the modelling of water hammer with two phase flow, as it is believed by the authors that cavitation can increase the pressure during a water hammer event, compared to a single phase water hammer. Therefore it is crucial to investigate whether this is the case especially when dimensioning pipe systems.

For the master's thesis project, the MOC program will be extended by analysing the two phase water hammer with two different models: The Discrete Vapour Cavity Model (DVCM) and the Discrete Gas Cavity Model (DGCM). As the DVCM and DGCM models do not use bubble dynamics for calculating the vapour fraction, the Rayleigh-Plesset equation (bubble equation) will be analysed for the possibility of implementation in the MOC program. Also, a two dimensional axisymmetric Computational Fluid Dynamics (CFD) simulation is constructed to simulate a two phase water hammer. The results obtained from the DVCM, DGCM, Rayleigh-Plesset equation, and CFD will be compared with experiments found from literature to analyse which model is most accurate for an estimation of a two phase water hammer.

1.1. REPORT READING

The report has been divided into sections to give an overview of the different simulation methods and experiments. First an introduction of a single phase water hammer followed by an introduction into the basics of cavitation and its mechanisms during a water hammer event are presented. Then the experiments, that the models will be compared to, and the results from these are presented. Then the report is effectively split up into two parts. First by modelling a single phase water hammer using MOC and CFD. Followed by the modelling of a two phase water hammer using MOC, Rayleigh-Plesset equation, and CFD.

2. WATER HAMMER PHENOMENON

The water hammer phenomenon is generated by a sudden change in flow caused by e.g. a valve closure or a pump failure. This cutoff in flow will cause a sudden change in the momentum of the fluid, causing a pressure wave to travel through the system. This pressure wave can lead to pipe ruptures and/or damages to equipment if comprehensive security measures are not applied.

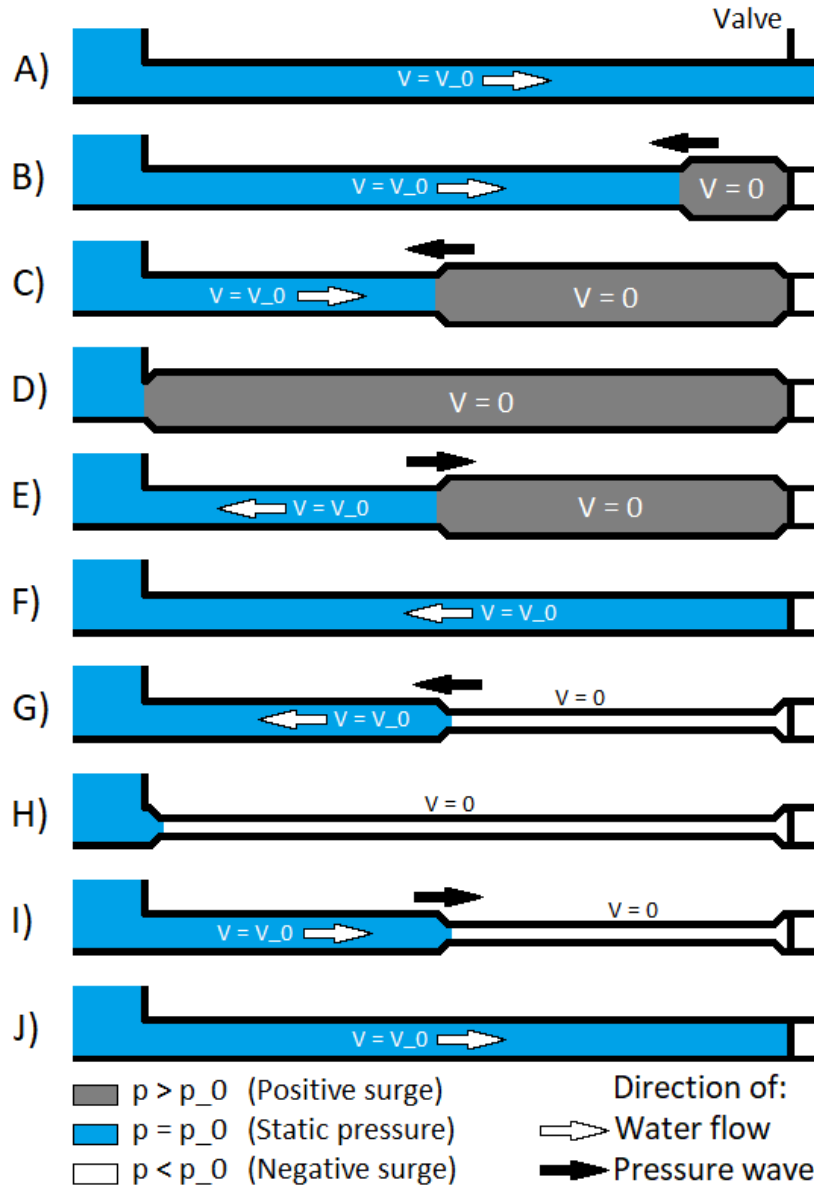


Figure 2.1: Water hammer illustration with instantaneous valve closure. [1]

A pressure wave generated by an instantaneous valve closure, in a horizontal pipe, is illustrated in Fig. 2.1. The setup has a reservoir at the upstream end and a valve at the downstream end.

A) A steady flow through the pipe with the valve open. B) The valve is closed instantaneously generating an increase in pressure. C) The pressure wave moves towards the lower pressure at the reservoir and leaves the water in standstill. D) As there is no momentum to convert into pressure in the reservoir, the pressure wave is reflected back towards the valve. E) The pressure is converted into velocity as the pressure wave is moving towards the valve. The water velocity is negative as the pressure is lower at the reservoir. F) The pressure wave is reflected as it reaches the valve. G) As the pressure wave moves towards the reservoir, the pressure is lowered as the velocity is negative. H) The pressure is reflected at the reservoir again and moves towards the valve. I) The pressure is converted into velocity and as the pressure at the reservoir is higher than the pressure wave, the velocity is positive. J) When the pressure wave has reached the valve again, the pattern restarts from B) and continues until the energy has been dissipated through friction, or the valve is reopened. [2]

The pressure wave is moving with the speed of sound, which is constant during a single phase water hammer. The wave speed, a , can be calculated by Eq. (2.1). [3]

$$a = \sqrt{\frac{K/\rho}{1 + \frac{DK}{eE}c_1}} \quad (2.1)$$

Where ρ is the density of the fluid, e is the thickness of the pipe wall, E is the Young's modulus which relates the stress and strain in the pipe, c_1 is a constant that depends on the anchorage of the pipe, and K is the bulk modulus of the fluid which is a measure of the elasticity of the fluid.

For an anchored pipe that resists longitudinal movement c_1 is calculated with Eq. (2.2) if the ratio $D/e < 25$ and for a pipe where $D/e > 25$ it is calculated with Eq. (2.3). [3]

$$c_1 = \frac{2e}{D}(1 + \nu) + \frac{D(1 - \nu^2)}{D + e} \quad (2.2)$$

$$c_1 = 1 - \nu^2 \quad (2.3)$$

Where ν is Poisson's ratio.

A simple way to approximate the pressure increase is to use the Joukowsky equation, seen in Eq. (2.4) [2].

$$\Delta H = \frac{a\Delta u}{g} \quad (2.4)$$

Where H is the piezometric head, Δu is the change in velocity from steady state, and g is the gravitational acceleration. The Joukowsky equation assumes that the change in velocity happens instantaneously, which should give the highest possible pressure increase, without taking into account cavitation.

3. CAVITATION

If the pressure during the water hammer event reaches or falls below the vapour pressure, vapour bubbles will start to form. This process is known as cavitation. The process of cavitation is characterized by the rupturing of a liquid by decreasing the pressure to the saturated vapour pressure while roughly keeping the temperature constant. For the saturated liquid to become saturated vapour a sufficient amount of nucleation sites with a significant size has to be present.

In practical engineering processes, the rupture of the liquid into vapour often occur at the boundary between the liquid and the solid wall or between the liquid and tiny contaminants in the liquid. This rupture process is called heterogeneous nucleation.

The nucleation sites are the optimum place for growth and appearance of macroscopic bubbles on a solid surface. It is at these sites, when the pressure is lowered, that the bubbles are generated and released to the liquid.

The bubble size can maximum increase in the order of a 100 for a typical cavitating flow [4].

When the bubble collapses, a reentrant jet (microjet) is developed. Where a part of the bubble surface will accelerate inward with a high speed, as seen in Fig. 3.1.

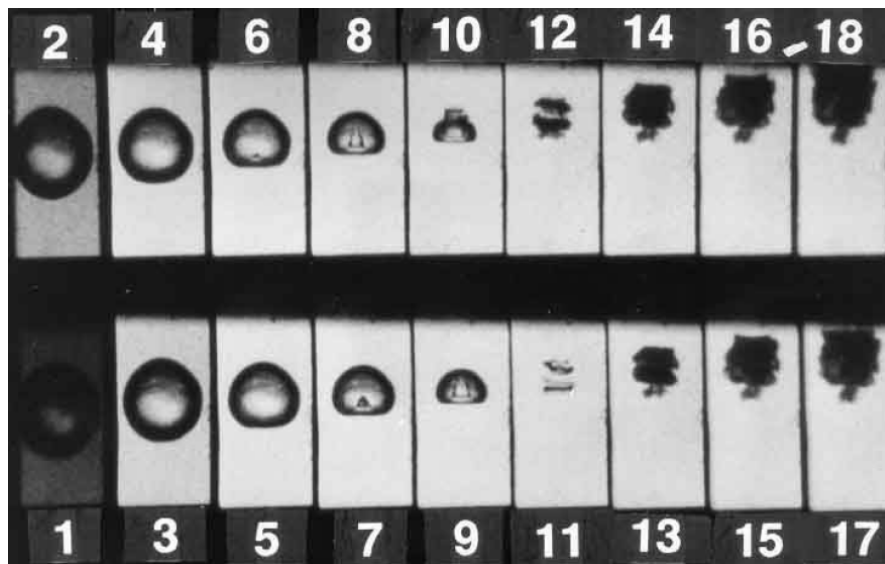


Figure 3.1: Reentrant jet at bubble collapse. [5]

As the bubble collapses, a cloud of smaller bubbles is generated, as seen in picture 11 - 18 in Fig. 3.1. When the bubble collapses it can cause material damages and loud noises caused by high pressure. If the change in pressure is e.g. 0.1bar the maximum pressure of the bubble collapse is about 10^{10} bar (assuming a spherical bubble) [4].

As the microjet collapse occur very localized on the surface, the surface experience very high and transient stresses which could, if repeated, lead to damages to the material. [4] For the water hammer pressure wave with cavitating flow, the high pressure generated by the bubble collapse could lead to an even higher pressure than seen from a single phase water hammer.

Another effect of the formation of vapour cavities, is that the wave speed is decreased and is no longer constant. In Fig. 3.2 the wave speed's dependency on the void fraction of gas is illustrated. It is clear that with increasing gas void fraction there will be a reduction in the wave speed. The reason for this is that the cavities effectively function as springs separating water molecules. This is contrary to water hammer events without cavities where the water molecules would interact directly upon each other causing a greater wave speed.[3]

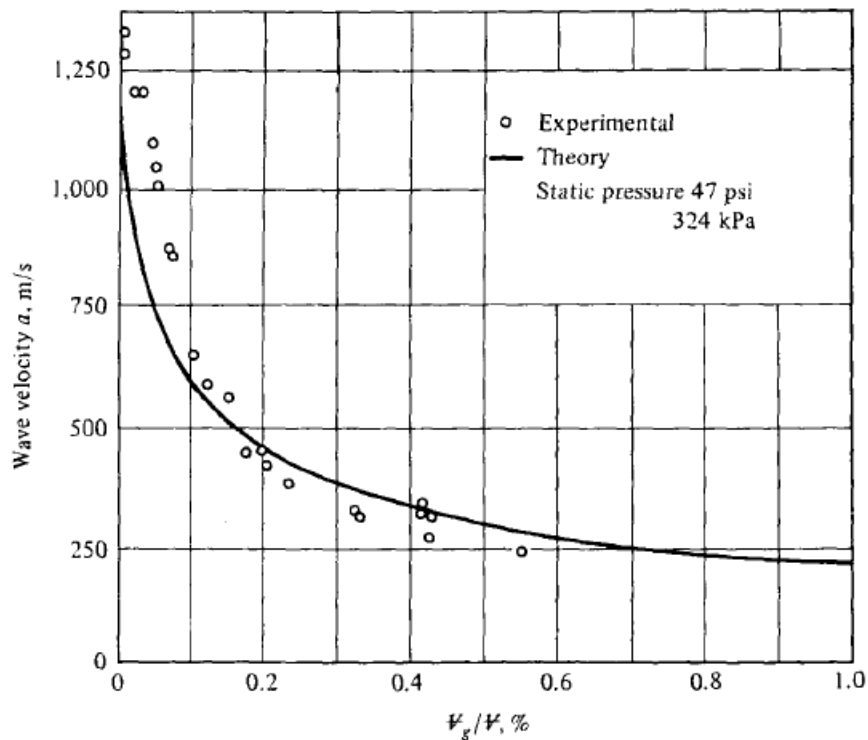


Figure 3.2: Effect of the void fraction of gas on the wavespeed. [3]

It is seen that a water hammer with cavitating flow can cause extreme damages to pipes, joints and foundations. In 1950 at the Oigawa Hydropower Station, Japan, an accident resulted in 3 deaths. During a maintenance of the oil control system a fast closure of a valve caused a high pressure wave to split the penstock. As the penstock split, water was released generating a low pressure wave resulting in column separation (clear separation of liquid and vapour) that made the pipe collapse due to the pressure difference between the pipe and the external atmospheric air. [6] The pipe damages can be seen in Fig. 3.3.

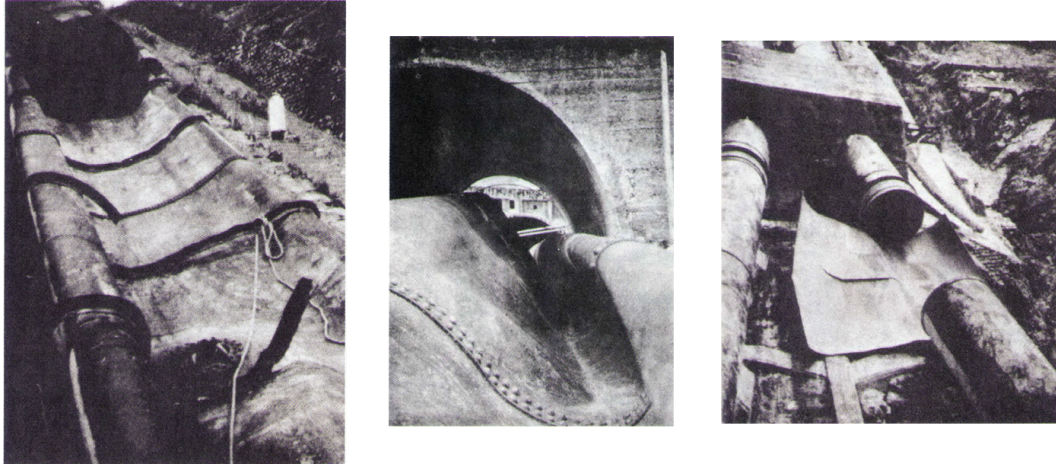


Figure 3.3: Damages to the penstock at Oigawa Hydropower Station, Japan. [6]

In another case a large pipeline test rig at Deltares, the Netherlands, has an automatic control valve at the upstream and downstream of the pipeline. Because of a power failure both control valves closed simultaneously creating a transient event by a down-surge at the upstream end and an upsurge at the downstream end. The closure of the valves caused leakage at the joints and damages to the pipe support, as seen in Fig. 3.4.



Figure 3.4: Water hammer damages at Deltares, the Netherlands. [7]

4. EXPERIMENTS

Four experiments have been found with the same setup: a straight pipe with a reservoir/-tank upstream, a fast closing valve and a reservoir/tank downstream. The experiments have been chosen such that they have different velocities and Reynolds numbers to analyse if this will affect the simulations. The experiments are performed by Soares et al. [8] and Bergant et al. [9]. The experiments are used for comparison of the models to evaluate which model most accurately estimate the pressure and the behaviour of the pressure wave.

4.1. SOARES ET AL. (CASE 1 AND 2)

The experiments performed by Soares et al. [8] consists of a $15.22m$ straight copper pipe with a wall thickness of $1.0mm$ and an internal diameter of $20mm$. The medium is water at room temperature. The experimental setup, as seen in Fig. 4.1, has a hydropneumatic tank at the upstream and a pneumatically actuated quarter turn ball valve at the downstream.

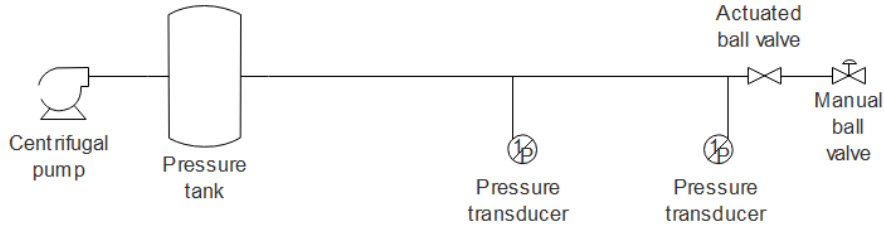


Figure 4.1: Experimental setup. [8]

The closure time is not given by Soares et al. [8]. Therefore the closure time has been determined from the experimental data, and approximated as $18ms$. The Young's modulus of the copper pipe is $120GPa$. The two experiments were conducted with an initial velocity of $0.423m/s$ (Case 1) and $0.497m/s$ (Case 2) respectively. The experiment with the lowest velocity resulted in a single phase water hammer, while the experiment with the highest velocity resulted in a two phase water hammer. The reservoir head of the two experiments was $46m$. The experimental parameters can be seen in Table 4.1.

Table 4.1: Experimental parameters.

Parameter	Value	Parameter	Value
Pipe length	$15.22m$	Case 1 velocity	$0.423m/s$
Wall thickness	$1.0mm$	Case 1 Reynolds number	8428
Pipe internal diameter	$20mm$	Case 2 velocity	$0.497m/s$
Valve closure time	$16.5ms$	Case 2 Reynolds number	9894
Young's modulus	$120GPa$	Reservoir head	$46m$

The experimental results for the single and two phase experiments at the valve is as seen in Fig. 4.2 and 4.3. Note that the pressure is described in gauge piezometric head, i.e. zero meters is equivalent to atmospheric conditions.

The single phase experiment, see Fig. 4.2, shows a typical water hammer event at the valve. The pressure rises from a steady state value until it reaches a maximum pressure. Then after a period of high pressure, a period of low pressure will follow. The pressure will oscillate between high and low pressure with decreasing amplitude due to friction.

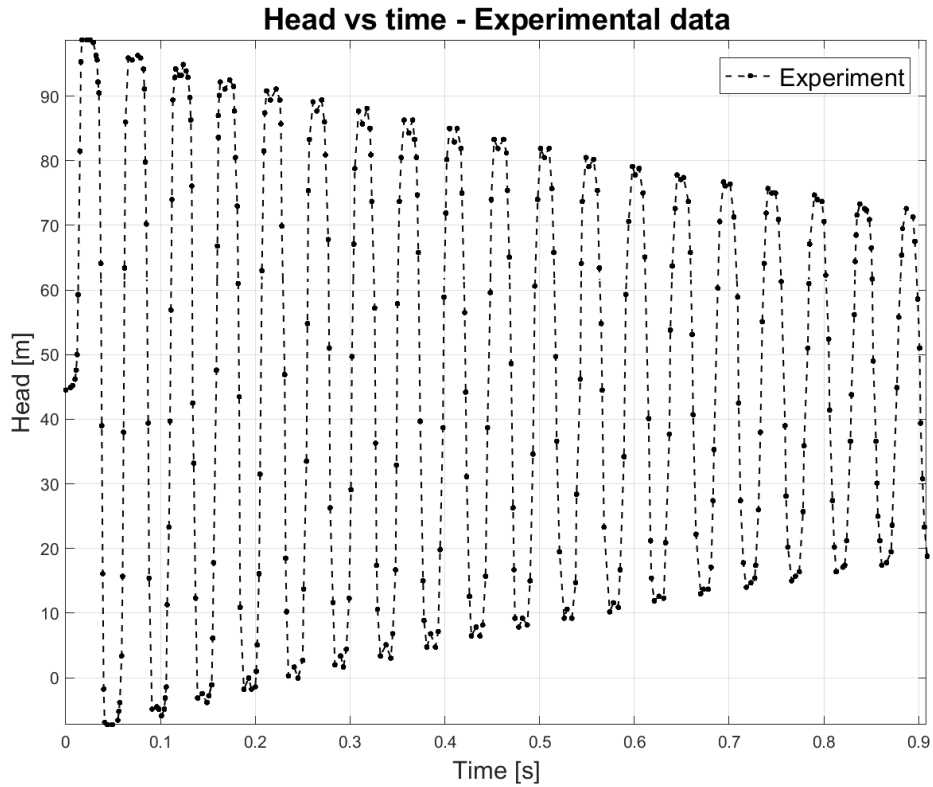


Figure 4.2: Single phase pressure at the valve (Case 1).

The two phase experiment, see Fig. 4.3, will initially resemble a single phase water hammer, but the low pressure will reach the vapour pressure, which will cause the formation of vapour cavities/bubbles. The second pressure peak is higher than the first pressure peak, contrary to the single phase water hammer, because the vapour cavities collapse. These high pressure peaks will be present as long as the low pressure reaches the vapour pressure.

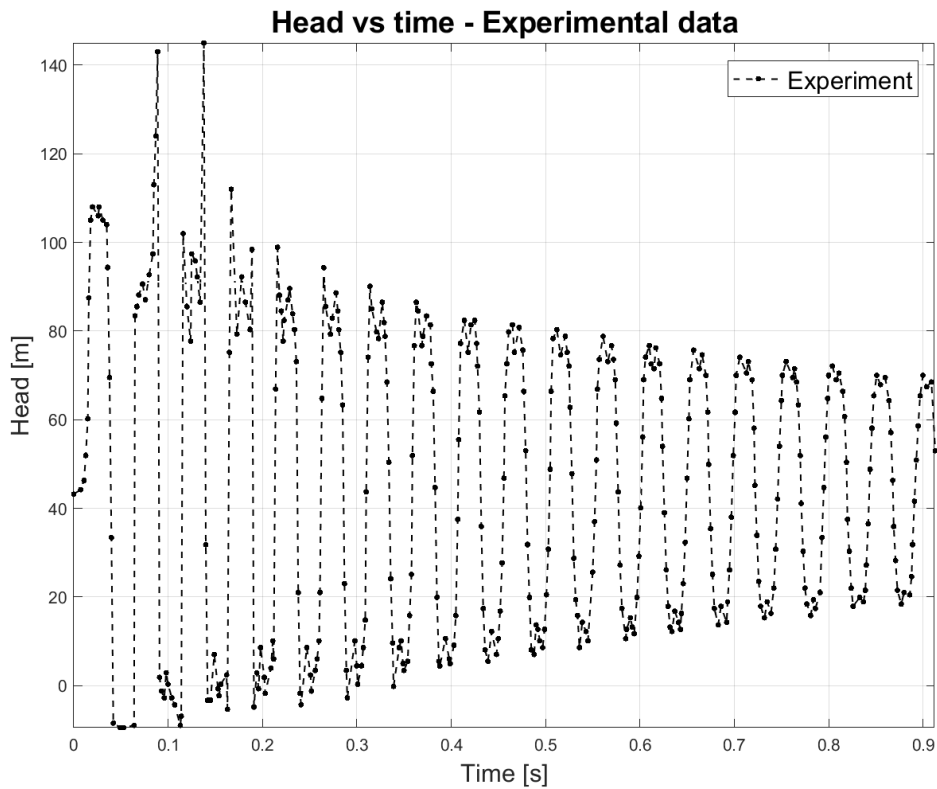


Figure 4.3: Two phase pressure at the valve (Case 2).

4.2. BERGANT ET AL. (CASE 3 AND 4)

The experiments performed by Bergant et al. [9] consists of a 37.23m straight copper pipe with a wall thickness of 1.63mm and an internal diameter of 22.1mm. Water is the working fluid at room temperature.

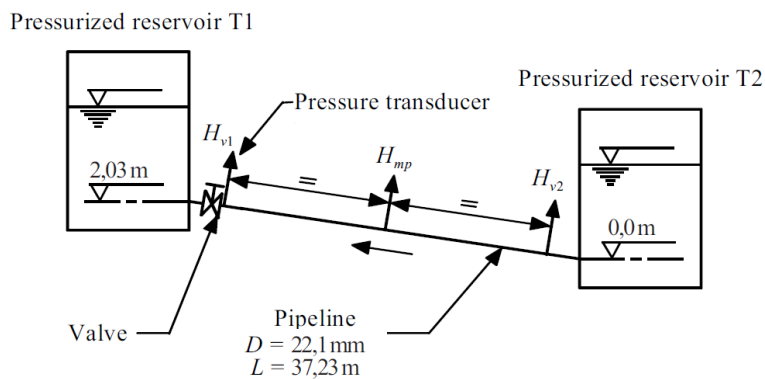


Figure 4.4: Experimental setup for the Bergant et al. experiments. [9]

The experimental setup, as seen in Fig. 4.4, consists of a pressurized tank at the upstream and downstream end of the pipe. The pressurized tanks are controlled by a computerized pressure control system for a precise estimation of the pressure. The pipe has a slope of 5.45% (3.12°). A fast closing ball valve is placed downstream of the pipe for generation of the transient. Two experiments have been carried out with an initial velocity of $0.30m/s$ (Case 3) and $1.40m/s$ (Case 4) with a head at the pressurized tank, T2, of $22m$. The fast valve closure is identical for the two experiments, $0.009s$. The material parameters used is the same as for the Soares et al. [8] experiments as they were not given by Bergant et al. [9] and consist of the same pipe material. The experimental parameters can be seen in Table 4.2.

Table 4.2: Experimental parameters.

Parameter	Value	Parameter	Value
Pipe length	$37.23m$	Case 3 velocity	$0.3m/s$
Wall thickness	$1.63mm$	Case 3 Reynolds number	6605
Pipe internal diameter	$22.1mm$	Case 4 velocity	$1.40m/s$
Pipe slope	3.12°	Case 4 Reynolds number	30823
Valve closure time	$0.009s$	Reservoir head	$22m$

The experimental results for the experiments can be seen in Fig. 4.5 and 4.6, and it can be seen that both experiments are two phase.

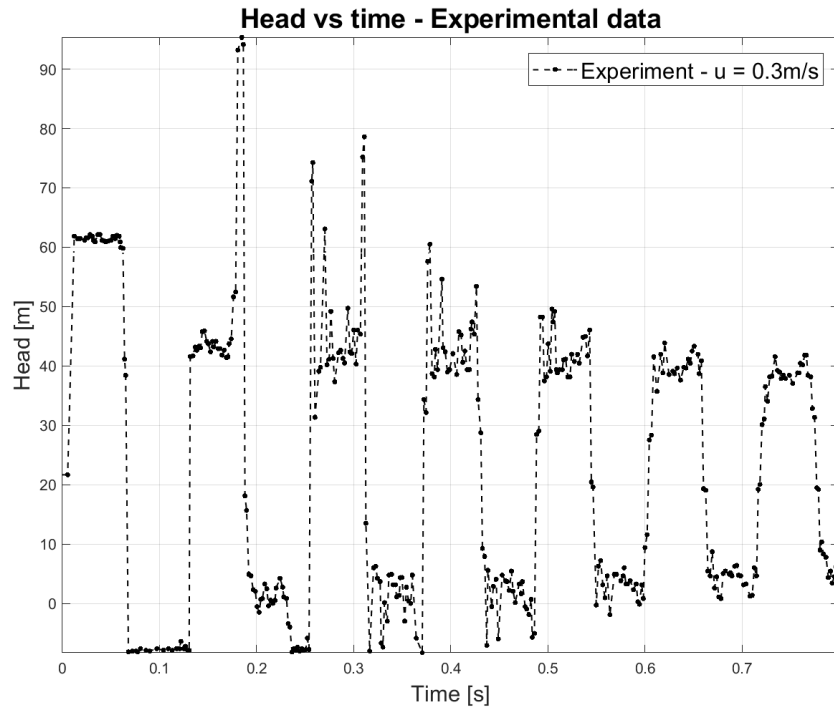


Figure 4.5: Pressure at the valve with an initial velocity of 0.30m/s (Case 3).

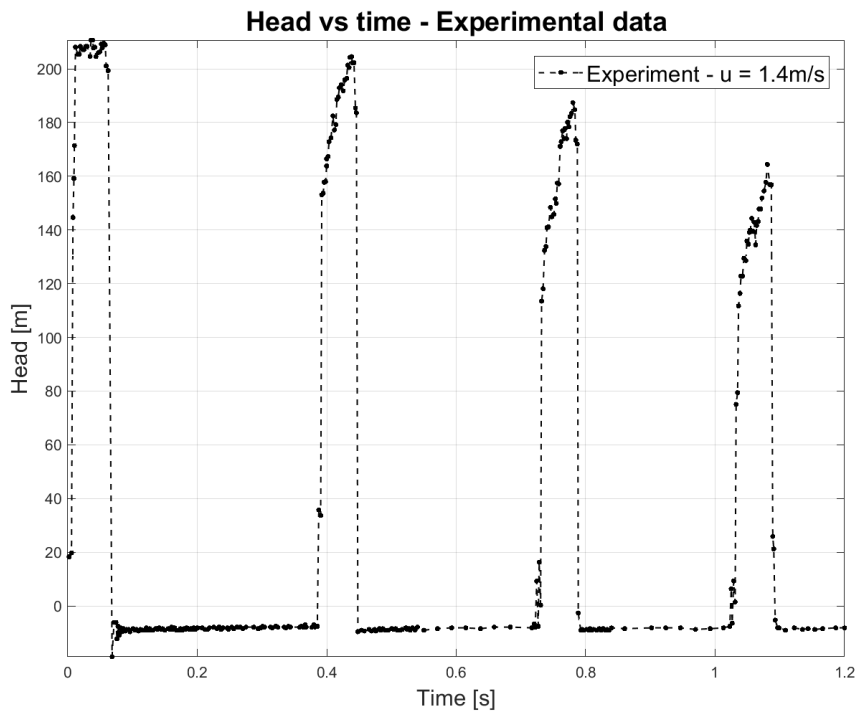


Figure 4.6: Pressure at the valve with an initial velocity of 1.40m/s (Case 4).

5. 1D MODELLING OF WATER HAMMER

The water hammer phenomenon in 1D is described by the continuity and momentum equations in Eq. (5.1) and Eq. (5.2) [3].

$$\frac{1}{\rho} \frac{dP}{dt} + a^2 \frac{\partial u}{\partial x} = 0 \quad (5.1)$$

$$\frac{1}{\rho} \frac{\partial P}{\partial x} + u \frac{\partial u}{\partial x} + \frac{\partial u}{\partial t} + g \sin(\theta) + J = 0 \quad (5.2)$$

In Eq. (5.1) ρ is the density of the fluid which is assumed to be constant, P is the pressure, t the is time, u is the velocity, and x is the spatial coordinate along the center of the pipe. In Eq. (5.2) g is the gravitational acceleration, θ is the inclination of the pipe, and J is the friction term.

The pressure in piezometric head is used and it is defined as in Eq. (5.3).

$$P = \rho g(H - z) \quad (5.3)$$

Where H is the piezometric head and z is the elevation of the pipe. The total derivative of the pressure in Eq. (5.3) can then be expressed as in Eq. (5.4).

$$\frac{dP}{dt} = \rho g \left(\frac{\partial H}{\partial t} + u \frac{\partial H}{\partial x} - \frac{\partial z}{\partial t} - u \frac{\partial z}{\partial x} \right) \quad (5.4)$$

The two last terms in Eq. (5.4) can be replaced with $\frac{\partial z}{\partial x} = \sin(\theta)$, which is the elevation of the pipe, and $\frac{\partial z}{\partial t} = 0$, which is only relevant if the pipe moves. This, plus a conversion of the velocity into the volumetric flow rate, Q , divided by the cross sectional area of the pipe, A , allows Eq. (5.1) and 5.2 to be rewritten into Eq. (5.5) and (5.6) respectively.

$$\frac{\partial H}{\partial t} + \frac{Q}{A} \frac{\partial H}{\partial x} + \frac{a^2}{gA} \frac{\partial Q}{\partial x} - \frac{Q}{A} \sin(\theta) = 0 = L_2 \quad (5.5)$$

$$\frac{\partial Q}{\partial t} + \frac{Q}{A} \frac{\partial Q}{\partial x} + gA \frac{\partial H}{\partial x} + AJ = 0 = L_1 \quad (5.6)$$

5.1. METHOD OF CHARACTERISTICS

MOC is used to solve the continuity equation, Eq. (5.5), and the momentum equation, Eq. (5.6). MOC transforms these equations, which is a set of two partial differential equations (PDEs), into a set of four ordinary differential equations (ODEs). The first step is to combine L_1 and L_2 with an unknown multiplier λ .

$$L = L_1 + \lambda L_2 \quad (5.7)$$

Inserting L_1 and L_2 and then rearranging gives L as in Eq. (5.8).

$$L = \underbrace{\frac{\partial Q}{\partial t} + \left(\frac{Q}{A} + \lambda \frac{a^2}{gA} \right) \frac{\partial Q}{\partial x}}_{=\frac{dQ}{dt}} + \lambda \underbrace{\left(\frac{\partial H}{\partial t} + \left(\frac{Q}{A} + \frac{gA}{\lambda} \right) \frac{\partial H}{\partial x} \right)}_{=\frac{dH}{dt}} + AJ - \lambda \frac{Q}{A} \sin(\theta) \quad (5.8)$$

Since both Q and H is dependent on x and t , their total derivatives are as in Eq. (5.9) and Eq. (5.10).

$$\frac{dQ}{dt} = \frac{\partial Q}{\partial t} + \frac{\partial Q}{\partial x} \frac{dx}{dt} \quad (5.9)$$

$$\frac{dH}{dt} = \frac{\partial H}{\partial t} + \frac{\partial H}{\partial x} \frac{dx}{dt} \quad (5.10)$$

This is substituted into Eq. (5.8), resulting in Eq. (5.11), assuming that the terms multiplied by $\partial Q/\partial x$ and $\partial H/\partial t$ are both equal to dx/dt , as in Eq. (5.12).

$$\frac{dQ}{dt} + \lambda \frac{dH}{dt} + AJ - \lambda \frac{Q}{A} \sin(\theta) = 0 \quad (5.11)$$

$$\frac{dx}{dt} = \frac{Q}{A} + \lambda \frac{a^2}{gA} = \frac{Q}{A} + \frac{gA}{\lambda} \quad (5.12)$$

Then Eq. (5.12) is used to solve for λ and it results in $\lambda = \pm \frac{gA}{a}$. If the positive value of λ is substituted into Eq. (5.11) and (5.12) they give the positive characteristics, C^+ (Eq. (5.13) and (5.14)). Substituting the negative value of λ into Eq. (5.11) and (5.12) give the negative characteristics, C^- (Eq. (5.15) and (5.16)).

$$C^+ : \begin{cases} \frac{dQ}{dt} + \frac{gA}{a} \frac{dH}{dt} + AJ - \frac{gQ}{a} \sin(\theta) = 0 & (5.13) \\ \frac{dx}{dt} = \frac{Q}{A} + a & (5.14) \end{cases}$$

$$C^- : \begin{cases} \frac{dQ}{dt} - \frac{gA}{a} \frac{dH}{dt} + AJ + \frac{gQ}{a} \sin(\theta) = 0 & (5.15) \\ \frac{dx}{dt} = \frac{Q}{A} - a & (5.16) \end{cases}$$

The positive and negative characteristics each consist of two equations. Eq. (5.13) and (5.15) are both valid as long as their respective compatibility equation, Eq. (5.14) and (5.16), holds true.

If $a \gg Q/A$ then Eq. (5.14) and (5.16) can be simplified by dropping Q/A . This corresponds to neglecting the convective terms, i.e. $\frac{Q}{A} \frac{\partial Q}{\partial x}$ and $\frac{Q}{A} \frac{\partial H}{\partial x}$, in Eq. (5.5) and (5.6). This assumption causes the characteristic lines, along which Eq. (5.13) and (5.15) are valid, to be linear with a constant slope of $\pm a$, which is illustrated in Fig. 5.1.

$$\frac{dx}{dt} = \pm a \quad (5.17)$$

To solve Eq. (5.13), (5.15), and (5.17) numerically, finite differences are used. Then Eq. (5.17) can be expressed in finite difference form as in Eq. (5.18).

$$\Delta x = \pm a \Delta t \quad (5.18)$$

For explicit transient solvers it is necessary to have a Courant number, C_o , less or equal to one. The Courant number is defined as the computational time step divided by the time the flow is in a cell as in Eq. (5.19). [10]

$$C_o = \frac{a \Delta t}{\Delta x} \quad (5.19)$$

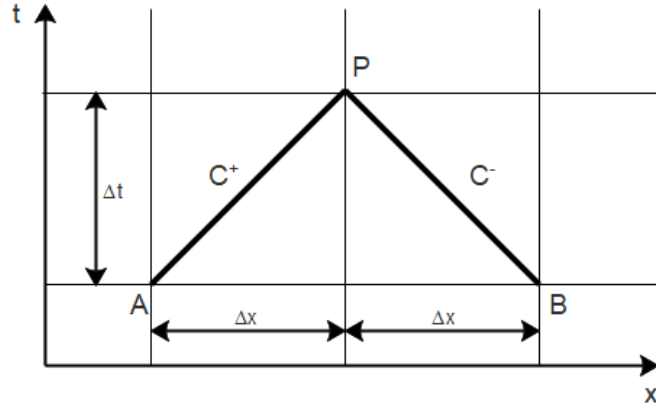


Figure 5.1: Example of characteristic lines with a constant slope in the xt plane.

In MOC the Courant number is equal to one, which can be realized from Eq. (5.18). The desired computational time step is determined by the number of divisions of the pipe, n , and the total travelling time of the pressure wave for the entire length of the pipe, $t_{trav} = L/a$.

$$\Delta t = \frac{t_{trav}}{n} = \frac{L}{na} \quad (5.20)$$

The next step is to approximate Eq. (5.13) and (5.15) with finite differences. The first step is to multiply Eq. (5.13) with $\frac{a}{gA}dt$, as in Eq. (5.21).

$$\frac{a}{gA}dQ + dH + \frac{a}{g}Jdt - \frac{Q}{A}\sin(\theta)dt = 0 \quad (5.21)$$

Since the values of the variables H and Q are known at point A the unknown values at point P can be found by integrating Eq. (5.21) along the positive characteristics line from point A to P , as in Eq. (5.22). This integration of the positive characteristics equation yields Eq. (5.23).

$$\int_{H_A}^{H_P} dH + B \int_{Q_A}^{Q_P} dQ + \frac{a}{g} \int_{t_A}^{t_P} Jdt - \frac{\sin(\theta)}{A} \int_{t_A}^{t_P} Qdt = 0 \quad (5.22)$$

$$H_P - H_A + B(Q_P - Q_A) + \frac{a}{g}J_A\Delta t - \frac{\sin(\theta)}{A}Q_A\Delta t = 0 \quad (5.23)$$

Where $B = \frac{a}{gA}$. Then solving for the head at point P yields the positive characteristics equation, Eq. (5.24).

$$H_P = C_p - BQ_P \quad (5.24)$$

Where

$$C_p = H_A - BQ_A - \frac{a}{g}J_A\Delta t + \frac{\sin(\theta)}{A}Q_A\Delta t \quad (5.25)$$

Similarly integrating from point P to B and solving for the head at point P yields the negative characteristics equation, Eq. (5.26).

$$H_P = C_m - BQ_P \quad (5.26)$$

Where

$$C_m = H_B - BQ_B + \frac{a}{g}J_B\Delta t - \frac{\sin(\theta)}{A}Q_B\Delta t \quad (5.27)$$

The positive characteristics equation, Eq. (5.24), and the negative characteristics equation, Eq. (5.26), are a system of two equations with two unknowns. Inserting Eq. (5.24) into Eq. (5.26) and solving for H_P yields:

$$H_P = \frac{C_p + C_m}{2} \quad (5.28)$$

Q_P can then be calculated with Eq. (5.29).

$$Q_P = \frac{H_P - C_m}{B} \quad (5.29)$$

5.1.1. STEADY STATE

In the previous section it is assumed that values at point A and B are known. To satisfy this, the steady state of the system has to be determined. Assuming that the flow rate is constant throughout the pipe in steady state and by inserting the positive Δt , isolated from Eq. (5.18), simplifies Eq. (5.23) to the steady state solution for pipe flow. Note that the volumetric flow rate has been replaced by the steady state volumetric flow rate, Q_0 .

$$H_P = H_A - \frac{1}{g}J\Delta x + \frac{\sin(\theta)}{aA}Q_0\Delta x \quad (5.30)$$

5.1.2. BOUNDARY CONDITIONS

The upstream end of the pipe is modelled as a large pressure reservoir with constant pressure. The volumetric flow rate is determined with Eq. (5.26) setting $H_P = H_r$.

The downstream end of the pipe is a valve. The valve closing characteristics have a great effect on the size of the pressure peak and of the timing of the pressure peak. When the valve characteristics is unknown it can be modelled with a dimensionless closure time, τ_v , defined as in Eq. (5.31) [11].

$$\tau_v = 1 - \frac{t}{t_c}^m \quad (5.31)$$

Where t_c is the closure time and m is an adjustable constant that describes the type of closure. There are four closure types depending on the value of m , and is illustrated in Fig. (5.2).

$m = 0$ This corresponds to an instantaneous closure of the valve, which will result in the largest pressure peak.

$0 < m < 1$ Choosing m in this interval will produce a concave decrease. Values of m close to 0 will resemble the instantaneous closure and close to 1 will resemble a linear closure.

$m = 1$ This corresponds to a linear closure of the valve.

$1 < m < \infty$ Choosing m in this interval will produce a convex decrease. Again values of m close to 1 will resemble a linear closure and large values will resemble a delayed instantaneous closure.

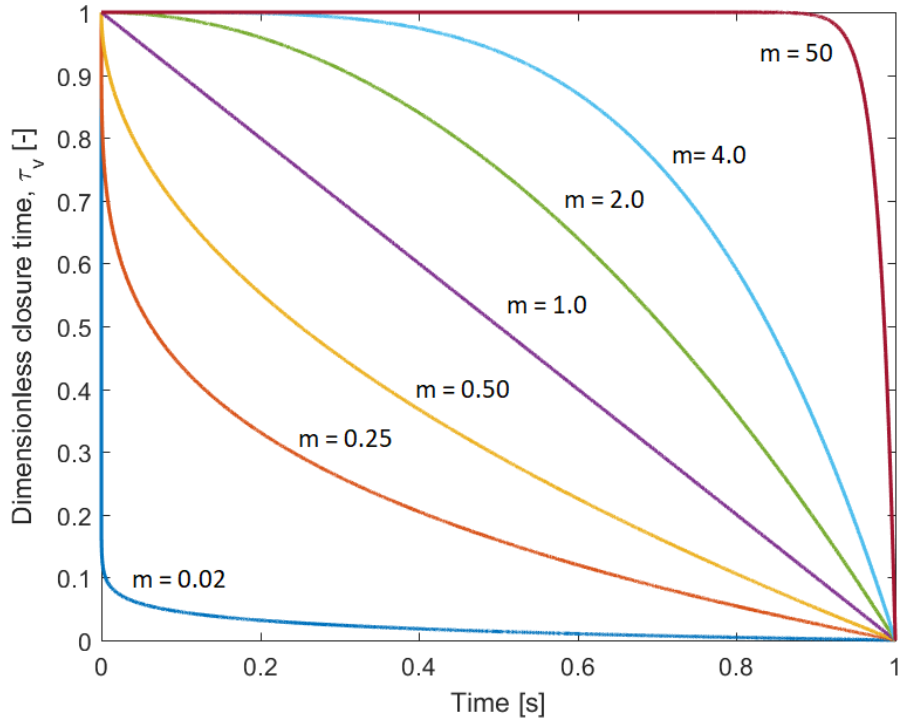


Figure 5.2: Dependency of τ_v on m .

The volumetric flow rate is calculated with Eq. (5.32) for $t < t_c$ and when $t \leq 0$ it is set to zero.

$$Q_P = -BC_v + \sqrt{(BC_v)^2 + 2C_v C_p} \quad (5.32)$$

Where C_v is defined as in Eq. (5.33).

$$C_v = \frac{(Q_0 \tau_v)^2}{2H_0} \quad (5.33)$$

5.2. GRID TYPE

In MOC there are two different grid types, assuming constant wave speed: The rectangular grid and the diamond grid. The diamond grid, see Fig. 5.3b, works by calculating the nodes where the characteristics lines meet. This can result in problems when calculation and plotting the results, because each node is only calculated for half of the time steps. This is normally solved via interpolation but this might result in interpolation errors, which is not wanted. This is not a problem for the rectangular grid (see Fig. 5.3a) because it is simply two diamond grids, making it possible to calculate every time step for the nodes. This, however, comes with its own problems, because the diamond grids are not directly connected to each other, and can therefore cause numerical oscillation with certain unsteady friction models [12]. Together with this, the rectangular grid is also more computationally heavy, because it calculates each node for every time step. The grid type used herein will be the rectangular grid type to avoid the need of interpolation.

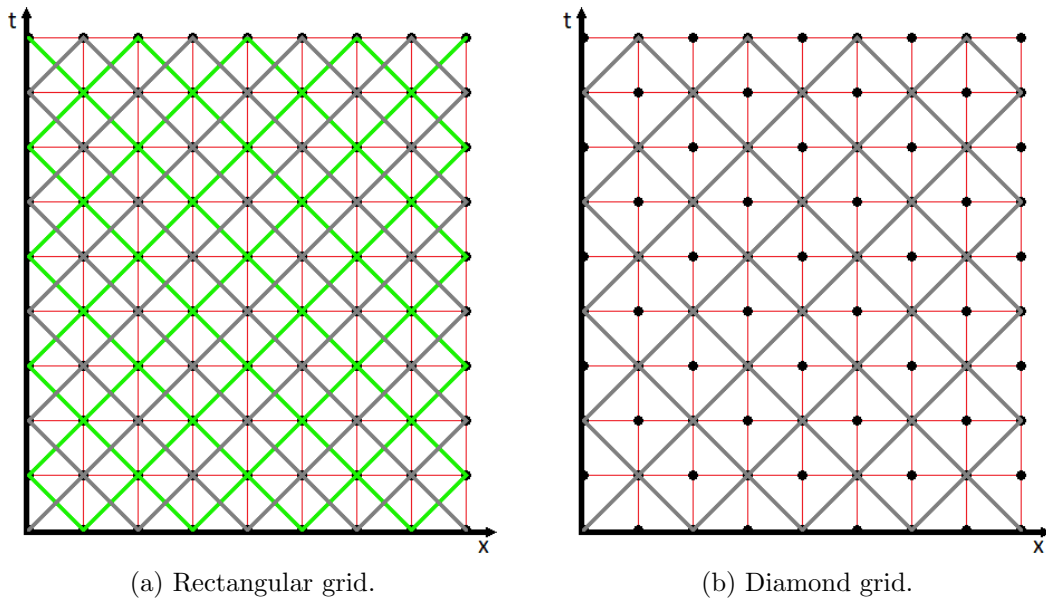


Figure 5.3: The rectangular and diamond grid.

5.3. FRICTION MODELS

The friction term, described by J as in Eq. (5.34), is the combination of a quasi-steady, J_{qs} , and an unsteady part, J_{us} . [13]

$$J = J_{qs} + J_{us} \quad (5.34)$$

Modelling only the quasi-steady friction approximates the first pressure peak well, but underestimates the friction for the rest of the transient event [1]. Therefore, the unsteady friction is crucial for the description of the entire transient event [14]. Duan et al. [15] investigated the relevance of the unsteady friction with dependence on pipe length and Reynolds number and it showed that the relevance of the unsteady friction decreased with increasing lengths and Reynolds numbers. The reason being that the unsteady friction phenomenon occurs where the fluid accelerates or decelerates which is close to the pressure wave front [16, 17]. This means that for a long pipe, the unsteady friction relevance should be less than for a short pipe, as the pressure wave front needs to propagate longer. Therefore the pressure wave front is present at a point for only a fraction of the time of the transient event. The unsteady friction is still important to model, but it is good to note that for actual pipeline systems the relevance might be smaller compared to the relatively short pipe line systems used for experiments.

The unsteady friction is primarily modelled by two different friction model types: The Convolution Based (CB) friction model and the Instantaneous Acceleration Based (IAB) friction model. The friction models investigated will be a CB friction model suggested by Vardy & Brown [18] and an IAB model suggested by Brunone et. al [17].

5.3.1. QUASI-STEADY FRICTION

The quasi-steady friction is calculated with the skin friction in Eq. (5.35).

$$J_{qs} = \frac{fQ|Q|}{2DA^2} \quad (5.35)$$

Where f is the friction factor. The friction factor calculation method is dependent on the flow regime in the pipe. For laminar flow it is calculated with Eq. (5.36) and for turbulent flow it is calculated with the Colebrook equation in Eq. (5.37)[19].

$$f = \frac{64}{Re} \quad (5.36)$$

$$\frac{1}{\sqrt{f}} = -2.0 \log \left(\frac{\epsilon/D}{3.7} + \frac{2.51}{Re\sqrt{f}} \right) \quad (5.37)$$

The quasi-steady friction is implemented such that it is updated for each time step and position according to the local flow conditions.

5.3.2. VARDY & BROWN FRICTION MODEL

The CB friction model was first developed by Zielke [16] for laminar flow and was extended to the turbulent flow regime for a smooth pipe by Vardy & Brown [18]. The CB friction model is the convolution of the history of accelerations and of a weighting function, as in Eq. (5.38).

$$J_{us} = \frac{16\mu}{\rho D^2 A} \left(\frac{\partial Q}{\partial t} * W(\tau) \right) \quad (5.38)$$

Where μ and ρ is the dynamic viscosity and density of the fluid respectively, $\frac{\partial Q}{\partial t}$ is the acceleration, $W(\tau)$ is the weighting function that is dependent the dimensionless time τ defined as in Eq. (5.39).

$$\tau = \frac{4\rho t}{\mu D^2} \quad (5.39)$$

The weighting function developed by Vardy & Brown, in Eq. (5.40), is derived assuming a bilinear eddy viscosity distribution and assuming frozen viscosity. The weighting function is valid for Reynolds numbers ranging from 2000 to 10^8 .

$$W(\tau) = \frac{A^* e^{\tau B^*}}{\sqrt{\tau}} \quad (5.40)$$

Where $A^* = \frac{1}{2\sqrt{\pi}}$, $B^* = \frac{Re^\kappa}{12.86}$, $\kappa = \log\left(\frac{15.29}{Re^{0.0567}}\right)$ and it is assumed that the eddy viscosity at the wall is equal to the laminar viscosity i.e. $\nu_w = \nu_{lam}$.

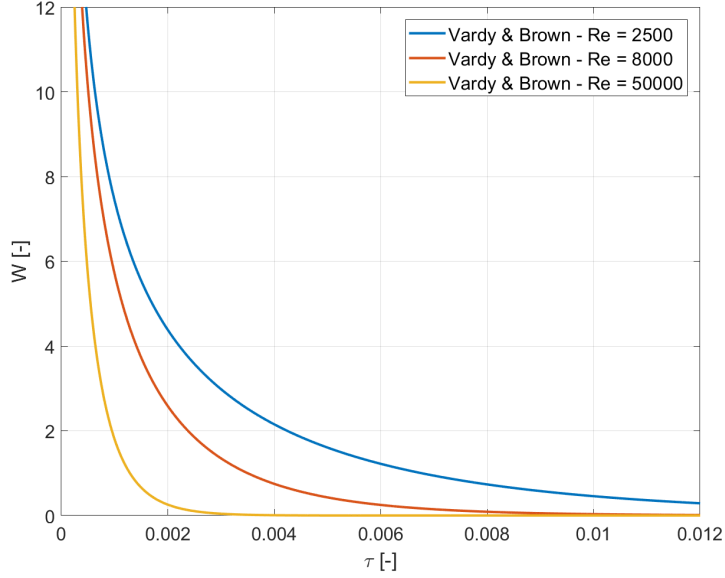


Figure 5.4: Illustration of the weighting function's, derived by Vardy & Brown, dependency on the Reynolds number.

In Fig. 5.4 it is clear that with an increase in the Reynolds number the weighting function tend to zero quicker. This results in past accelerations having a smaller effect on the friction with increasing Reynolds numbers.

The Vardy & Brown friction model is implemented in a rectangular grid via a first order finite difference approximation as in Eq. (5.41)[20].

$$J_{us} = \frac{16\rho}{\mu D^2 A} \sum_{j=2}^{n-1} \left(Q(i, n-j+1) - Q(i, n-j) \cdot W \left(j\Delta\tau - \frac{\Delta\tau}{2} \right) \right) \quad (5.41)$$

Where i is the position index, j is the time index, $n \geq 3$ and is the number of time steps from the start of the transient event and $\Delta\tau$ is the dimensionless time step and is defined as in Eq. (5.42).

$$\Delta\tau = \frac{4\rho\Delta t}{\mu D^2} \quad (5.42)$$

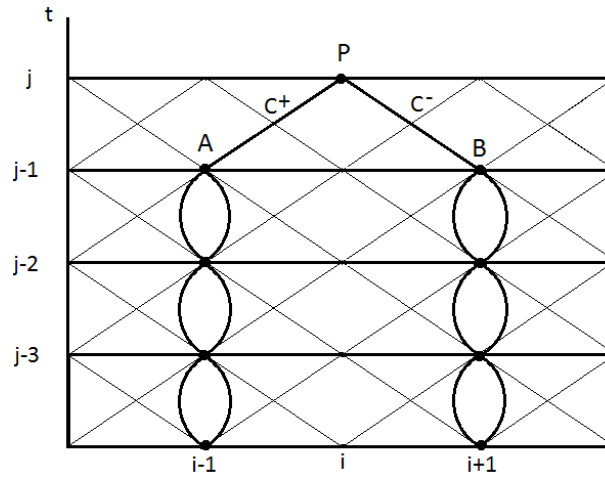


Figure 5.5: Illustration of the discretisation of Eq. (5.41).

In Fig. 5.5 a graphical representation of the discretisation is present. As in the previous chapter, the value at point P is determined by the positive and negative characteristics equations. For the positive characteristics equation values of the acceleration history at point A is used and for the negative characteristics equation values at point B . The thin lines correspond to the characteristic lines of the system. To calculate the acceleration at point A values at time $j-1$ and $j-2$ is used. These two values are not on the same characteristics grid, but on two independent diamond grids which is a consequence of the rectangular grid.

5.3.3. BRUNONE FRICTION MODEL

The IAB friction model suggested by Brunone et al. [17] is dependent on the local instantaneous acceleration and the local instantaneous convective acceleration, as in Eq.

(5.43).

$$J_{us} = \frac{k}{A} \left(\frac{\partial Q}{\partial t} - a \frac{\partial Q}{\partial x} \right) \quad (5.43)$$

Where k is Brunone's friction coefficient, $\frac{\partial Q}{\partial t}$ is the local acceleration, $\frac{\partial Q}{\partial x}$ is the local convective acceleration. Eq. (5.43) predicts the convective acceleration correctly in the case of a downstream valve, but Vítkovský showed that it failed to predict other cases such as an upstream valve which led to the corrected version in Eq. (5.44) [21].

$$J_{us} = \frac{k}{A} \left(\frac{\partial Q}{\partial t} - a \cdot \text{sign}(Q) \frac{\partial Q}{\partial x} \right) \quad (5.44)$$

Brunone's friction coefficient can be determined either empirically, as suggested by Brunone et al. [17], or by determining Vardy's shear decay coefficient, C^* , as suggested by Vardy & Brown [18] in Eq. (5.45).

$$k = \frac{\sqrt{C^*}}{2} \quad (5.45)$$

Vardy's shear decay coefficient, for smooth pipes, can be calculated for laminar flow as in Eq. (5.46) and for turbulent flow with Eq. (5.47) [21].

$$C^* = 0.000476 \quad (5.46)$$

$$C^* = \frac{7.41}{Re^{\log(14.3/Re^{0.05})}} \quad (5.47)$$

The Brunone friction coefficient dependency on the Reynolds number is illustrated in Fig. 5.6.

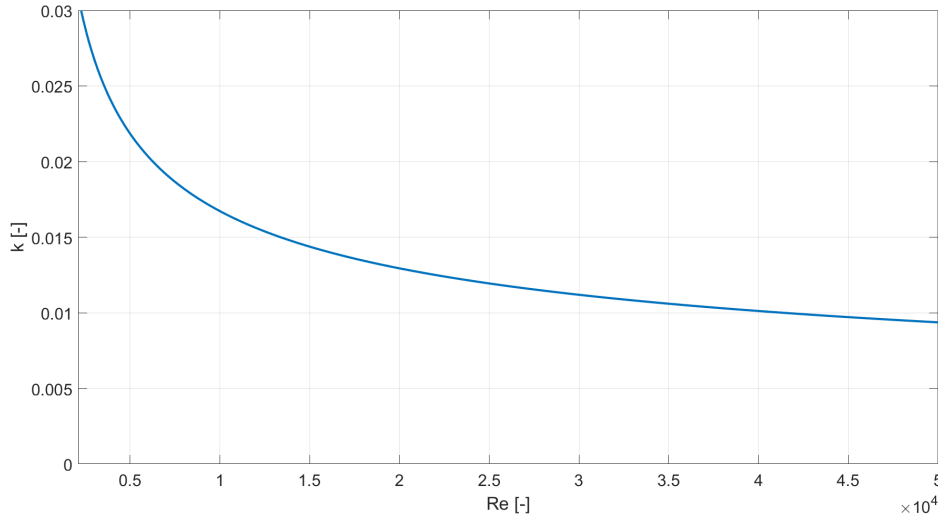


Figure 5.6: The relationship between Brunone's friction coefficient and the Reynolds number.

As with the weighting function it is clear that k decreases with an increase in Reynolds number.

The implementation of the Brunone friction model with both explicit and implicit implementation was investigated by Vítkovský et al. [22] and it showed that there was no significant difference between them. Therefore the instantaneous acceleration and instantaneous convective acceleration are implemented explicitly as in Eq. (5.48) and Eq. (5.49) and are illustrated in Fig. 5.7.

$$C^+ : \begin{cases} \frac{\partial Q}{\partial t} \approx \frac{Q(i-1,j-1) - Q(i-1,j-2)}{\Delta t} \\ \frac{\partial Q}{\partial x} \approx \frac{Q(i,j-1) - Q(i-1,j-1)}{\Delta x} \end{cases} \quad (5.48)$$

$$C^- : \begin{cases} \frac{\partial Q}{\partial t} \approx \frac{Q(i+1,j-1) - Q(i+1,j-2)}{\Delta t} \\ \frac{\partial Q}{\partial x} \approx \frac{Q(i+1,j-1) - Q(i,j-1)}{\Delta x} \end{cases} \quad (5.49)$$

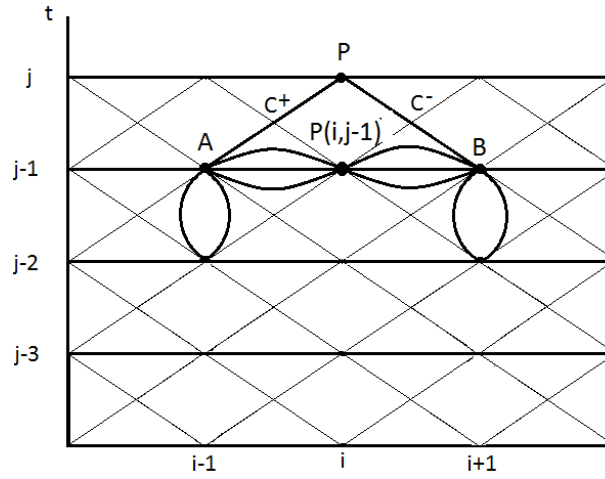


Figure 5.7: Illustration of the discretisation of Eq. (5.48) and (5.49).

6. CFD MODELLING OF SINGLE PHASE FLOW

The conservation equations: Continuity and momentum, is solved for all flows in ANSYS Fluent.

6.1. CONTINUITY EQUATION

For the conservation of mass the equation can be written as in Eq. (6.1).

$$\underbrace{\frac{\partial \rho}{\partial t}}_{\text{accumulation}} + \underbrace{\frac{\partial}{\partial x_j}(\rho u_j)}_{\text{convection}} = 0 \quad (6.1)$$

The equation is valid for both incompressible and compressible flows.

6.2. MOMENTUM EQUATION

The compressible Navier-Stokes momentum equation is written as in Eq. (6.2). It is assumed that there is no body force, gravity and slip velocity.

$$\underbrace{\frac{\partial}{\partial t}(\rho u_i)}_{\text{accumulation}} + \underbrace{\frac{\partial}{\partial x_j}(\rho u_i u_j)}_{\text{convection}} = - \underbrace{\frac{\partial P}{\partial x_i}}_{\text{pressure gradient}} + \underbrace{\frac{\partial}{\partial x_j} \left(\mu \left(\frac{\partial u_i}{\partial x_j} + \frac{\partial u_j}{\partial x_i} \right) \right)}_{\text{viscous stresses}} \quad (6.2)$$

6.3. TURBULENCE MODELS

To analyze if the choice of turbulence model has an effect on the simulation results, three different RANS turbulence models will be tested: Realizable $k - \epsilon$, Standard $k - \omega$, and Shear-Stress Transport (SST) $k - \omega$ model. All of the equations are written for a single phase flow.

6.3.1. REALIZABLE $k - \epsilon$ MODEL

The effects of convection, diffusion, production, and destruction of turbulence are described by the Realizable $k - \epsilon$ model. The model consists of two partial differential transport equations: The turbulent kinetic energy, k , and the rate of dissipation of turbulent energy ϵ . The equation for the turbulent kinetic energy is seen in Eq. (6.3).

$$\underbrace{\frac{\partial}{\partial t}(\rho k)}_{\text{accumulation}} + \underbrace{\frac{\partial}{\partial x_i}(\rho k \bar{u}_i)}_{\text{convection}} = \underbrace{\frac{\partial}{\partial x_j} \left(\left(\mu + \frac{\mu_t}{\sigma_k} \right) \frac{\partial k}{\partial x_j} \right)}_{\text{viscous + turbulent diffusion}} + \underbrace{G_k - \rho \epsilon - Y_M}_{\text{other terms}} \quad (6.3)$$

Where μ_t is the turbulent viscosity, σ_k is the turbulent Prandtl numbers for k , G_k is the effect of the mean velocity gradient, and Y_M is the fluctuating dilatation of the overall

dissipation rate in the compressible turbulence.

The rate of dissipation of turbulent energy are expressed as in Eq. (6.4).

$$\underbrace{\frac{\partial}{\partial t}(\rho\epsilon)}_{\text{accumulation}} + \underbrace{\frac{\partial}{\partial x_i}(\rho\epsilon\bar{u}_i)}_{\text{convection}} = \underbrace{\frac{\partial}{\partial x_j} \left(\left(\mu + \frac{\mu_t}{\sigma_\epsilon} \right) \frac{\partial \epsilon}{\partial x_j} \right)}_{\text{viscous + turbulent diffusion}} + \underbrace{\rho C_1 S \epsilon}_{\text{production of } \epsilon} - \underbrace{\rho C_2 \frac{\epsilon^2}{k + \sqrt{\nu \epsilon}}}_{\text{disintegrating term}} \quad (6.4)$$

Where S is the modulus of the mean rate of the strain tensor, C_1 and C_2 are constants and ν is the kinematic viscosity. The Realizable model deviates from the Standard $k - \epsilon$ model by proposing a new production and disintegration term in the dissipation equation as this equation is a weakness of the Standard model. The model is realizable because the turbulent normal stresses is non-negative [23]. The Standard and RNG $k - \epsilon$ models use a constant, C_μ , for the eddy viscosity where the Realizable model uses a function describing the effect of the mean rotation on the Reynolds stresses.

For the closure of the $k - \epsilon$ model the eddy viscosity is calculated as in Eq. (6.5).

$$\mu_t = C_\mu \rho \frac{k^2}{\epsilon} \quad (6.5)$$

The default model constants of the Realizable model from Fluent User Guide are used [23].

Nikpour et al. [24] has analysed the Standard, Realizable and RNG $k - \epsilon$ model and the Reynolds Stress Model for a water hammer simulation. It was concluded that the Realizable model was the best turbulence model for the case based on simulation accuracy and computational time.

6.3.2. STANDARD $k - \omega$

The Standard $k - \omega$ model has a robust and accurate formulation in the near-wall region, but is strongly sensitive for freestream flow (outside the shear layer). As the Realizable $k - \epsilon$ model, the $k - \omega$ models consist of two transport PDE's: The turbulent kinetic energy, k , and the specific rate of dissipation of turbulent energy, ω , which is a ratio of ϵ to k . The equation for the turbulent kinetic energy is seen in Eq. (6.6).

$$\frac{\partial}{\partial t}(\rho k) + \frac{\partial}{\partial x_i}(\rho k \bar{u}_i) = \frac{\partial}{\partial x_j} \left(\left(\mu + \frac{\mu_t}{\sigma_k} \right) \frac{\partial k}{\partial x_j} \right) + G_k - Y_k \quad (6.6)$$

Where Y_k is the dissipation of k due to turbulence. The equation for the specific rate of dissipation of turbulent energy, is as seen in Eq. (6.7).

$$\frac{\partial}{\partial t}(\rho \omega) + \frac{\partial}{\partial x_i}(\rho \omega \bar{u}_i) = \frac{\partial}{\partial x_j} \left(\left(\mu + \frac{\mu_t}{\sigma_\omega} \right) \frac{\partial \omega}{\partial x_j} \right) + G_\omega - Y_\omega \quad (6.7)$$

Where G_ω is the production of ω .

The closure for the $k - \omega$ model, the turbulent viscosity, is calculated with Eq. (6.8).

$$\mu_t = \frac{\rho k}{\omega} \quad (6.8)$$

The default model constants of the $k - \omega$ model from Fluent User Guide are used [23].

6.3.3. SST $k - \omega$

Menter (1992) proposed a hybrid model combining the Standard $k - \omega$ model's behaviour at the near-wall region with the Standards $k - \epsilon$ model's at the free stream flow region. The turbulent kinetic energy is calculated as in Eq. (6.6) and the specific rate of dissipation of turbulent energy as in Eq. (6.9).

$$\frac{\partial}{\partial t}(\rho\omega) + \frac{\partial}{\partial x_i}(\rho\omega\bar{u}_i) = \frac{\partial}{\partial x_j} \left(\left(\mu + \frac{\mu_t}{\sigma_\omega} \right) \frac{\partial\omega}{\partial x_j} \right) + G_\omega - Y_\omega + D_\omega \quad (6.9)$$

Where D_ω is the cross-diffusion, used to blend the Standard $k - \omega$ and Standard $k - \epsilon$ model.

The turbulent viscosity has been corrected for the SST model compared to the Standard $k - \omega$ model as it fails to properly predict the amount of flow separation from smooth surfaces. To obtain the proper behaviour, Eq. (6.8) has been corrected with a limiter such that the eddy viscosity will not be over-predicted.

For the SST model, the σ_k and σ_ω are dependent on the blending function, F_1 , and the constants $\sigma_{k,1}$, $\sigma_{k,2}$, $\sigma_{\omega,1}$ and $\sigma_{\omega,2}$.

The default constants of the SST $k - \omega$ model from the Fluent User Guide are used [23].

6.4. CFD SIMULATION OF SINGLE PHASE WATER HAMMER

A 1D single phase water hammer experiment is compared with a CFD simulation to prove that the CFD method is a reliable method for water hammer simulation and to test different boundary conditions for later two phase simulations. A grid independency analysis and turbulence test are not performed because it is not found essential for the purpose of the single phase CFD simulation. The CFD simulation is performed using ANSYS Fluent 19.0.

The single phase experiment chosen is Case 1 from Soares et al. described in Sec. 4.1. The CFD simulation will be compared to MOC simulations using different unsteady friction models performed on the 9th semester [1].

6.4.1. GEOMETRY AND MESH

The geometry is constructed as 2D axisymmetric to simulate the effects in a 15.22m straight pipe. The cell shape for the mesh is chosen as quadrilateral with 16500 cells (15 · 1100cells) as seen on Fig. 6.1.

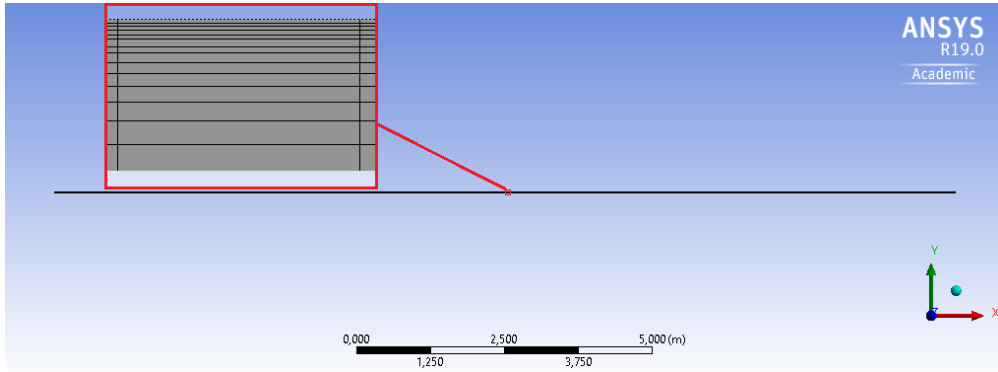


Figure 6.1: Quadrilateral mesh.

An inflation is used for better refinement at the wall and thereby obtaining a lower y^+ value. The y^+ value is below 5, which is in the viscous sublayer. The aspect ratio has a maximum of 99.67.

6.4.2. SETUP

The coupled pressure based solver is used with the SST $k-\omega$ turbulence model. The SST model is chosen as it combines the advantages of the $k-\epsilon$ and the $k-\omega$ model and accounts for the transport of turbulent shear stress when defining the turbulent viscosity. The time step size is chosen as 10^{-5} to account for the speed of sound through each cell.

6.4.3. BOUNDARY CONDITIONS

The boundary conditions chosen for the simulation is a "pressure-inlet" to describe the pressure at the upstream reservoir, which is assumed constant, and a "mass flow-outlet" to describe the mass flow through the pipe. For the two phase simulation the "mass flow-outlet" and the "velocity-outlet" are not possible. Therefore a simulation using a "reverse" velocity with a "velocity-inlet" and a "pressure-outlet" boundary condition has also been tested. For this the inlet boundary condition is a Dirichlet (constant velocity over the boundary) and the outlet a Neumann (pressure based). The purpose of this simulation is to analyze if the different boundary conditions have an effect on the pressure wave at the valve.

The velocity profile at the valve with the "mass flow-outlet" and the negative velocity "velocity-inlet" are illustrated in Fig. 6.2. With the "velocity-inlet" boundary, the flow has a fixed velocity over the entire boundary whereas the "mass flow-outlet" velocity profile has been developing through the pipe as seen in Fig. 6.2. The "mass flow-outlet" reaches a higher velocity at the pipe core as it has obtained a developed velocity profile.

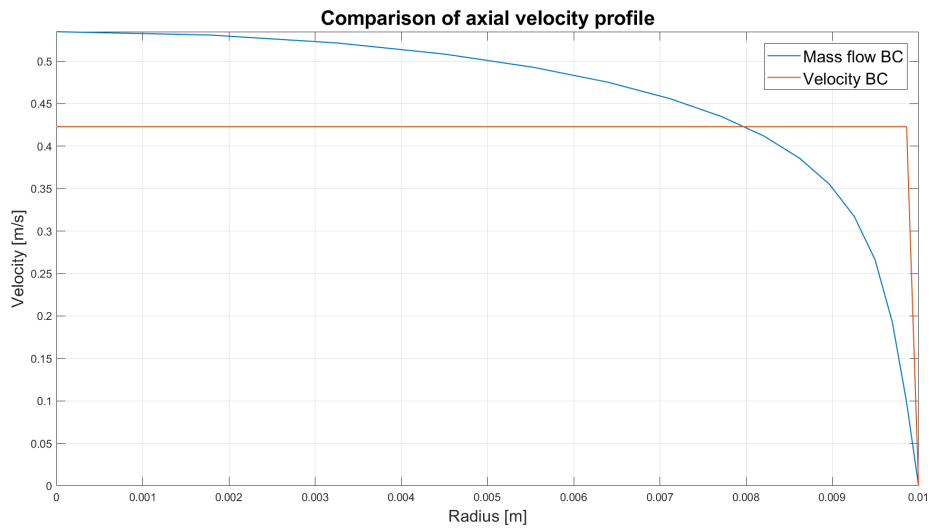


Figure 6.2: Velocity profile comparison.

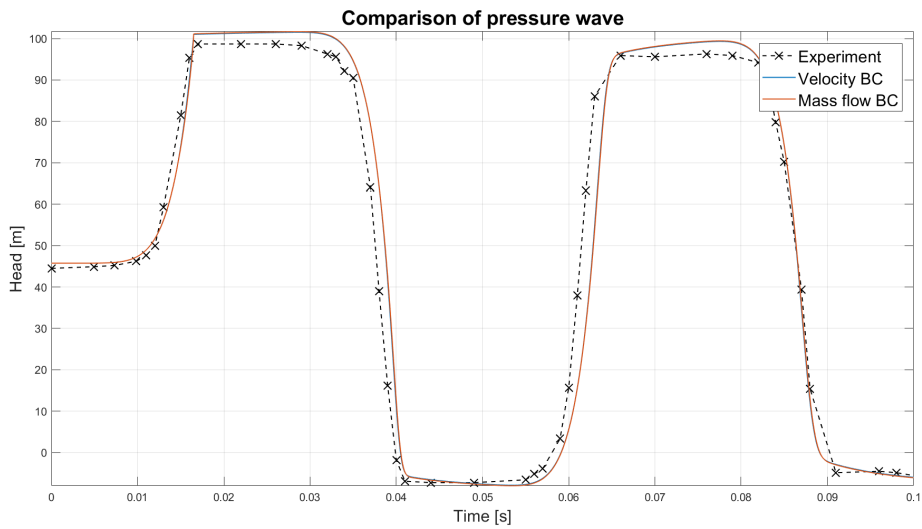


Figure 6.3: Pressure wave comparison.

As the pressure is close to uniform at the boundary, the pressure is taken as an average of the 15 nodes for the pressure wave. The pressure wave with the two boundary conditions are compared in Fig. 6.3. It can be seen, the pressure wave is almost identical with the two different boundary condition setups. The velocity profile did not have a significant

effect on the pressure wave and the "velocity-inlet" will be used for the two phase simulations.

6.4.4. VALVE CLOSURE

As the flow behaviour through the valve is not of interest, the valve closure is described by a user defined function (UDF) at the mass-flow outlet boundary. The UDF controls the outlet mass flow by the closure function τ_v described in Eq. (5.31).

6.4.5. BULK MODULUS

The pipe walls are not modelled in the simulation as fluid structure interaction is not used. Therefore, the bulk modulus has been modified to take into account the elasticity effect on the fluid from the pipe. The speed of sound can be calculated with Eq. (6.10), which assumes no effect from the pipe, and with Eq. (6.11), which accounts for the pipe.

$$a = \sqrt{\frac{K}{\rho}} \quad (6.10)$$

$$a = \sqrt{\frac{K/\rho}{1 + ((K/E)(D/e))c_1}} \quad (6.11)$$

Eq. (6.10) and Eq. (6.11) is set equal to each other as it is assumed that the speed of sound is constant. The bulk modulus, in Eq. (6.10), now noted as K' , is then isolated and an equation of a modified bulk modulus is obtained in Eq. (6.12).

$$K' = \frac{K}{1 + \frac{KD}{eE}} \quad (6.12)$$

If the pipe elasticity effects is not included, the wave speed would be too high, which would be unrealistic.

This modified bulk modulus is specified in Ansys Fluent when the density of water is set to compressible.

6.4.6. RESULTS

The CFD results are compared with the results obtained by MOC with the quasi-steady, Brunone and Vardy & Brown friction models which can be seen in Fig. 6.4. It can be seen that both unsteady friction models and the CFD model overestimate the pressure of the first peak and that the quasi-steady friction model give the best result. On the second peak both the CFD model and all the MOC models agree closely on the pressure. It can also be seen that the behaviour of the CFD model and friction model suggested by Vardy & Brown is very similar and that the quasi-steady friction model and the friction model suggested by Brunone have similar behaviour with the Brunone friction model giving a broader peak. From the following peaks it is clear that the Brunone gives the

best results followed by the CFD, Vardy & Brown, and the quasi-steady friction model in that order. From the comparison of the CFD simulation with the experimental results, it can be concluded that CFD model is valid for water hammer modelling.

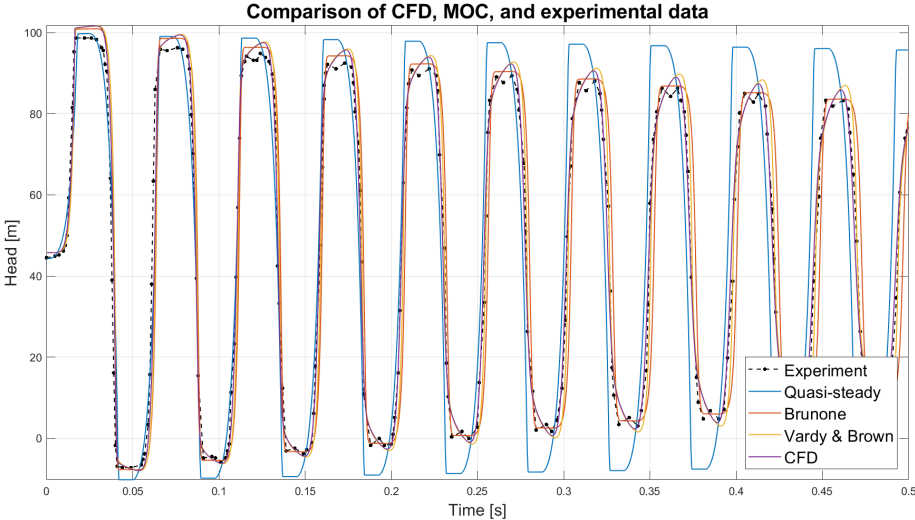


Figure 6.4: Soares single phase comparison.

7. MODELLING OF A TWO PHASE FLOW USING THE METHOD OF CHARACTERISTICS

The following sections will cover the modelling of the two phase water hammer that occurs when the pressure is decreased to the vapour pressure. In Sec. 3 the nature of cavitation is briefly described as well as the effects these have on the water hammer event. From this it is clear that there are primarily two things that will have to be modelled: The formation and collapse of vapour bubbles/cavities and the effect these have on the wave speed. For a two phase water hammer the wave speed can be calculated by Eq. (7.1) [3].

$$a' = \sqrt{\frac{\frac{K_m}{\rho_m}}{1 + \left(\frac{K_m D}{Ee}\right) c_1}} \quad (7.1)$$

Where ρ_m is the mixture density. The mixture density is calculated with Eq. (7.2), where it is assumed that the void fraction, α , is low, and therefore $\rho_m \approx \rho_l$.

$$\rho_m = \alpha \rho_g + (1 - \alpha) \rho_l \approx \rho_l \quad (7.2)$$

The bulk modulus of the mixture, K_m , can be described with Eq. (7.3).

$$K_m = \frac{K_l}{1 + \alpha \left(\frac{K_l}{P_g} - 1\right)} \quad (7.3)$$

Where K_l is the bulk modulus of the liquid phase and P_g is the absolute partial pressure of the gas phase, which can be described with Eq. (7.4). [3]

$$P_g = \rho_l g (H - z - H_v) \quad (7.4)$$

Where H_v is the gauge saturation/vapour pressure. It is assumed that P_g is equal to the bulk modulus of the gas phase for isothermal conditions.

Eq. (7.3) can be simplified to Eq. (7.5) by recognising that $K_l/p_g \gg 1$.

$$K_m = \frac{K_l}{1 + \alpha \frac{K_l}{p_g}} \quad (7.5)$$

Inserting Eq. (7.2) and (7.5) into Eq. (7.1), and rearranging, the expression for a' in Eq. (7.6) is obtained.

$$a' = \sqrt{\frac{\frac{K_l}{\rho_l}}{\left(1 + \alpha \frac{K_l}{p_g}\right) + \left(\frac{K_l D}{Ee}\right) c_1}} \quad (7.6)$$

It is possible to simplify Eq. (7.6) to Eq. (7.7).

$$a' = \frac{a}{\sqrt{1 + \frac{\alpha \frac{K_l}{p_g}}{1 + \left(\frac{K_l D}{Ee}\right) c_1}}} \quad (7.7)$$

Where a is the wave speed in a single phase system, described with Eq. (2.1). A problem with a' is the fact that it is pressure dependent, and therefore will change size during the simulation. This will be a problem when setting up the one-dimensional equations for the MOC, because the size of the reaches and of the time step will change over time. In Fig. 7.1, an example of how the grid can change is shown, where the red lines represent the grid with a' , while the places where the grey lines intersect represent the grid with a .

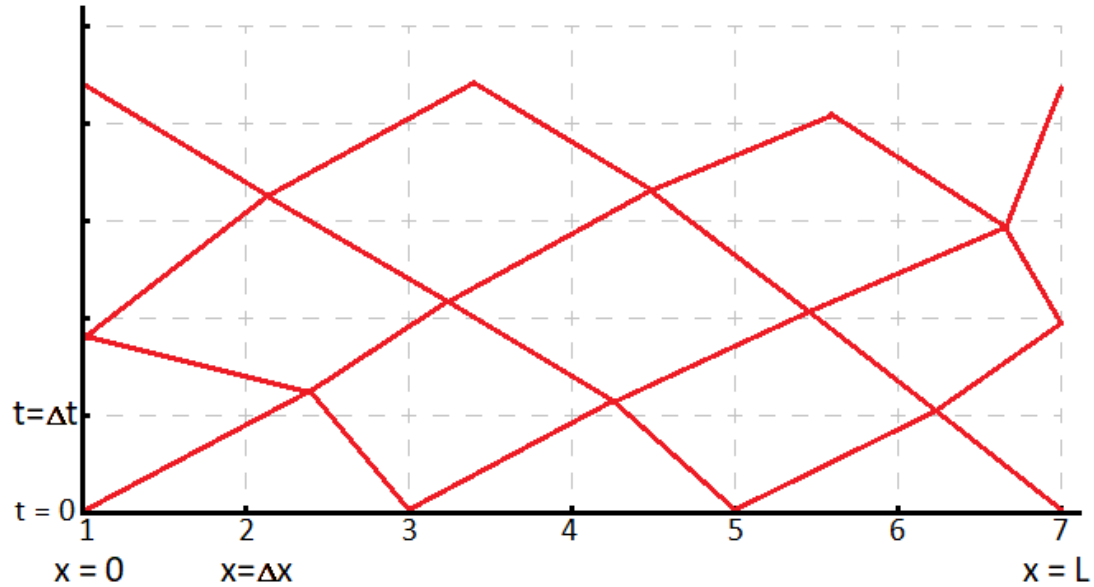


Figure 7.1: Effect of relating the wave speed to the absolute partial pressure of the gas, i.e. having a varying wave speed.

In extreme cases, the nodes can shift outside of the ends of the pipe, which is not physically possible, and nodes would have to be removed during the calculation. A way to solve this problem would be to interpolate the results either at every time step or periodically (e.g. at every fifth time step). This will move the nodes back to predetermined positions and should remove the possibility of nodes moving away from the setup. However, doing this will introduce interpolation error, which is not of interest.

Another way to solve the problems with the moving grid would be to assume that the wave speed is not affected by the amount of free gas present. It is assumed that all the free gas, in a reach, forms a single pocket of gas at the node and therefore the wave speed between each node is constant at the speed for a single phase system. This assumption forms the basis for two commonly used two phase MOC methods, known as the Discrete Vapour Cavity Model (DVCM), which will be explained in Sec. 7.1, and the Discrete Gas Cavity Model (DGCM), which will be explained in Sec. 7.2. DVCM and DGCM models the size of the gas pocket, V_g (V_{cav} for DVCM), via Eq. (7.8). [3]

$$\frac{dV_g}{dt} = Q_{out} - Q_{in} \quad (7.8)$$

of increased attenuation. Therefore, it is best to use a ψ with a value close to 0.5, where the amount of numerical oscillation is minimal. [3]

7.1. DISCRETE VAPOUR CAVITY MODEL

DVCM assumes that there is no vapour in steady state and when the pressure is above vaporization pressure. Because of this assumption, DVCM is calculated as a single phase system when the pressure is above vaporization, with V_{cav} set to zero and $Q_{u,P} = Q_P$. When the calculated pressure becomes lower than or equal to the vaporization pressure, the node of interest is converted into a pressure boundary, where the pressure is set as in Eq. (7.11). [3]

$$H_P = z_P + H_v \quad (7.11)$$

When the node is treated as a pressure boundary, it is assumed that the difference between the flow rates $Q_{u,P}$ and Q_P is turned into vapour and stored in the node. The vapour cavity size is calculated with Eq. (7.9), where $V_{g,P}$ and $V_{g,P0}$ are replaced with $V_{cav,P}$ and $V_{cav,P0}$ respectively.

A flow chart for the calculation of an interior node is shown in Fig. 7.3, where the block with $V_{cav}(i, j - 1) > 0$ investigates whether there is a vapour cavity present in the previous time step. If there is a vapour cavity at the previous time step, it is assumed that the node is still a pressure boundary. After calculating H_P , $Q_{u,P}$, Q_P , and $V_{cav,P}$, it is checked whether the vapour cavity has condensed or if it is still there. If the vapour cavity has condensed, the node should be calculated as a single phase node, with $V_{cav} = 0$.

DVCM is the simplest of the two phase MOC models shown, and, as will be seen later, it can reproduce some of the flow scenarios to a certain degree [3]. However, it will also be seen that DVCM have its limitations for large flow rates, where it is not possible to simulate flow scenarios due to relatively large vapour cavities being created. It is recommended to keep the void fraction in every reach below 10% [25].

7.1.1. DVCM STEADY STATE

DVCM uses the same method for calculating the steady state conditions as the single phase method, shown in Sec. 5.1.1. It is assumed that the steady state conditions do not allow the formation of vapour cavities, and therefore V_{cav} is set to zero.

7.1.2. DVCM BOUNDARIES

For the upstream boundary, DVCM uses the same description for the reservoir as in the single phase method, shown in Sec. 5.1.2. It is assumed that the pressure at the reservoir is always above the vaporization pressure, and therefore no vapour cavities can be created, $V_{cav} = 0$.

For the downstream boundary, the same method for the valve closure is used to calculate the outlet flow rate, Q_P , as in Sec. 5.1.2. The head is calculated in almost the

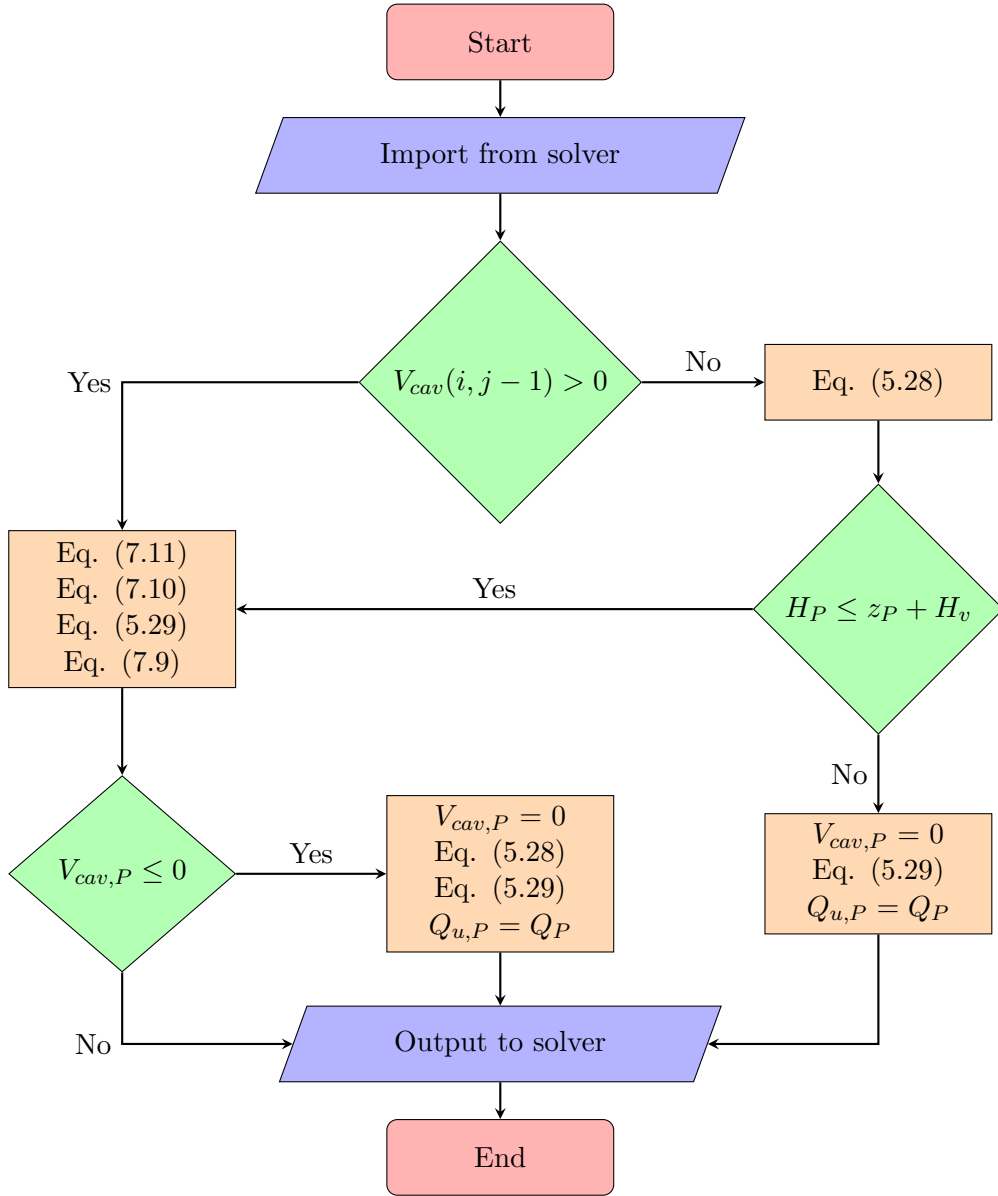


Figure 7.3: DVCN flow chart.

same way as in the flowchart in Fig. 7.3. Eq. (5.28) is replaced with $Q_{u,P} = Q_P$ and Eq. (7.12), while Eq. (5.29) is replaced with Eq. (5.32).

$$H_P = C_p - BQ_{u,P} \quad (7.12)$$

7.2. DISCRETE GAS CAVITY MODEL

DGCM assumes there is always a small amount of free gas present in the system. Because there is always a small amount of free gas present in the system, it is not possible to do as in DVCM, where the head is calculated as single phase when $H_P > z_P + H_v$ and treated as a pressure boundary when it is not. A new expression for the head has to be set up, which takes the effect of the gas cavity into account. This can be done with the use of Eq. (7.9), where $Q_{u,P}$ is described with Eq. (7.10), and Q_P with Eq. (5.29). Now, the only remaining parameter, which is not described, is $V_{g,P}$. An expression for $V_{g,P}$ can be set up with the ideal gas law and the assumption that the mass of free gas, M_g , is constant, shown in Eq. (7.13). [3]

$$M_g R_g T = P_g \alpha V = P_{g,0} \alpha_0 V \quad (7.13)$$

Where R_g is the gas constant, T is the temperature, P_g is the absolute partial pressure of the free gas, and $P_{g,0}$ is the absolute partial pressure for the initial void fraction α_0 (i.e. at steady state). $V_{g,P} = \alpha V$ is isolated from Eq. (7.13), and the result can be seen, in a simplified form, in Eq. (7.14), where P_g is described with Eq. (7.4). [3]

$$V_{g,P} = \frac{C_3}{H_P - z_P - H_v} \quad (7.14)$$

$$C_3 = \frac{P_{g,0} \alpha_0 V}{\rho_l g} \quad (7.15)$$

Combining Eq. (7.9), (7.10), (5.29), and (7.14) gives the expression in Eq. (7.16), which can be rearranged into Eq. (7.17).

$$\begin{aligned} \frac{C_3}{H_P - z_P - H_v} = V_{g,P0} \\ + 2\Delta t \left[\psi \left(\frac{H_P - C_m}{B} - \frac{C_p - H_P}{B} \right) + (1 - \psi) (Q_{P0} - Q_{u,P0}) \right] \end{aligned} \quad (7.16)$$

$$0 = (H_P - z_P - H_v)^2 + 2B_1 (H_P - z_P - H_v) - C_4 \quad (7.17)$$

Where B_2 , C_4 , B_v , and B_1 are defined as in Eq. (7.18).

$$\begin{aligned} B_2 &= \frac{0.5}{2} \\ C_4 &= \frac{B_2 B C_3}{\psi \Delta t} \\ B_v &= \frac{V_{g,P0} + (1 - \psi) (Q_{P0} - Q_{u,P0})}{\psi} \\ B_1 &= -B_2 (C_p + C_m) + B_2 B B_v + \frac{z_P + H_v}{2} \end{aligned} \quad (7.18)$$

Eq. (7.17) is treated, and solved, as a quadratic equation, shown in Eq. (7.19).

$$0 = x^2 + 2B_1x - C_4 \quad (7.19)$$

Where $x = H_P - z_P - H_{vap}$. The result can be seen in Eq. (7.20), where it can be seen that there are five expressions instead of the expected two. This is because the first two expressions can yield inaccurate results in extreme conditions of high pressure and very low volumes of free gas, or at very low pressure and high volumes of free gas, where $|B_B| = |C_4/B_1^2| \ll 1$. A way around this is to linearise the expressions, which gives the third and fourth expressions. The fifth expression is for when $B_1 = 0$.

$$H_P = \begin{cases} -B_1 (1 + \sqrt{1 + B_B}) + z_P + H_v & \text{if } B_1 < 0 \text{ and } B_B > 0.001 \\ -B_1 (1 - \sqrt{1 + B_B}) + z_P + H_v & \text{if } B_1 > 0 \text{ and } B_B > 0.001 \\ -2B_1 - \frac{C_4}{2B_1} + z_P + H_v & \text{if } B_1 < 0 \text{ and } B_B < 0.001 \\ \frac{C_4}{2B_1} + z_P + H_v & \text{if } B_1 > 0 \text{ and } B_B < 0.001 \\ \sqrt{C_4} + z_P + H_v & \text{otherwise} \end{cases} \quad (7.20)$$

With the expression for the head, the flow rates, and the gas cavity size are calculated with Eq. (7.10), (5.29), and (7.9) respectively.

7.2.1. DGCM STEADY STATE

DGCM calculates the steady state conditions in almost the same way as in the single phase method, shown in Sec. 5.1.1. The only difference is the addition of the calculation for the volume of gas. This is done with Eq. (7.14), which can be simplified to Eq. (7.21) upon insertion of C_3 , with $P_{g,0} = \rho_l g (H_P - z_P - H_v)$.

$$V_g = \alpha_0 V \quad (7.21)$$

7.2.2. DGCM BOUNDARIES

For the upstream boundary, the same addition as to the steady state calculations, is added to the single phase reservoir method, meaning the volume of gas is calculated with Eq. (7.14), while the rest is calculated as in Sec. 5.1.2.

For the downstream boundary, the same method for the valve closure is used to calculate the outlet flow rate, Q_P , as in Sec. 5.1.2. The head is described in a similar fashion as is Sec. 7.2, however, now Q_P is known and therefore, Eq. (5.29) is not inserted into Eq. (7.9). This gives the expression in Eq. (7.22), which can be rearranged into Eq. (7.23)

$$\frac{C_3}{H_P - z_P - H_v} = V_{g,P0} + 2\Delta t \left[\psi \left(Q_P - \frac{C_p - H_P}{B} \right) + (1 - \psi) (Q_{P0} - Q_{u,P0}) \right] \quad (7.22)$$

$$0 = (H_P - z_P - H_v)^2 + 2B_1 (H_P - z_P - H_v) - C_4 \quad (7.23)$$

Where B_2 , C_4 , B_v , and B_1 are defined as in Eq. (7.24).

$$\begin{aligned}
 B_2 &= \frac{1}{2} \\
 C_4 &= \frac{B_2 B C_3}{\psi \Delta t} \\
 B_v &= \frac{\frac{V_{g,P0}}{2\Delta t} + (1 - \psi)(Q_{P0} - Q_{u,P0})}{\psi} \\
 B_1 &= -B_2(C_p - BQ_P) + B_2 B B_v + \frac{z_P + H_v}{2}
 \end{aligned} \tag{7.24}$$

Since Eq. (7.23) has the same form as Eq. (7.17), the head at the valve can be described with Eq. (7.20), remembering to use the expressions from Eq. (7.24) instead of Eq. (7.18).

The flow rates and gas cavity size are calculated with Eq. (7.10), (5.32), and (7.9) respectively.

7.3. MOC SETTINGS - TWO PHASE SOARES

In order to set up MOC for case 2, the valve closure coefficient, m , the weighting factor, ψ , and the number of reaches, n , have to be chosen.

m was chosen as 5, while ψ and the number of reaches is determined via a grid independency analysis where it was chosen to investigate grids with 6, 12, 24, 48, 96, and 192 reaches. If a full analysis were to be conducted, a total of 108 different simulations would have to be conducted (6 different grids X 3 different friction models X 3 different weighting factor values (0.55, 0.75 and 0.95) X 2 different two phase models). It was chosen to reduce the number of simulations and use the following approach:

1. Find the appropriate weighting factor, ψ , for the analysis using a frequently used grid size of 24 reaches [14, 12].
2. Conduct a grid independency analysis for each friction model for both DVCM and DGCM with the chosen ψ .
3. Compare and choose the best friction model for DVCM and DGCM separately.

After this there will be a setup for DVCM and for DGCM, which will be compared with the CFD simulations in Sec. 10.1. The reason for conducting a grid independency analysis for each friction model is because it was seen that it was not the same mesh which was ideal for all friction models.

The ψ values used for the grid independency analysis can be seen in Table 7.1, where it can be seen that for DVCM, all the friction models use the same values. For DGCM however, it can be seen that the quasi-steady friction model required a higher ψ value compared to Brunone and Vardy & Brown, which is due to numerical oscillation. Fig. 7.4 show how much numerical oscillation was produced during the simulation with quasi-steady friction, while Fig. 7.5 show how much was seen for Brunone. For quasi-steady, it can be seen that there is still some numerical oscillation with $\psi = 0.75$, and notably more than with $\psi = 0.95$, however, since it was recommended to choose a value close to $\psi = 0.5$, it was chosen to use $\psi = 0.75$ because the numerical oscillation was of relatively small magnitude.

Table 7.1: ψ chosen for the grid independency analysis.

Friction models	DVCM	DGCM
Quasi-steady	0.55	0.75
Brunone	0.55	0.55
Vardy & Brown	0.55	0.55

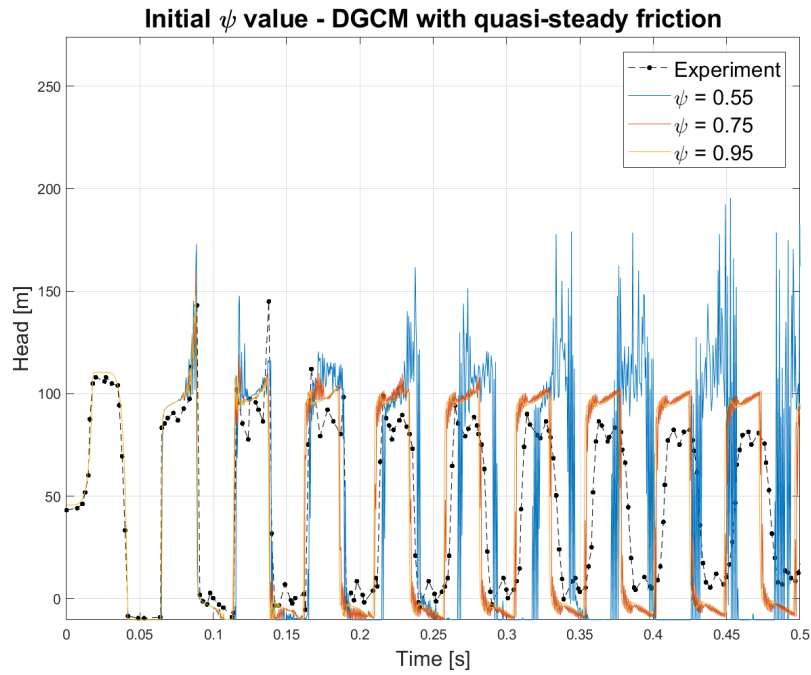


Figure 7.4: Comparison of different ψ values for DGCM with quasi-steady friction.

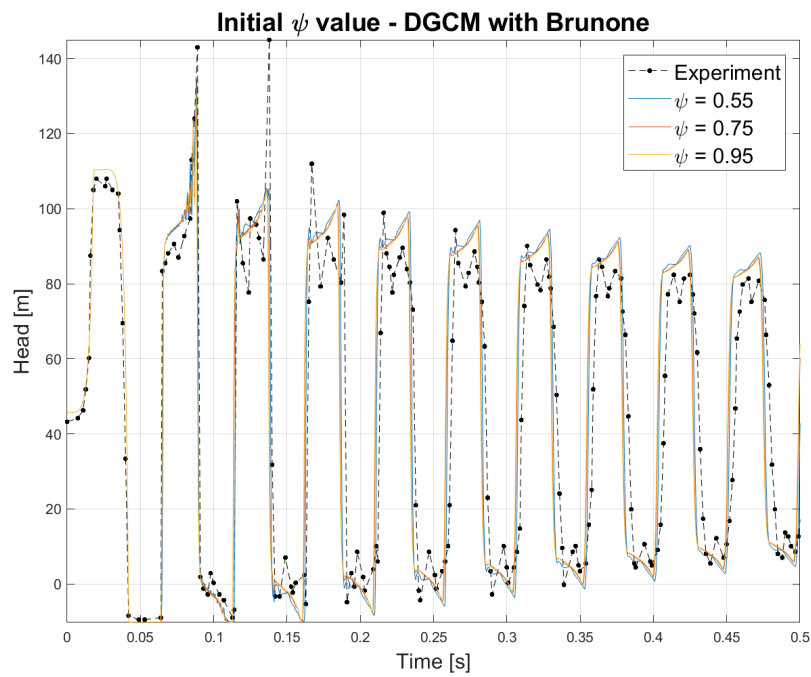


Figure 7.5: Comparison of different ψ values for DGCM with Brunone unsteady friction.

7.3.1. GRID INDEPENDENCY ANALYSIS

The grid independency analysis was, as mentioned, performed on six different meshes with 6, 12, 24, 48, 96, and 192 reaches respectively for each friction model for each two phase method. In the comparison, the following three parameters were taken into account: The head at the valve over time, the void fraction at the valve over time, and the total amount of vapour/gas in the pipe over time, $V_{cav,total}$ and $V_{g,total}$. The reason for including the void fraction and the total amount of vapour/gas in the pipe is because there can be problems with an increased amount of vapour/gas as the number of reaches increases [25]. It is possible to see which mesh has been chosen for each friction model and each two phase model in Table 7.2. It can be seen that the unsteady friction models agree on which mesh is sufficient for the simulations, while the quasi-steady friction model requires a more refined mesh.

Table 7.2: Number of reaches in the appropriate mesh for each friction model.

Friction models	DVCM	DGCM
Quasi-steady	96	96
Brunone	48	48
Vardy & Brown	48	48

For DVCM with the quasi-steady friction model (see Fig. 7.6), the mesh with 96 reaches were chosen because it produced the highest head at the second high pressure zone. There were no consistency for the head when the number of reaches was increased, and therefore the mesh with the highest head was chosen. If the mesh with the head closest to the experimental data were to be chosen, then the mesh with 6 reaches should be chosen. For α , it was observed that when the number of reaches increased, the void fraction also increased, together with the amount of numerical oscillation. However, it was not accompanied with an increase in total amount of vapour, which actually stayed relatively constant. This could indicate that more of the total amount of vapour is formed at the valve.

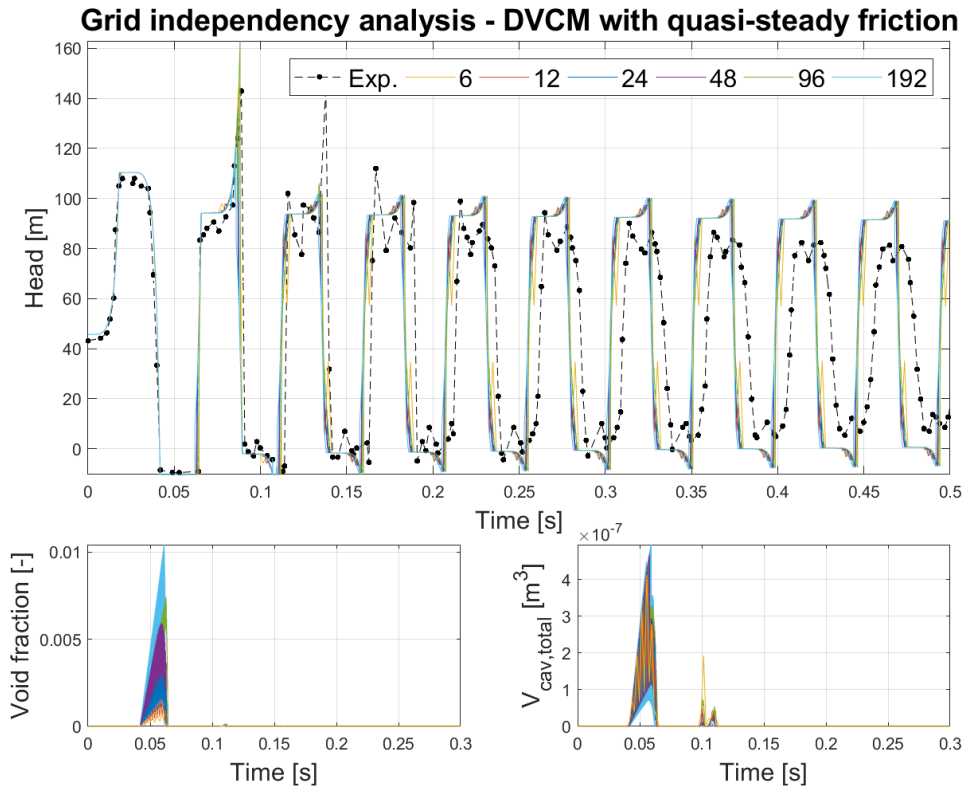


Figure 7.6: Grid independency analysis of case 2 with DVCM using the quasi-steady friction model.

For DVCM with Brunone’s unsteady friction model (see Fig. 7.7), the mesh with 48 reaches was chosen because of a relatively small difference in head and total vapour volume between the mesh with 48, 96, and 192 reaches. The mesh with 24 reaches were not chosen because it had a lower head at the second high pressure zone, compared to the mesh with 48 reaches. When looking at α , there were no consistency for what happened when the number of reaches were increased. An increase was seen when the number of reaches were increased from 6 to 24, followed by a marginal decrease for 48 reaches. α then remained relatively stable for 96 reaches before a significant decrease with 192 reaches. Despite this inconsistency in α , the total amount of vapour still remained relatively constant when the amount of reaches increased.

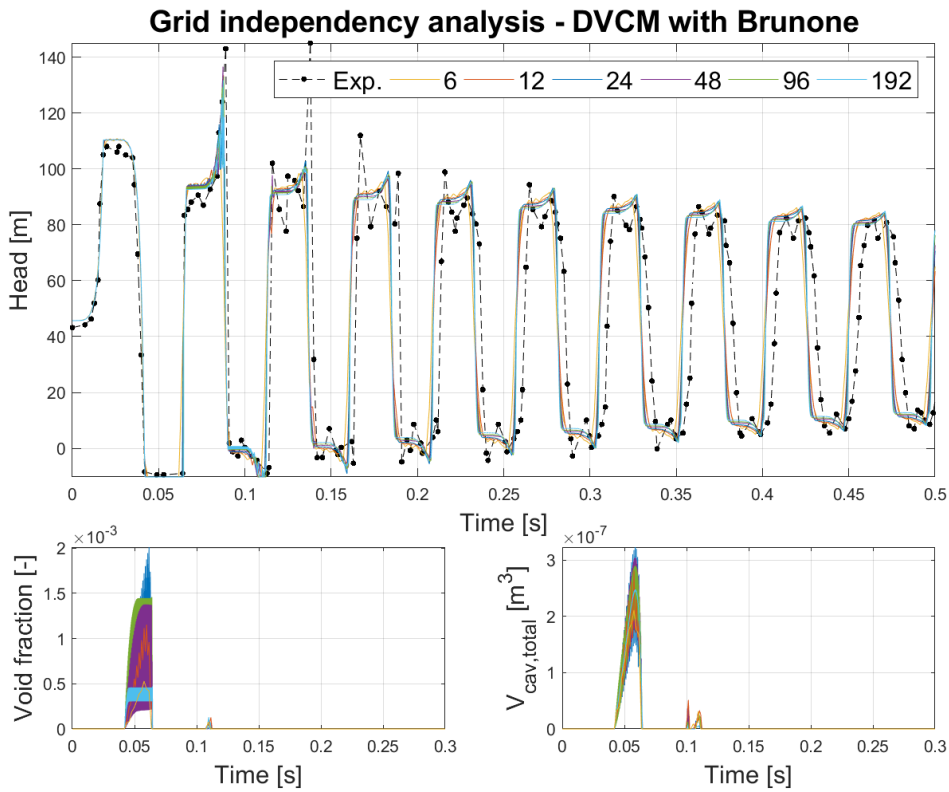


Figure 7.7: Grid independency analysis of case 2 with DVCM using Brunone’s unsteady friction model.

For DVCM with Vardy & Brown’s unsteady friction model (see Fig. 7.8), the mesh with 48 reaches was chosen because of a relatively small difference in head and total vapour volume between the mesh with 48 and 192 reaches. The mesh with 24 reaches was not chosen because of the same reason as with DVCM using Brunone’s unsteady friction model, lower head at the second high pressure zone. The mesh with 96 reaches was not chosen because the head was higher at the second high pressure zone, compared to the mesh with 48 reaches. When looking at α , it was seen that as the amount of

reaches increased, the size of α also increased, which was also seen for DVCM using the quasi-steady friction model. The amount of numerical oscillation for α also increased as the amount of reaches increased. This behaviour for Vardy & Brown's unsteady friction model was also seen for the other unsteady friction models, which were used in the previous work (Zielke [16] and Zarzycki [26]), and it could indicate that for DVCM with convolution based unsteady friction, the void fraction increases as the amount of reaches increases. However, because the total amount of gas is constant for all used meshes, it seems like the amount of gas is distributed in another way, with more gas coalescing at the valve.

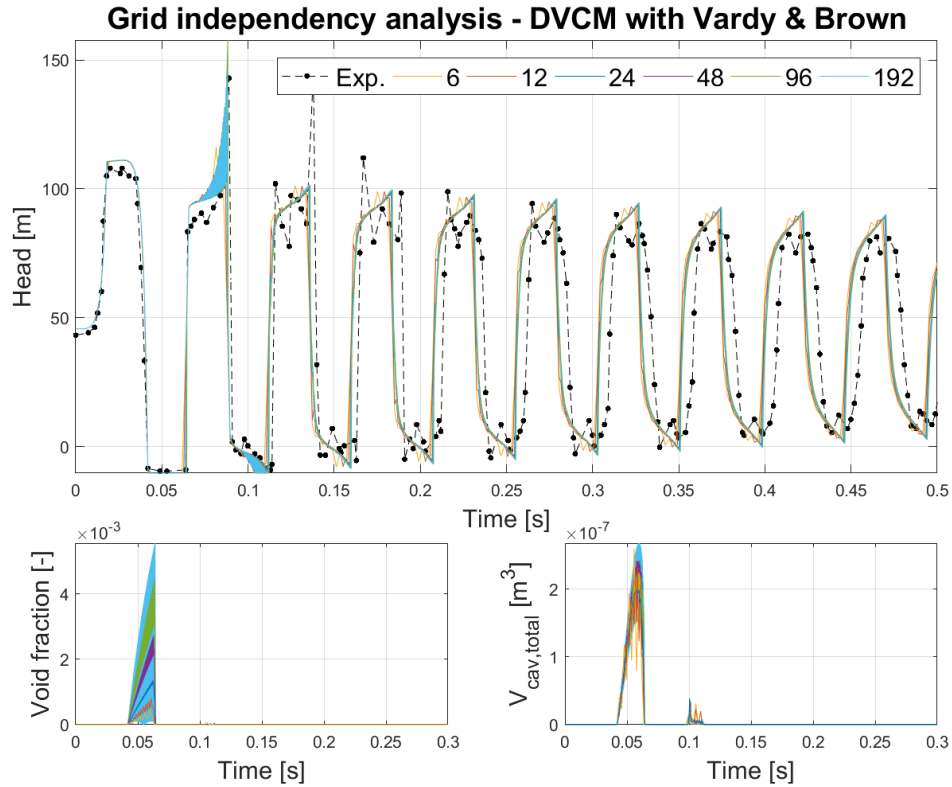


Figure 7.8: Grid independency analysis of case 2 with DVCM using Vardy & Brown's unsteady friction model.

For DGCM with the quasi-steady friction model (see Fig. 7.9), the mesh with 96 reaches was chosen because of a relatively small difference in head and total gas volume between the mesh with 96 and 192 reaches. The mesh with 48 reaches was not chosen because of a higher head at the first peak than on the third high pressure zone, compared to the mesh with 96 reaches. When looking at α and $V_{cav,total}$, the same tendency as for DVCM using quasi-steady friction was observed. However this time, there were almost no oscillation for the mesh with 192 reaches.

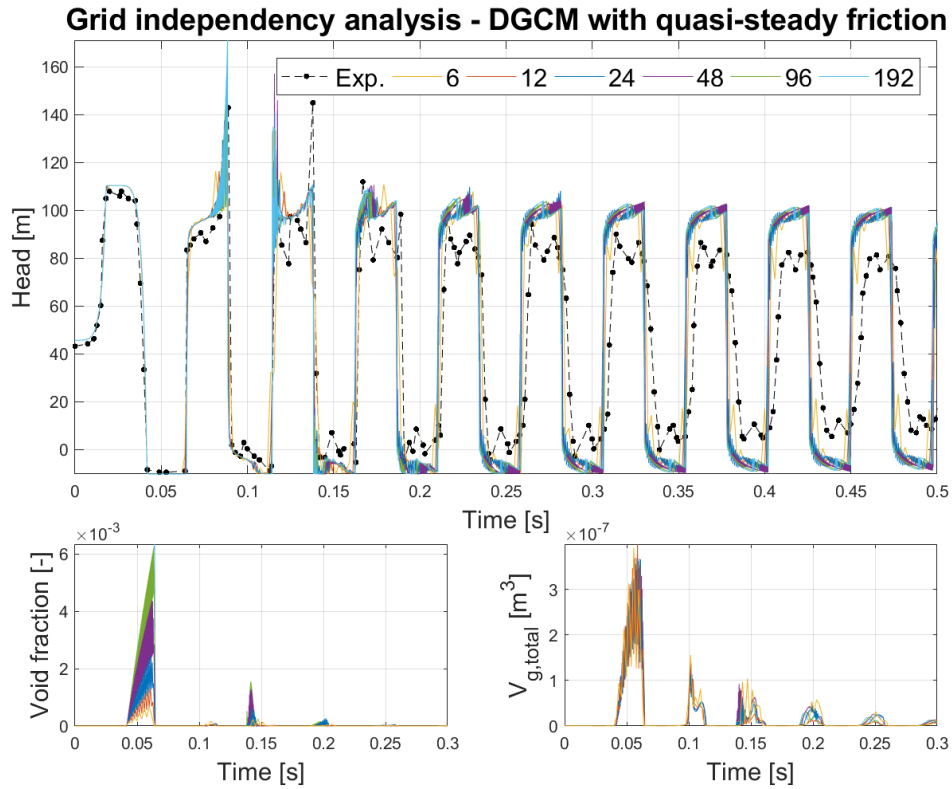


Figure 7.9: Grid independency analysis of case 2 with DGCM using the quasi-steady friction model.

For DGCM with Brunone’s unsteady friction model (see Fig. 7.10), the mesh with 48 reaches were chosen. However, like with DVCM using quasi-steady friction, there was no clear convergence for the second high pressure zone when the amount of reaches was increased. There was however, a convergence on the third high pressure zone, where the first peak became smaller and smaller as the amount of reaches increased. The mesh with 48 reaches was therefore chosen because it shared roughly the same size of head at the second high pressure zone, while also having a relatively small first peak on the third high pressure zone. For α , the same tendency as for DVCM using Brunone’s unsteady friction model was observed, i.e. no consistency in size when the number of reaches increased. For the total amount of gas, a roughly constant amount was observed when increasing the number of reaches, but with a decrease in numerical oscillation (except for the mesh with 6 reaches).

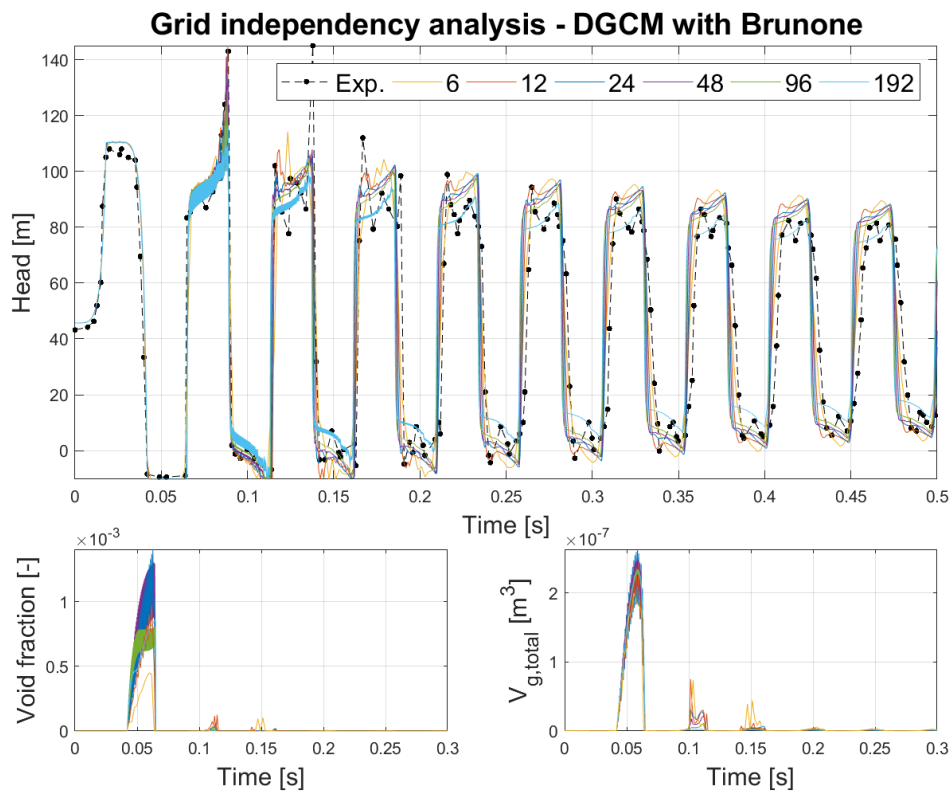


Figure 7.10: Grid independency analysis of case 2 with DGCM using Brunone’s unsteady friction model.

For DGCM with Vardy & Brown's unsteady friction model (see Fig. 7.11), the mesh with 48 reaches was chosen because of relatively small difference in head, α , and total gas volume between the mesh with 48 og 96 reaches. The mesh with 24 reaches was not chosen because of a lower head at the second high pressure zone, compared to the mesh with 48 reaches. For α , the same tendency as for DGCM using Brunone's unsteady friction model was observed. However, this time the amount of numerical oscillation was significantly less. For the total amount of gas, a relatively constant amount of gas was observed when increasing the amount of reaches, with the amount of numerical oscillation decreasing.

The behaviour for DGCM using Vardy & Brown's unsteady friction model was, as with DVCM, the same for the other convolution based friction models used in the previous work. This could indicate that for both DVCM and DGCM, the choice of convolution based unsteady friction model is of less importance when modelling a two phase water hammer.

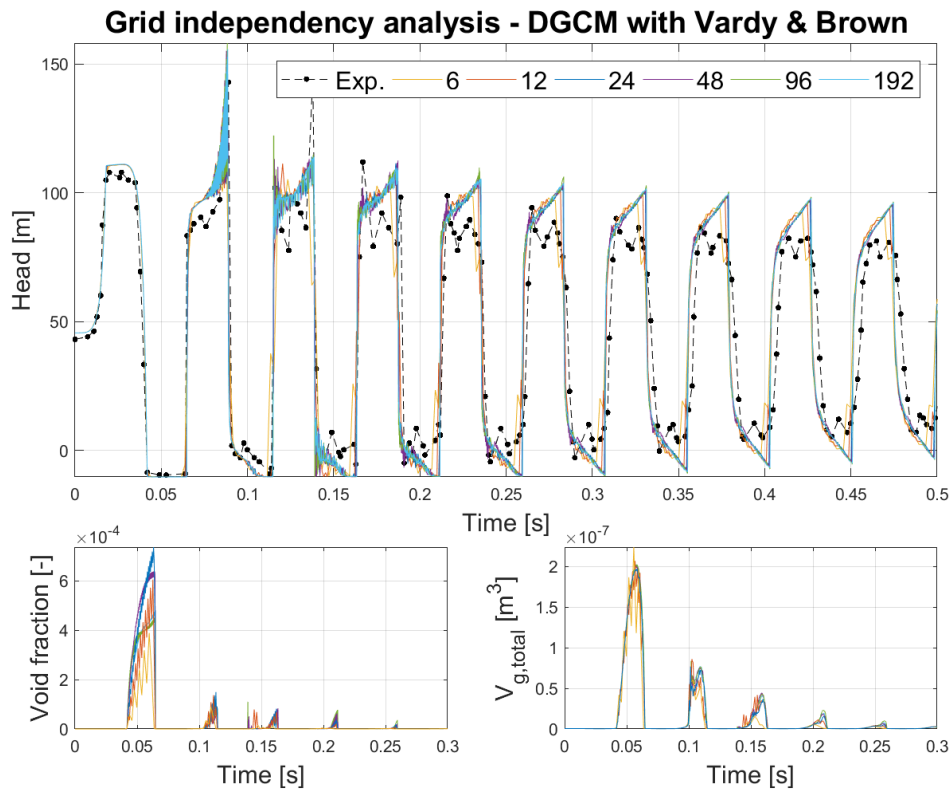


Figure 7.11: Grid independency analysis of case 2 with DGCM using Vardy & Brown's unsteady friction model.

7.3.2. COMPARISON OF FRICTION MODELS

The highest peak on each high pressure zone is determined, via Matlab, and the time and size of the pressure peaks are noted.

The time between each high pressure peak is compared to the experimental data, and the results for DVCM are summarized in Table 7.3. It can be seen that the average time period, between each high pressure peak, is similar for the experiment and all of the friction models at approximately 0.049s. When looking at the largest and smallest time period, it can be seen that there is some disagreement between the experimental data and the simulations. The difference in the largest time period can be attributed to the placement of the peak on the first high pressure zone, see Fig. 7.12 and Fig. 7.13. For the experiment, the first high pressure zone is comprised of a quick increase in pressure, followed by a small decrease before the pressure quickly falls down into the cavitation zone. The simulations are comprised of a quick increase in pressure followed by a small increase, before the pressure quickly falls down into the cavitation zone. The difference in the smallest time period can be attributed to the difference in the fourth high pressure zone, where the experiment has two peaks, while the simulations only have one peak. The largest of the peaks, for the experiment, is the first one, and therefore it is used for calculating the time period. This first peak happens earlier than in the simulations and therefore the time period is smaller.

Table 7.3: Time of period of oscillation - DVCM

Friction models	Largest	Average	Smallest
Experiment [s]	0.0690	0.0489	0.0290
Quasi-Steady [s]	0.0614	0.0485	0.0460
Brunone [s]	0.0604	0.0487	0.0478
Vardy & Brown [s]	0.0602	0.0484	0.0475

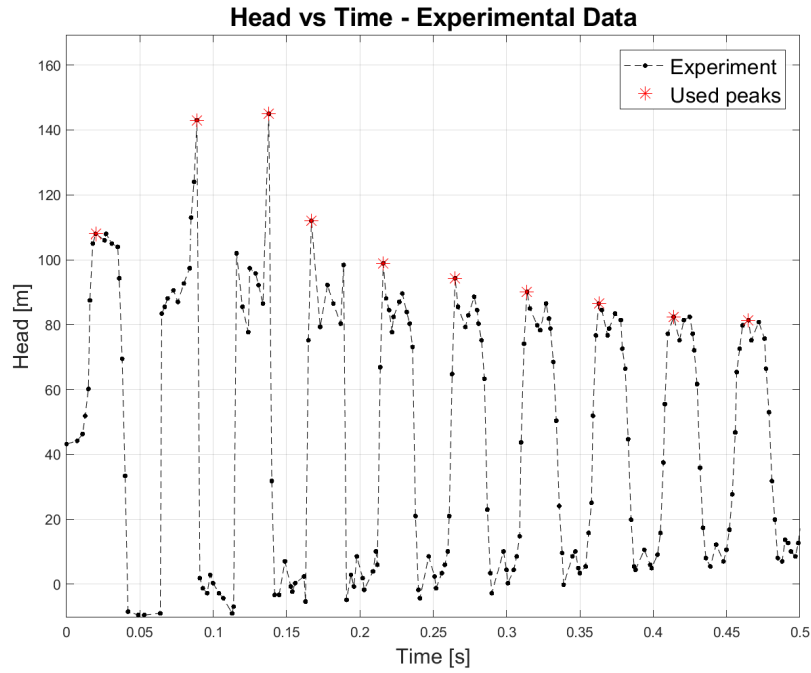


Figure 7.12: The peaks used by the experiment for the comparison with MOC.

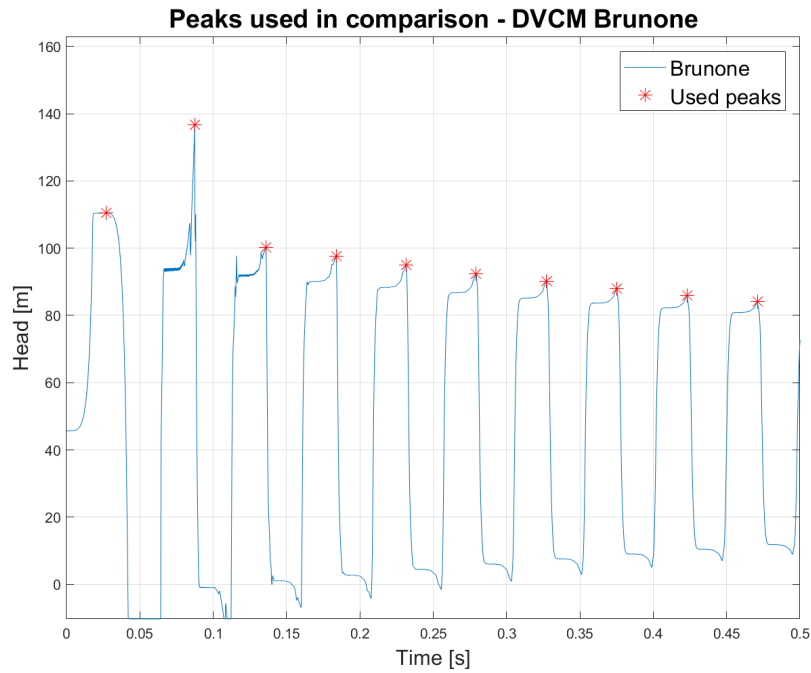


Figure 7.13: The peaks used by DVCM, using Brunone, for the comparison.

The size of the pressure peaks are also compared to the experimental data, and the results for DVCM are summarized in Table 7.4. The deviation from the experimental data is illustrated in Fig. 7.14 and it can be seen that for the first peak, all of the friction models give nearly the same results. For the second peak, it can be seen that Brunone is slightly more accurate than Vardy & Brown, but the deviation from Vardy & Brown is positive rather than Brunone, which has a negative deviation. For the third peak, it can be seen that non of the friction models accurately describe the head, which is due to the fact that the experiment has its largest peak here. This is not the case for the simulations and therefore non of them can accurately describe this peak. It can however be seen that the quasi-steady and Vardy & Brown's friction models have a higher head at the second peak (+12.4% and +4.8% respectively), which is advantageous for dimensioning purposes. For the fourth and fifth peak, all friction models give similar results, and from the sixth peak Brunone give the most accurate results. As expected, the quasi-steady friction model is not able to describe the dampening of the pressure and it therefore gives the least accurate results from the sixth peak. When the flow time was increased to 0.9s, it was seen that Brunone and Vardy & Brown each converged to a deviation of roughly +2.5% and +11% respectively, while quasi-steady continued to increase in deviation (+31% at peak 15).

Table 7.4: Difference in head at peaks - DVCM

Peak	Experiment	Quasi-steady		Brunone		Vardy & Brown	
	Head [m]	Head [m]	Deviation [%]	Head [m]	Deviation [%]	Head [m]	Deviation [%]
1	108.00	110.44	2.26	110.46	2.27	111.17	2.93
2	143.00	162.96	13.96	136.59	-4.48	151.98	6.28
3	145.00	106.11	-26.82	100.28	-30.84	101.40	-30.07
4	112.00	101.47	-9.40	97.55	-12.90	99.48	-11.18
5	98.90	101.08	2.20	94.90	-4.05	97.65	-1.27
6	94.30	100.68	6.77	92.34	-2.08	95.90	1.69
7	90.10	100.30	11.32	90.08	-0.03	94.27	4.63
8	86.50	99.92	15.51	88.01	1.74	92.70	7.17
9	82.40	99.54	20.80	86.01	4.38	91.17	10.65
10	81.40	99.17	21.83	84.02	3.22	89.68	10.17

Based on the comparison of the time period between oscillations and the deviation in the head, it is concluded that Vardy & Brown's unsteady friction model is the best friction model to use with DVCM, because it has a relatively low amount of deviation (converges at +11%), and it is the friction model which most accurately describe the head of the largest peak (+4.8%), even though the peak is not located in the same high pressure zone (experiment at the third zone and Vardy & Brown at the second zone).

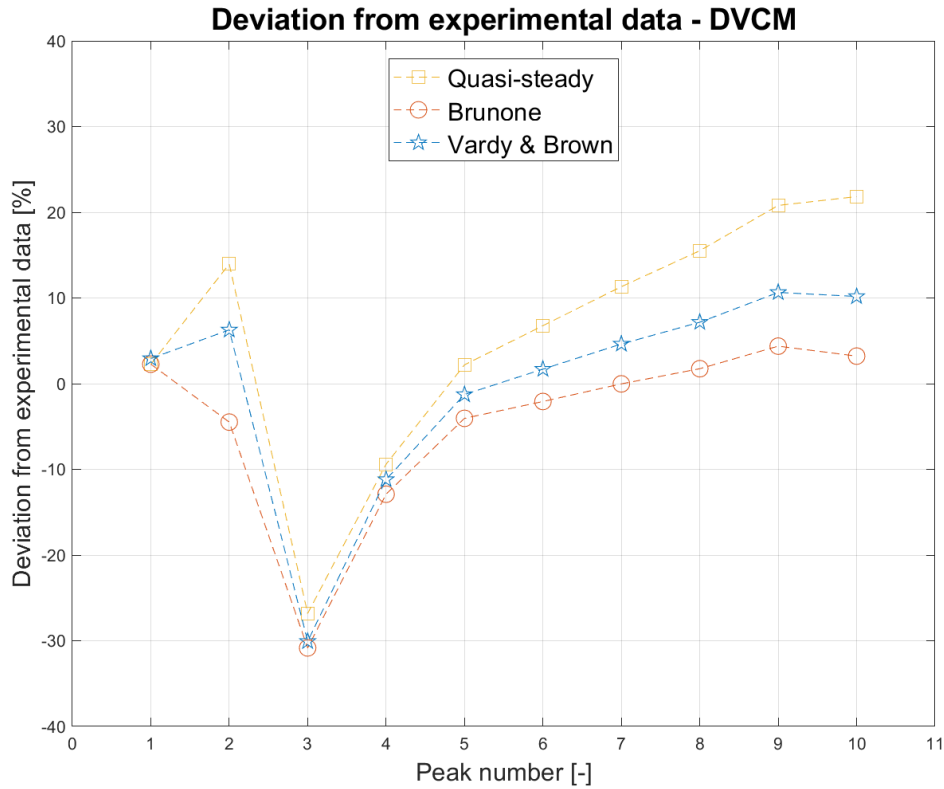


Figure 7.14: Deviation of MOC, using DVCM, from the experimental data.

For DGCM, the results of the time between each high pressure peak is shown in Table 7.5. It can be seen that the average time period, between each high pressure peak, is similar for the experiment and all of the friction models at approximately 0.049s. When looking at the largest and smallest time period, it can be seen that there is some disagreement between the experimental data and the simulations. The difference in the largest time period can be attributed to the same problem as with DVCM. For the smallest time period, the difference can be attributed to the difference in the third high pressure zone. The experimental data, and the simulations, all have two peaks on the third high pressure zone, unlike DVCM, but it is only for quasi-steady that the first of the two peaks are the highest, as was also the case for the experiment, see Fig. 7.15, while for Brunone and Vardy & Brown, the second peak is the highest, see Fig. 7.16.

Table 7.5: Time of period of oscillation - DGCM

Friction models	Largest	Average	Smallest
Experiment [s]	0.0690	0.0489	0.0290
Quasi-Steady [s]	0.0617	0.0484	0.0272
Brunone [s]	0.0609	0.0487	0.0475
Vardy & Brown [s]	0.0599	0.0487	0.0465

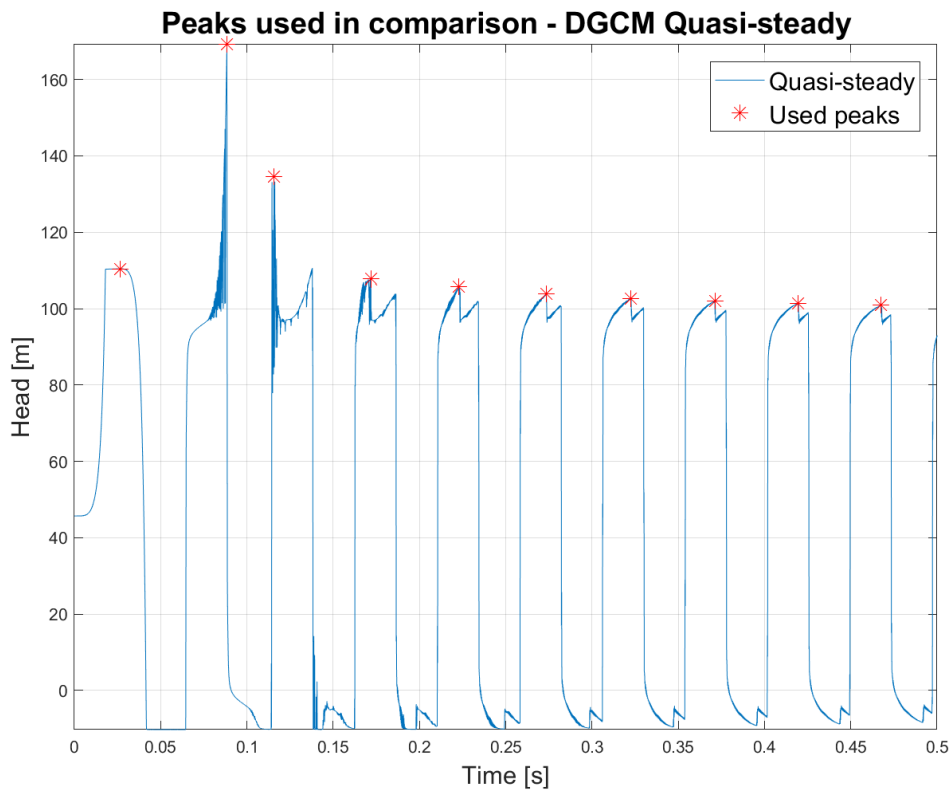


Figure 7.15: The peaks used by DGCM, using quasi-steady friction, for the comparison.

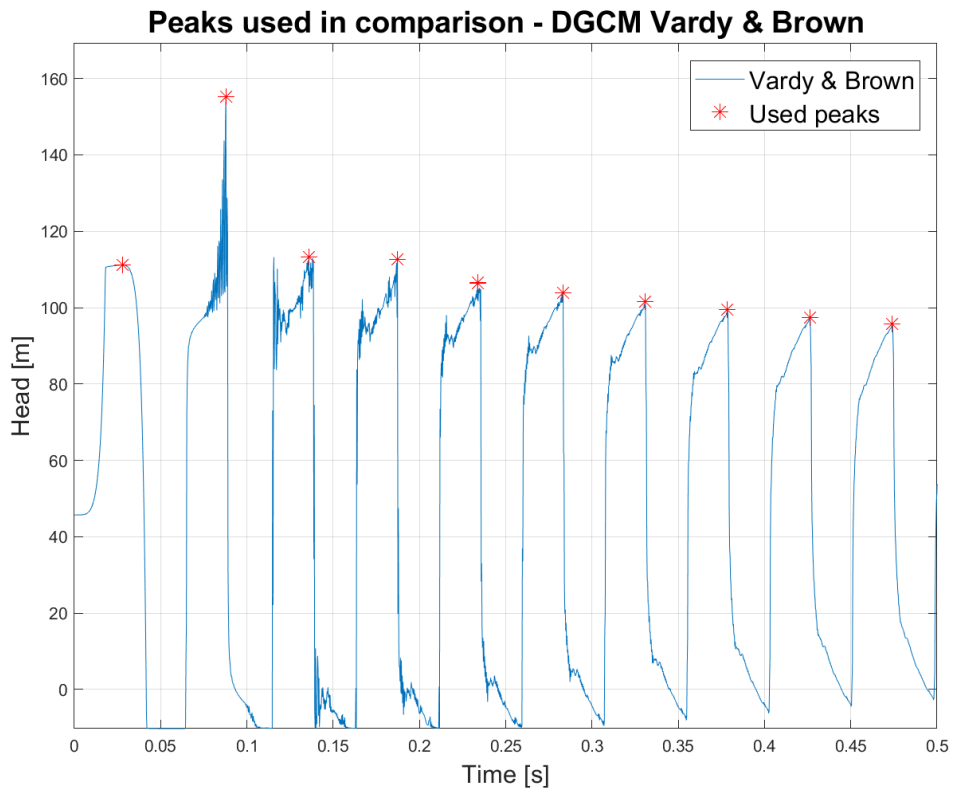


Figure 7.16: The peaks used by DGCM, using Vardy & Brown, for the comparison.

The size of the pressure peaks, for DGCM, are compared to the experimental data in Table 7.6, and the deviation from the experimental data can be seen in Fig. 7.17. It can be seen that for the first peak, all of the friction models give nearly the same results. For the second peak, it can be seen that Brunone is the most accurate model, with a slight underestimation of the head, while the remaining two models overestimate the head. For the third peak, it can be seen that non of the friction models can accurately describe the head. This is again due to the problem with the experiment having the highest head at the third peak, and again it can be seen that quasi-steady and Vardy & Brown have a higher head at the second peak (+16.7% and +7% respectively). This is again advantages for dimensioning purposes. For the fourth peak, Vardy & Brown is the most accurate model, with a slight overestimation of the head. From the fifth peak and onwards, Brunone is the most accurate model, with an overestimation of less than +10%. It is not as clear as with DVCM, but quasi-steady friction is again not able to describe the dampening of the pressure and therefore gives the least accurate results. When the flow time was increased to 0.9s, it was seen that Brunone and Vardy & Brown each converged to a deviation of roughly +6.4% and +18% respectively, while quasi-steady continued to increase in deviation (+33% at peak 15).

Table 7.6: Difference in head at peaks - DGCM

Peak	Experiment	Quasi-steady		Brunone		Vardy & Brown	
	Head [m]	Head [m]	Deviation [%]	Head [m]	Deviation [%]	Head [m]	Deviation [%]
1	108.00	110.44	2.26	110.45	2.27	111.16	2.93
2	143.00	169.26	18.37	141.10	-1.33	155.16	8.51
3	145.00	134.64	-7.14	107.85	-25.62	113.23	-21.91
4	112.00	107.89	-3.67	101.57	-9.31	112.61	0.54
5	98.90	105.76	6.94	98.76	-0.14	106.64	7.83
6	94.30	103.87	10.15	95.72	1.51	103.87	10.14
7	90.10	102.70	13.98	93.11	3.34	101.52	12.67
8	86.50	102.09	18.02	90.82	4.99	99.44	14.96
9	82.40	101.46	23.13	88.75	7.70	97.49	18.31
10	81.40	100.92	23.98	86.93	6.79	95.67	17.53

Based on the comparison of the time period between oscillations and the deviation in the head, it is concluded that Vardy & Brown's unsteady friction model is the best friction model to use with DGCM, because it is the model which most accurately describes the head at the highest peak (+7%), while still having a relatively acceptable deviation for the remaining peaks (converges at +18%). If the damping period is of primary interest, then Brunone's unsteady friction model should be used (it underestimates the largest peak by -2.7%).

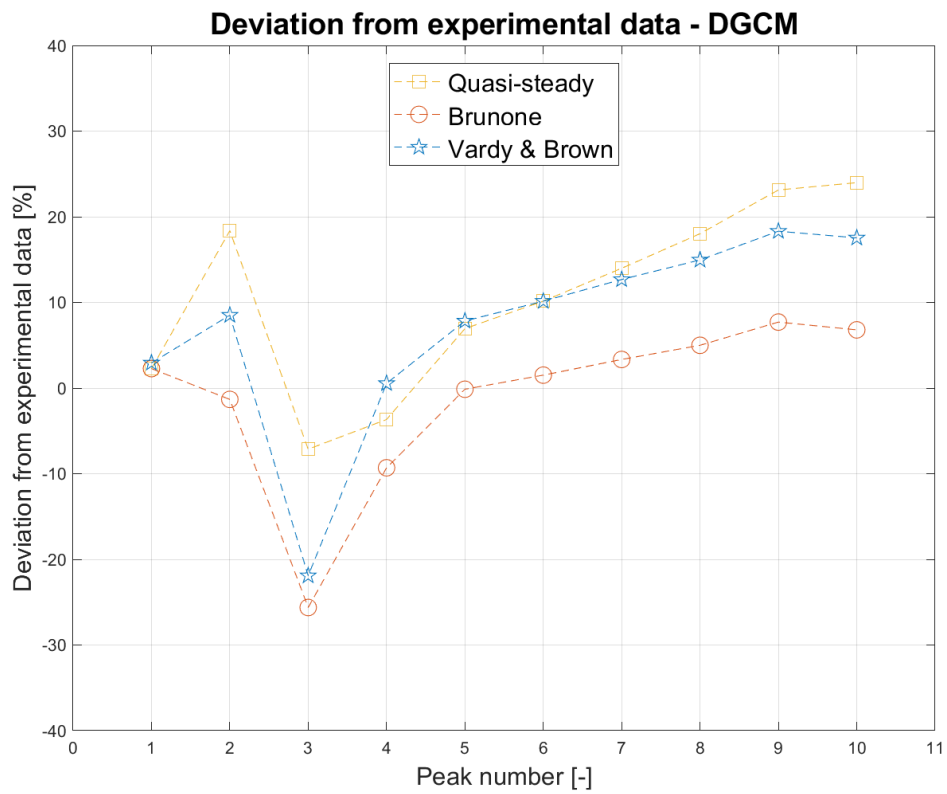


Figure 7.17: Deviation of MOC, using DGCM, from the experimental data.

7.4. MOC SETTINGS - TWO PHASE BERGANT ET AL. - LOW VELOCITY

For Case 3, the same approach as in Sec. 7.3 will be used to determine the valve closure coefficient, m , the weighting factor, ψ , and the number of reaches. m was chosen to 5. When ψ and the number of reaches has been determined, the best friction model for DVCM and DGCM will be compared to the results from the CFD simulations in Sec. 10.2. The ψ values used for the grid independency analysis can be seen in Table 7.7, where it can be seen that for DVCM, all the friction models use the same values. For DGCM however, it can be seen that quasi-steady and Vardy & Brown's friction model both require a higher ψ value compared to Brunone.

Table 7.7: ψ chosen for the grid independency analysis.

Friction models	DVCM	DGCM
Quasi-steady	0.55	0.75
Brunone	0.55	0.55
Vardy & Brown	0.55	0.75

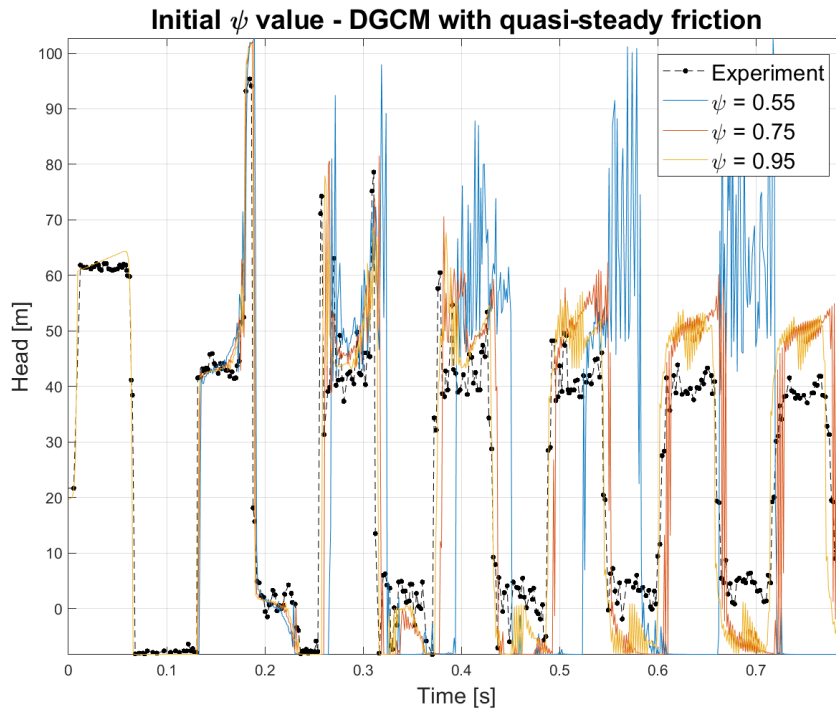


Figure 7.18: Comparison of different ψ values for DGCM with quasi-steady friction.

In Fig. 7.18 it is possible to see the amount of numerical oscillation present for the sim-

ulations with quasi-steady friction for DGCM. It can be seen that there is a relatively high amount of numerical oscillation for all of the simulated ψ values, with $\psi = 0.55$ having a much higher amount. Since it is recommended to have a ψ close to 0.5, 0.75 was chosen rather than 0.95 due to their relatively similar amounts of numerical oscillation.

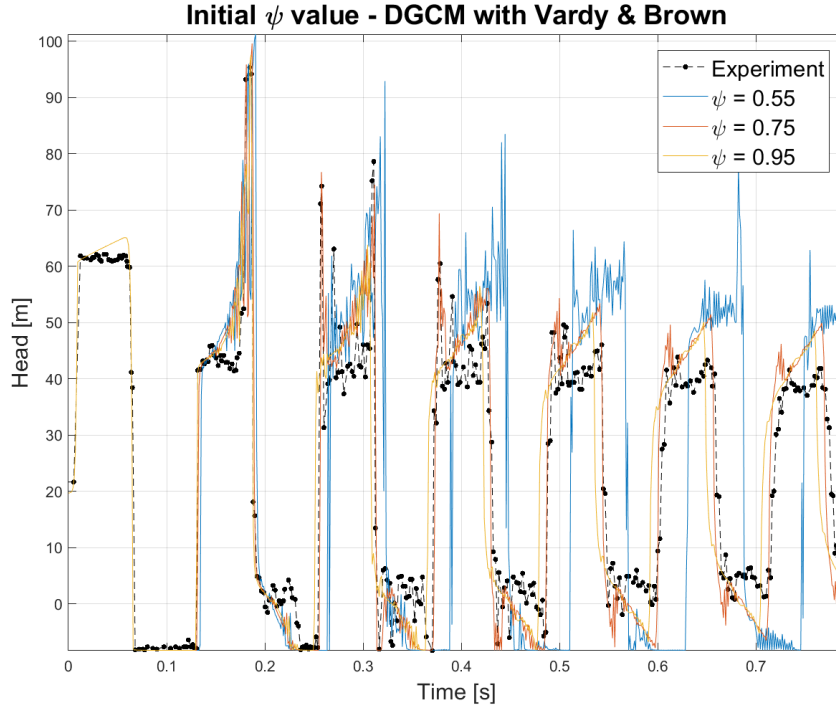


Figure 7.19: Comparison of different ψ values for DGCM with Vardy & Brown.

In Fig. 7.19 it is possible to see the amount of numerical oscillation present for the simulations with Vardy & Brown for DGCM. It can be seen that the amount of numerical oscillation is much lower than for quasi-steady, but there is still a high amount of numerical oscillation for $\psi = 0.55$. It was therefore chosen to use $\psi = 0.75$. The grid independency analysis was conducted in the same fashion as in Sec. 7.3.1 and the results are shown in Table 7.8. A detailed description of the mesh grid independency analysis is available in App. C.1.

Table 7.8: Number of reaches in the appropriate mesh for each friction model.

Friction models	DVCM	DGCM
Quasi-steady	24	24
Brunone	48	24
Vardy & Brown	48	48

7.4.1. COMPARISON OF FRICTION MODELS

For the comparison of the friction models, the same approach as in Sec. 7.3.2 will be used. The highest peak on each high pressure zone is determined via Matlab, and the time and size of the pressure peak is noted.

The time between each high pressure peak is compared to the experimental data, and the results for DVCM are summarized in Table 7.9. It can be seen that the average time period between each high pressure peak is relatively similar at approximately 0.12s, with Vardy & Brown having the largest deviation at -6.4% . For the largest and smallest time period, there is some disagreement between the experimental data and the simulations. The problem here is exactly the same as for Case 2 (Sec. 7.3.2), where the position of the highest point on a high pressure zone is very different. It can be seen that the quasi-steady friction model is generally better at replicating the time period between the oscillation, with a deviation of only $+4\%$ for the largest, -4.7% for the average, and $+18\%$ for the smallest time period. Both unsteady friction models have at deviation of -20.1% for the largest, Brunone have -5.5% for the average, and they both have a deviation greater than $+60\%$ for the smallest time period.

Table 7.9: Time of period of oscillation - DVCM

Friction models	Largest	Average	Smallest
Experiment [s]	0.1561	0.1227	0.0676
Quasi-Steady - DVCM [s]	0.1623	0.1170	0.0800
Brunone - DVCM [s]	0.1247	0.1159	0.1129
Vardy & Brown - DVCM [s]	0.1247	0.1149	0.1106

The size of the pressure peaks is also compared to the experimental data, and the results for DVCM are shown in Table 7.10. The deviation from the experimental data is illustrated in Fig. 7.20, and it can be seen that for the two first peaks, both unsteady friction models are very similar in deviation. From the third peak and afterwards, the difference between the unsteady friction models become relatively large with Vardy & Brown being the most accurate for the third to fifth peak, and Brunone for the sixth and seventh. The quasi-steady friction model has a deviation which is almost comparable to the deviation for Vardy & Brown, with the largest difference being at peak 4, where Vardy & Brown has a deviation of -11% while quasi-steady has a deviation of -20% . Unlike with Case 2 (Sec. 7.3.2), it was not possible to see a convergence, for the unsteady friction models, if the flow time was increased, as all of the experimental data was in use. There is an indication of a convergence for both unsteady friction models, with Brunone at -4% and Vardy & Brown at $+12\%$, however more peaks are required to conclude this.

Table 7.10: Difference in head at peaks - DVCM

Peak	Experiment	Quasi-steady		Brunone		Vardy & Brown	
	Head [m]	Head [m]	Deviation [%]	Head [m]	Deviation [%]	Head [m]	Deviation [%]
1	62.13	64.35	3.57	64.37	3.60	65.14	4.84
2	95.37	103.42	8.45	99.10	3.91	99.90	4.75
3	78.62	68.87	-12.40	51.28	-34.77	67.76	-13.80
4	60.50	48.47	-19.88	47.42	-21.61	53.83	-11.02
5	49.60	48.26	-2.70	44.72	-9.85	50.91	2.63
6	43.88	48.06	9.51	42.39	-3.40	48.81	11.22
7	41.84	47.85	14.37	40.17	-3.99	46.84	11.96

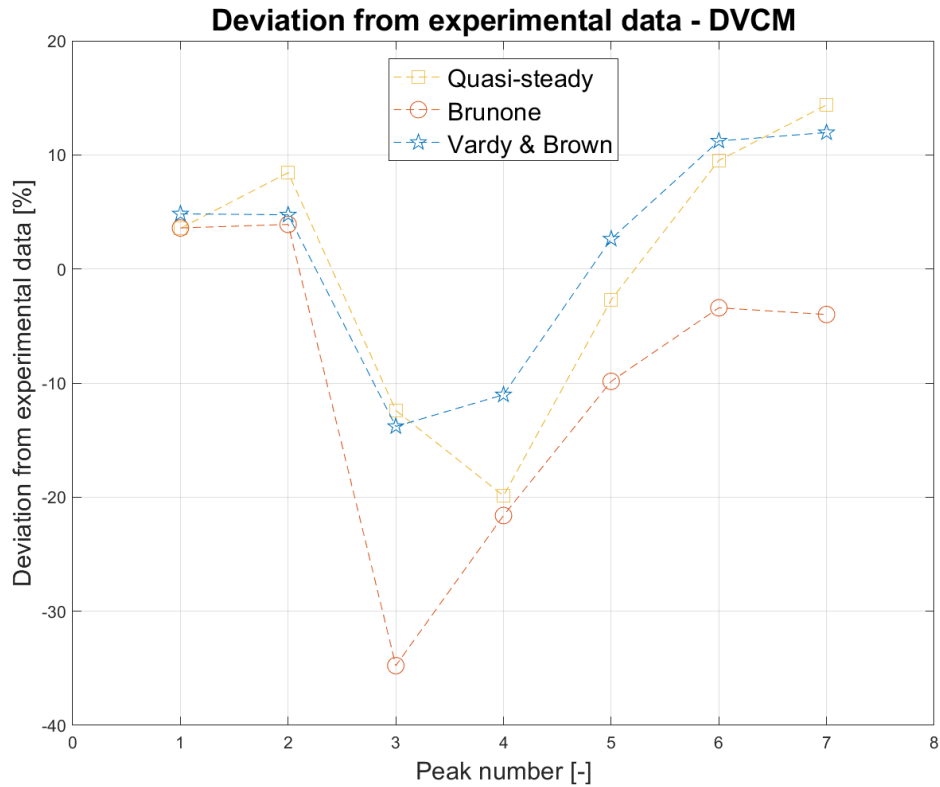


Figure 7.20: Deviation of MOC, using DVCM, from the experimental data.

Based on the comparison of the time period between oscillations and the deviation in the head, it is concluded that Vardy & Brown's unsteady friction model is the best friction model for use with DVCM in this case. This is because it has a lower deviation from the experimental results for the first five peaks.

For DGCM, the results of the time between each high pressure peak is summarized in Table 7.11. It can be seen that the average time period between each high pressure

peak is relatively similar at approximately 0.12s, with Vardy & Brown having the largest deviation at -3.7% . For the largest and smallest time period, there is some disagreement between the experimental data and the simulations. The problem here is exactly the same as for Case 2 (Sec. 7.3.2), where the position of the highest point on a high pressure zone is very different. It can be seen that the quasi-steady friction model is generally better at replicating the time period between the oscillation, with a deviation of only $+7\%$ for the largest, -1.6% for the average, and -2.5% for the smallest time period. When comparing the unsteady friction models, it can be seen that Brunone is slightly more accurate for the largest and average time period with a deviation of -16.4% and -2.7% respectively while Vardy & Brown has -16.7% and -3.7% respectively (both have $+67\%$ for the smallest time period).

Table 7.11: Time of period of oscillation - DGCM

Friction models	Largest	Average	Smallest
Experiment [s]	0.1561	0.1227	0.0676
Quasi-Steady - DGCM [s]	0.1670	0.1207	0.0659
Brunone - DGCM [s]	0.1305	0.1194	0.1129
Vardy & Brown - DGCM [s]	0.1300	0.1182	0.1129

The size of the pressure peaks is also compared to the experimental data, and the results for DGCM are shown in Table 7.12. The deviation from the experimental data is illustrated in Fig. 7.21, and it can be seen that for the first two peaks, all three friction models are relatively similar in deviation, with quasi-steady being slightly larger. For the third peak, it can be seen that all of the friction models are still relatively similar, not accounting for \pm , with Brunone having the largest deviation. From the fourth peak and onwards, both unsteady friction models have a similar deviation, with Vardy & Brown being the most accurate at the fourth peak, and Brunone being slightly better from the fifth peak and onwards. The deviation for the quasi-steady friction model increases greatly from the fourth peak to the sixth peak, followed by a small decrease. As for DVCN, it is not possible to see a convergence for the unsteady friction model in DGCM. It might be possible to see a slight indication of a convergence, with Brunone at $+17\%$ and Vardy & Brown at $+20\%$, but it is not possible to be certain.

Table 7.12: Difference in head at peaks - DGCM

Peak	Experiment		Quasi-steady		Brunone		Vardy & Brown	
	Head [m]	Head [m]	Head [m]	Deviation [%]	Head [m]	Deviation [%]	Head [m]	Deviation [%]
1	62.13	64.35	64.35	3.56	64.50	3.81	65.13	4.83
2	95.37	102.29	102.29	7.25	99.39	4.22	99.69	4.53
3	78.62	81.58	81.58	3.78	70.42	-10.42	84.60	7.61
4	60.50	70.60	70.60	16.70	59.46	-1.72	60.21	-0.48
5	49.60	62.39	62.39	25.78	52.70	6.24	53.49	7.84
6	43.88	60.21	60.21	37.22	50.72	15.59	51.31	16.94
7	41.84	56.40	56.40	34.79	48.85	16.76	50.03	19.57

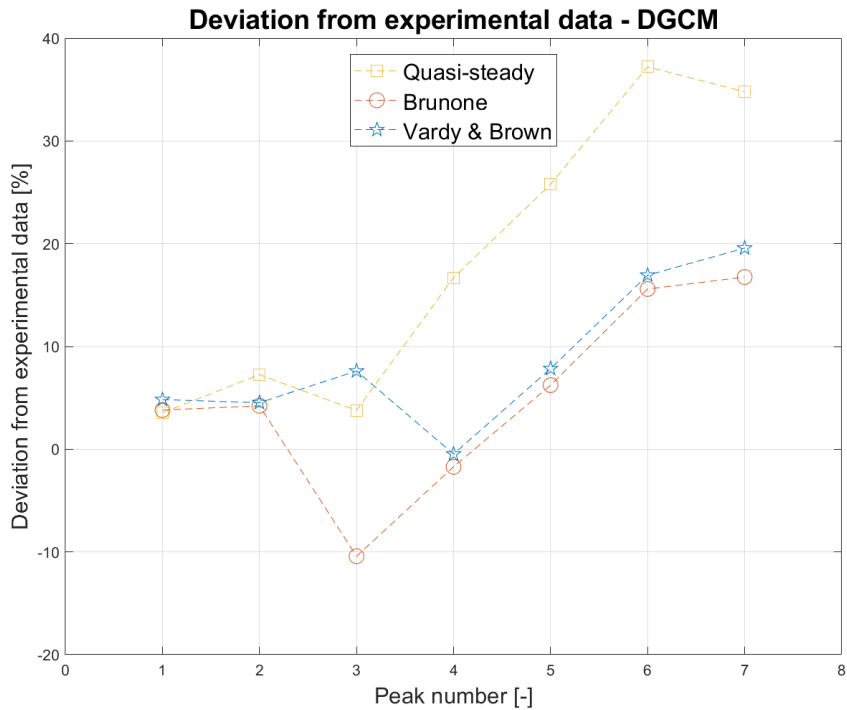


Figure 7.21: Deviation of MOC, using DGCM, from the experimental data.

Based on the comparison of the time period between oscillations and the deviation in the head, it is concluded that Vardy & Brown's unsteady friction model is the best friction model for use with DGCM in this case. This is because of a lower deviation at the third peak, compared to Brunone (+7.6% vs -10.4% respectively), and the relatively small difference in deviation afterwards (+20% vs +17% respectively).

7.5. MOC SETTINGS - TWO PHASE BERGANT - HIGH VELOCITY

For Case 4, the same approach as in Sec. 7.3 will be used to determine the valve closure coefficient, m , the weighting factor, ψ , and the number of reaches. m was chosen as 5. When ψ and the number of reaches has been determined, the best friction model for DVCM and DGCM will be compared to the results from the CFD simulations in Sec. 10.3.

Unlike for the previous two cases, for this case a number of problems were observed for DVCM together with some unexpected behaviour for both DVCM and DGCM. One of the unexpected behaviours for both DVCM and DGCM are related to the time period between each high pressure zone. The only difference between Case 3 and 4, which uses the exact same setup, is the inlet velocity, and from this it was assumed that the time period between each high pressure zone should be relatively similar. However, this was not the case, which can be seen in Fig. 7.22, where the experimental data from Case 3 and 4 are plotted together. It can be seen that for Case 3 (Low velocity), the water hammer moves way faster than in Case 4 (High velocity), with Case 3 having three times as many high pressure zones per second. This indicates that the amount of vapour/gas produced during cavitation, in Case 4, is of such great magnitude that the wave speed is severely reduced.

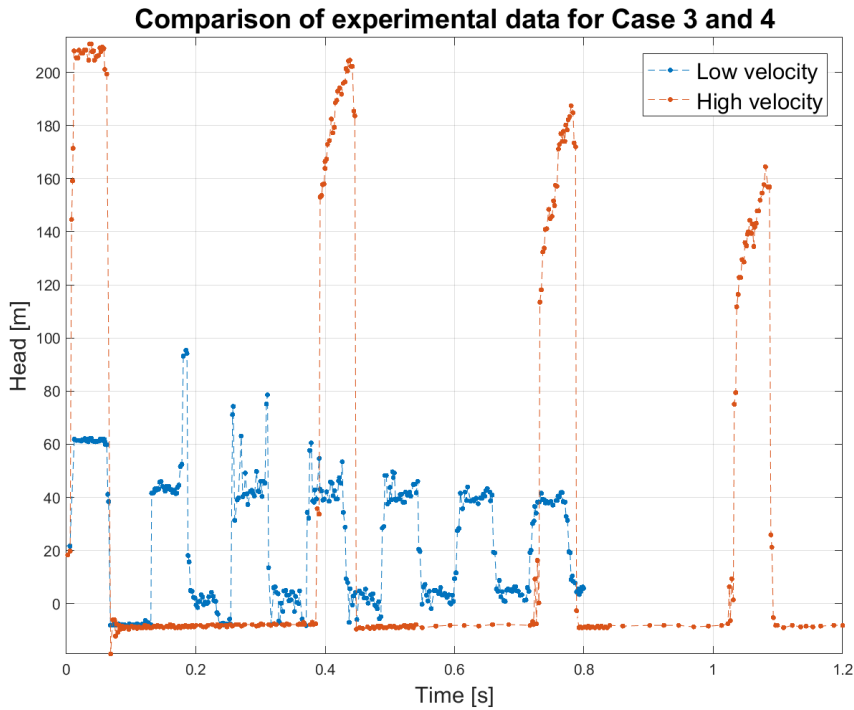


Figure 7.22: Comparison of experimental data from case 3 and 4, which uses the exact same setup, but with different inlet velocities.

This could (and did for DVCM) result in problems for DVCM and DGCM, because both models assume that the vapour/gas is coalesced together in each reach, therefore assuming a constant single phase wave speed, because the vapour/gas pockets are of a relatively small size. In Fig. 7.23 it can be seen that none of the friction models, when using DVCM, can accurately describe the experiment. It can be seen that for the second high pressure zone, DVCM is very accurate, but after this, all of the friction models have too much damping, which is believed to be the reason for the smaller distance between each high pressure zone. Because of this major difference between the experimental data and the simulations, it is concluded that DVCM is not suited for use in this case, and will therefore not be considered for Case 4.

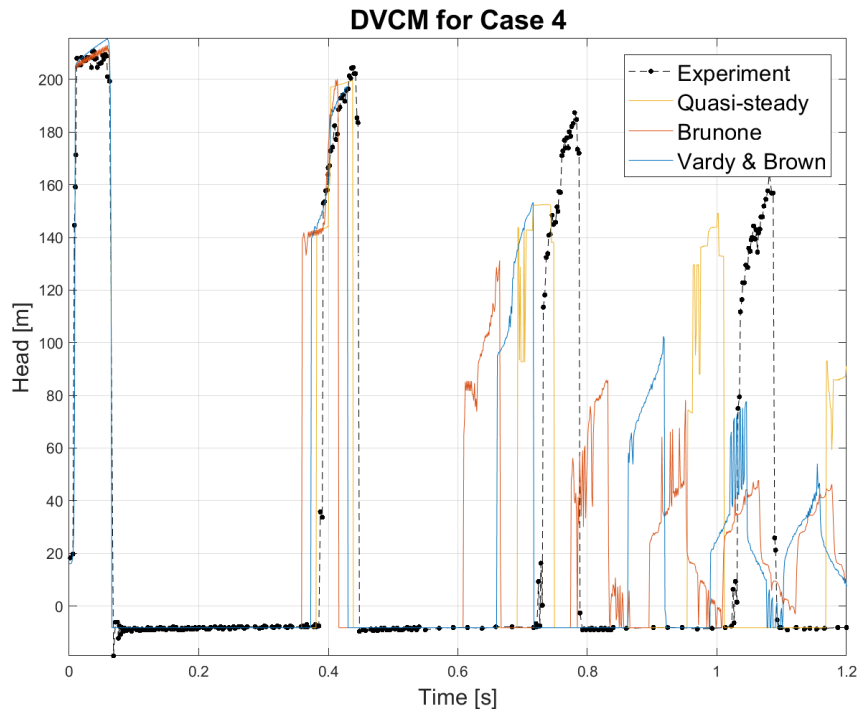


Figure 7.23: The friction models used together with DVCM is compared to the experimental data.

Another unexpected behaviour for both DVCM and DGCM is the way the void fraction at the valve develops during the periods with cavitation (see Fig. 7.24). It was expected that the void fraction would continuously increase until the pressure increase. However, this was not the case and it was observed that the void fraction started to decrease after 0.25 seconds. This response seems strange because the pressure is still at the vaporization pressure and the pressure wave should just have left the reservoir. However, others have documented a similar response from another model and an experiment [27].

In Table 7.13 it is possible to see the chosen ψ value for the grid independency analysis, and it can be seen that the quasi-steady friction model has been omitted. The reason

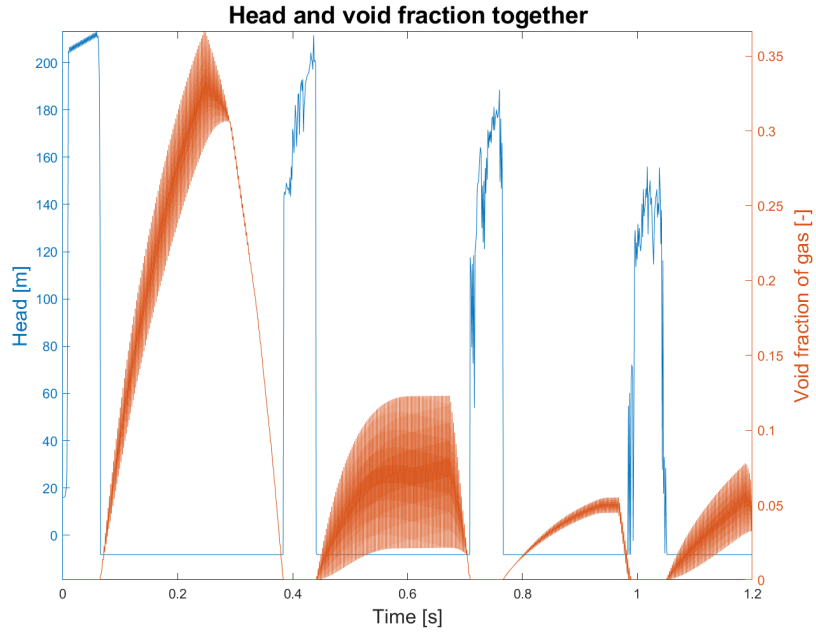


Figure 7.24: The head and void fraction obtained with DGCM.

Table 7.13: ψ chosen for the grid independency analysis.

Friction models	DGCM
Brunone	0.55
Vardy & Brown	0.55

for omitting the quasi-steady friction model is due to an excessive amount of numerical oscillation independent of the chosen value of ψ .

ψ was set to 0.55 for both Brunone and Vardy & Brown because the amount of numerical oscillation was relatively low. The grid independency analysis was conducted in the same fashion as in Sec. 7.3.1 and the results are shown in Table 7.14. A detailed description of the grid independency analysis is available in the App. sec. C.2.

Table 7.14: Number of reaches in the appropriate mesh for each friction model.

Friction models	DGCM
Brunone	24
Vardy & Brown	24

7.5.1. COMPARISON OF FRICTION MODELS

For the comparison of the friction models, the same approach as in Sec. 7.3.2 will be used.

The time between each high pressure peak is compared to the experimental data, and the results are summarized in Table 7.15 (unlike in previous sections, here it is first, second, and third period, not largest, average, and smallest). As with the other cases, there are still some problems with the placement of the highest point on the experimental data, which results in the first time period being a little longer for the experiment, compared to the simulations. For the second and third period the problem with placement of the highest peak might be the reason for the difference between the experiment and Vardy & Brown. Brunone however, seems to have more damping than the experimental data and Vardy & Brown, and this could result in a smaller time period (see Fig. 7.25).

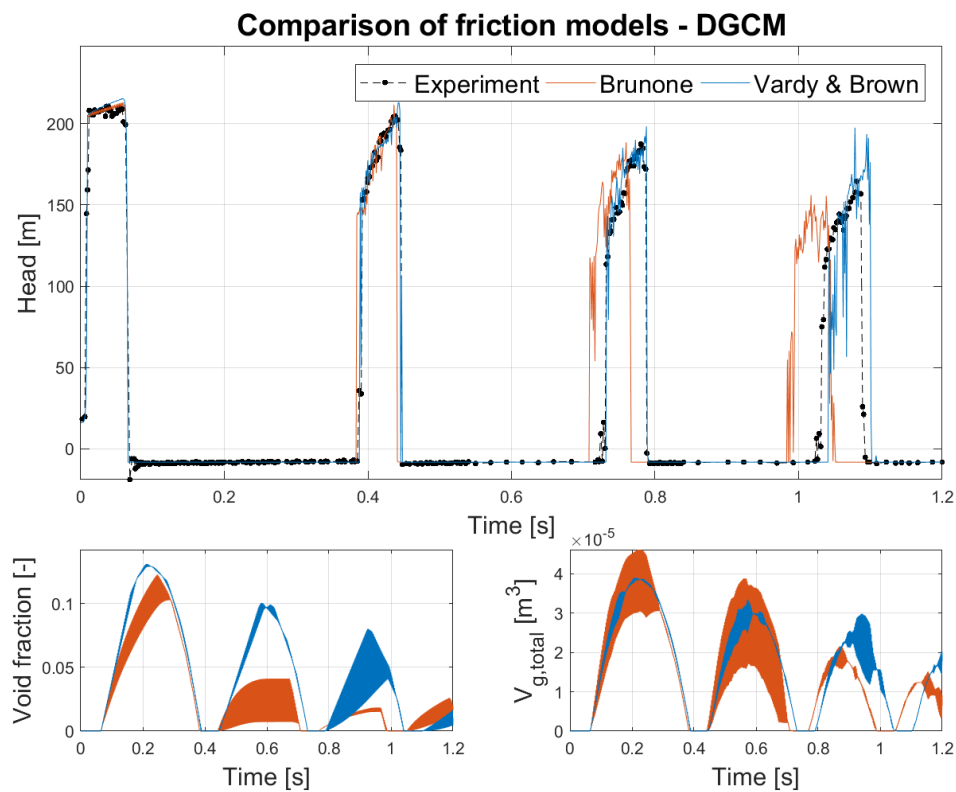


Figure 7.25: Experimental data, DGCM using Brunone, and DGCM using Vardy & Brown plotted together.

Table 7.15: Time of period of oscillation - DGCM

Friction models	First	Second	Third
Experiment [s]	0.4024	0.3420	0.3005
Brunone - DGCM [s]	0.3775	0.3234	0.2576
Vardy & Brown - DGCM [s]	0.3846	0.3446	0.2905

The size of the pressure peaks is also compared to the experimental data, and the results are shown in Table 7.16. The deviation from the experimental data is illustrated in Fig. 7.26, and it can be seen for the two first peaks, that Brunone and Vardy & Brown are relatively similar in deviation. After the second peak, the similarity stops, and it is seen that Vardy & Brown's overestimation increases rapidly in size between the third and fourth peak. Brunone's overestimation becomes of relatively small size for the third peak followed by an underestimation of the fourth peak. It is unknown to which degree Brunone and Vardy & Brown will under- and overestimate the head at the following peaks, and it is therefore difficult to recommend any of the models for other purposes than dimensioning purposes.

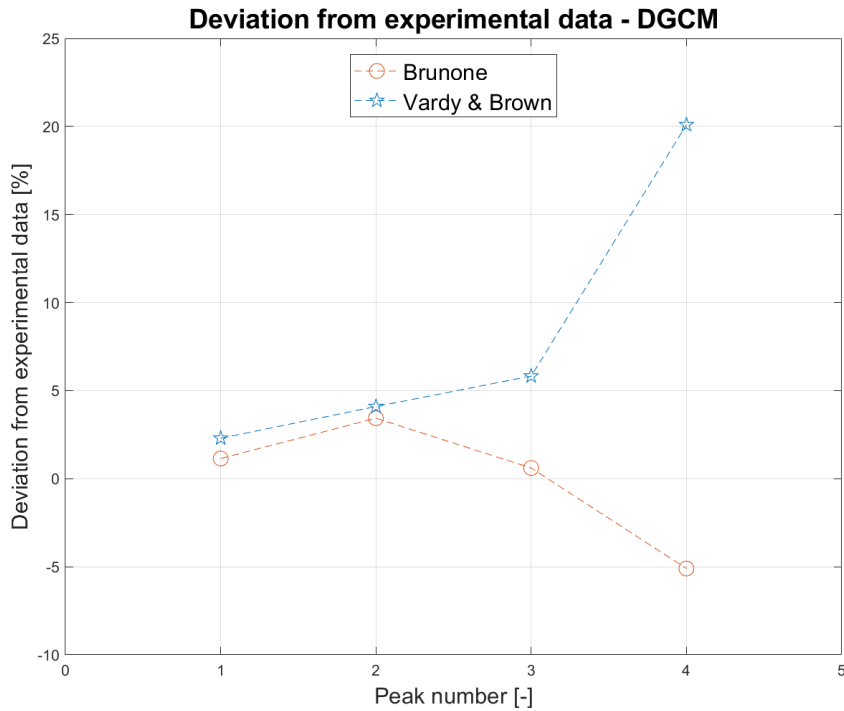


Figure 7.26: Deviation of MOC, using DGCM, from the experimental data.

Table 7.16: Difference in head at peaks - DGCM

Peak	Experiment	Brunone		Vardy & Brown	
	Head [m]	Head [m]	Deviation [%]	Head [m]	Deviation [%]
1	210.69	213.10	1.14	215.53	2.30
2	204.58	211.60	3.44	212.96	4.10
3	187.40	188.54	0.61	198.32	5.83
4	164.41	156.02	-5.10	197.45	20.09

Based on the comparison of the time period between oscillations and the deviation in the head, it is concluded that Vardy & Brown's unsteady friction model is the best friction model for the use with DGCM in this case. This is because of a more accurate description of the time period between each oscillation. When looking at the head, it is too early in the flow time to conclude whether Vardy & Brown is better than Brunone, because they both have trouble accurately describing the damping of the head.

7.6. MOC SETTINGS - SUMMARY

In Table 7.17 the settings chosen in Sec. 7.3, 7.4, and 7.5 for Case 2, 3, and 4 respectively are summarized. These settings will be used in the simulations for comparison with the CFD simulations in Sec. 10.

Table 7.17: Chosen settings for DVCM and DGCM for each experiment.

Experiment	Two phase model	Friction model	m	ψ	Reaches
Soares et al.	DVCM	Vardy & Brown	5	0.55	48
	DGCM	Vardy & Brown	5	0.55	48
Bergant et al. Low velocity	DVCM	Vardy & Brown	5	0.55	48
	DGCM	Vardy & Brown	5	0.75	48
Bergant et al. High velocity	DGCM	Vardy & Brown	5	0.55	24

8. 1D TWO PHASE WATER HAMMER WITH BUBBLE DYNAMICS

The previously presented two phase water hammer models have neglected bubble dynamics. This section is used to get the theoretical basis for developing a 1D two phase water hammer model that includes bubble dynamics. First the governing equations for a two phase water hammer will be introduced then focus will turn to bubble dynamics.

8.1. GOVERNING EQUATIONS

It is assumed that the liquid is contaminated by a contaminant gas in small nuclei. It is assumed that the distribution is uniform, that there is no slip between the bubbles and the liquid, that no gas will be released to the liquid, the gravitational effects can be neglected, and that the mass of the bubbles can be neglected since $\rho_l \gg \rho_v$ [28].

With these assumptions, the continuity and momentum equations can be written as in Eq. (8.1) and Eq. (8.2).

$$\frac{\partial}{\partial t}((1 - \alpha)\rho_l A) + \frac{\partial}{\partial x}((1 - \alpha)\rho_l u A) = 0 \quad (8.1)$$

$$\frac{\partial}{\partial t}((1 - \alpha)\rho_l u A) + u \frac{\partial}{\partial x}((1 - \alpha)\rho_l u A) + A \frac{\partial P}{\partial x} + A J = 0 \quad (8.2)$$

Where u is the velocity, A is the cross sectional area of the pipe, and α is the void fraction of gas.

The void fraction is defined as in Eq. (8.3), as the volume of gas, V_g , compared to the total volume, V_{tot} [29].

$$\alpha = \frac{V_g}{V_{tot}} = \frac{n_0 \frac{4}{3} \pi R^3}{1 + n_0 \frac{4}{3} \pi R^3} \quad (8.3)$$

Where n_0 is the start concentration of vapour in steady state and R is the bubble radius. With Eq. (8.1) - (8.3), the only thing needed is a description of the bubble radius.

8.2. BUBBLE DYNAMICS

The bubble dynamics of a single bubble suspended in a liquid driven by a sinusoidal acoustic pressure is illustrated in Fig. 8.1.

Initially the bubble is in equilibrium with the radius R_0 at ambient pressure. As the pressure is dropped, the bubble will grow slowly at first then start to grow faster until the pressure gets closer to the initial pressure. The bubble growth will begin to slow down until it reaches the maximum radius. After the maximum radius has been reached, the bubble collapses until it reaches the minimum radius where it will rebound and increase in radius. During the collapse extreme bubble surface velocities are obtained. The reason for this rebound is that the gas and vapour is highly compressed. This behaviour of collapse and rebound will continue with decreasing amplitudes until it is at rest. [30] If the bubble is stable, and does not implode and split up into smaller bubbles, as was seen in Fig. 3.1, the Rayleigh-Plesset equation can be used to describe the bubble dynamics.

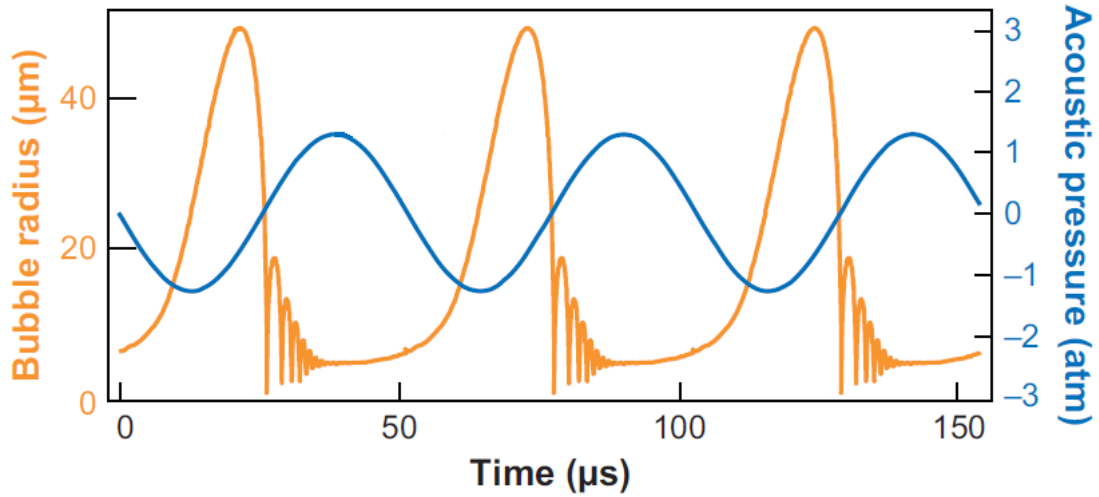


Figure 8.1: Bubble radius response for a sinusoidal acoustic pressure change. [30]

8.2.1. RAYLEIGH-PLESSET EQUATION

The Rayleigh-Plesset equation, Eq. (8.4), describes the dynamics of a single spherical bubble, that is the growth and the collapse, in an infinite liquid domain. It is derived from the Navier-Stokes equation and the full derivation is in App. A. It is assumed that the temperature of the liquid, the liquid density, and the dynamic viscosity of the liquid are constant. For the bubble it is assumed that the temperature is constant and that the internal bubble pressure, P_B , is uniform. [4]

$$\underbrace{\rho \left(R \frac{d^2 R}{dt^2} \right)}_{(1)} + \underbrace{\frac{3}{2} \left(\frac{dR}{dt} \right)^2}_{(2)} = \underbrace{P_B}_{(3)} - \underbrace{P_\infty}_{(4)} - \underbrace{\frac{2S}{R}}_{(5)} - \underbrace{\frac{4\mu}{R} \frac{dR}{dt}}_{(6)} \quad (8.4)$$

The first term (1) describes the pressure generated by the acceleration of the bubble wall, (2) comes from the convective terms in the Navier-Stokes equation, (3) is the internal bubble pressure, (4) is the pressure in the fluid far away from the bubble, (5) describes the surface tension of the bubble, and (6) is the viscous effect caused by the bubble growth. Since term (6) is the only viscous force present, it is assumed that the bubble follow the flow perfectly.

If it is assumed that P_∞ is known, a description of P_B is needed to solve Eq. (8.4) for the bubble radius. To describe the bubble pressure, the bubble contents will have to be assumed. It is assumed that a contaminant gas is present in the bubble with a partial pressure, P_{G0} , at a reference radius at steady state, R_0 , and temperature, T_∞ . Then the partial pressure of the gas at any given radius can be determined by Eq. (8.5), if the bubble temperature is constant and the gas behaviour is polytropic. [4]

$$P_G = P_{G0} \left(\frac{R_0}{R} \right)^3 \quad (8.5)$$

Then the bubble pressure can be determined with Eq. (8.6).

$$P_B = P_v + P_G \quad (8.6)$$

Where P_v is the vapour pressure. To solve Eq. (8.4) numerically it is split up into two first order ODEs, with $\frac{d^2R}{dt^2} = \frac{dy}{dt}$.

$$\frac{dR}{dt} = y \quad (8.7)$$

$$\frac{dy}{dt} = -\frac{3}{2R}y^2 + \frac{P_B - P_\infty}{\rho R} - \frac{2S}{\rho R^2} - \frac{4\mu}{\rho R^2}y \quad (8.8)$$

The initial conditions for the ODEs are $R(t=0) = R_0$ and $y(t=0) = \dot{R}_0$.

The last step is choosing a numerical solver. Alehossein et al. [31] investigated numerous solvers both with constant and variable time step for solving the Rayleigh-Plesset equation for cavitating water jets. They concluded that a variable time step is preferable, because at the bubble collapse and rebound, the slope is near $\pm\infty$. Therefore, very small time steps are needed to resolve the rebound. They also concluded that the Runge-Kutta-Feldberg (RKF) gave the most accurate solution. It has also been found in the literature that a Runge-Kutta based solver has been successfully applied to the Rayleigh-Plesset equation [32, 29].

8.2.2. RAYLEIGH-PLESSET RESPONSE

In the Rayleigh-Plesset equation it is the driving pressure P_∞ that causes the change in bubble radius. Therefore, the bubble response at different driving pressures is investigated. First with a small driving pressure also used by Alehossein et al. [31] with different solvers to test the implementation. Then with a driving pressure from case 2 with different initial bubble sizes.

8.2.3. SMALL DRIVING PRESSURE

Alehossein et al. [31] investigated the Rayleigh-Plesset equation for cavitating water jets. To test the numerical methods, they used a simplified version of the driving pressure, see Fig. 8.2. This simplified driving pressure is also used here to test if the Rayleigh-Plesset equation is correctly implemented and to test two numerical methods: Euler and the built in MATLAB "ode45" Runge-Kutta solver.

In the Euler method, a constant time step of $2 \cdot 10^{-10}$ s was used as further reductions of the time step had no effect on the bubble dynamics. The Runge-Kutta solver used a variable time step that is dependent on the bubble boundary speed. The fluid properties and initial bubble size used for the simulation are listed in Table 8.1.

The results of the simulation are in Fig. 8.2. The Euler and Runge-Kutta solvers give similar results predicting the initial growth phase and the first collapse and rebound. But after the first rebound, an offset between the two solvers occurs. This small offset starts to occur when the rate of change of the bubble radius begins to decrease which is where the step size should increase for the Runge-Kutta solver. Therefore, the offset

Symbol	Value
$P_\infty(0)$	$12000Pa$
P_v	$4240Pa$
ρ_l	$996 \frac{kg}{m^3}$
ν_l	$0.798 \cdot 10^{-3} \frac{m^2}{s}$
S	$7.2 \cdot 10^{-2} \frac{N}{m}$
R_0	$10^{-5}m$

Table 8.1: Fluid properties and initial bubble size.

is likely to be caused by this effect. The Runge-Kutta uses significantly less time steps with 177 time steps compared to 185001 timesteps used by the Euler solver. Therefore the built-in MATLAB "ode45" solver will be used [33]. The results obtained here give a smaller bubble growth than the one obtained by Alehossein et al. [31], which might be caused by a different calculation method of P_{g0} , which was not given in the article.

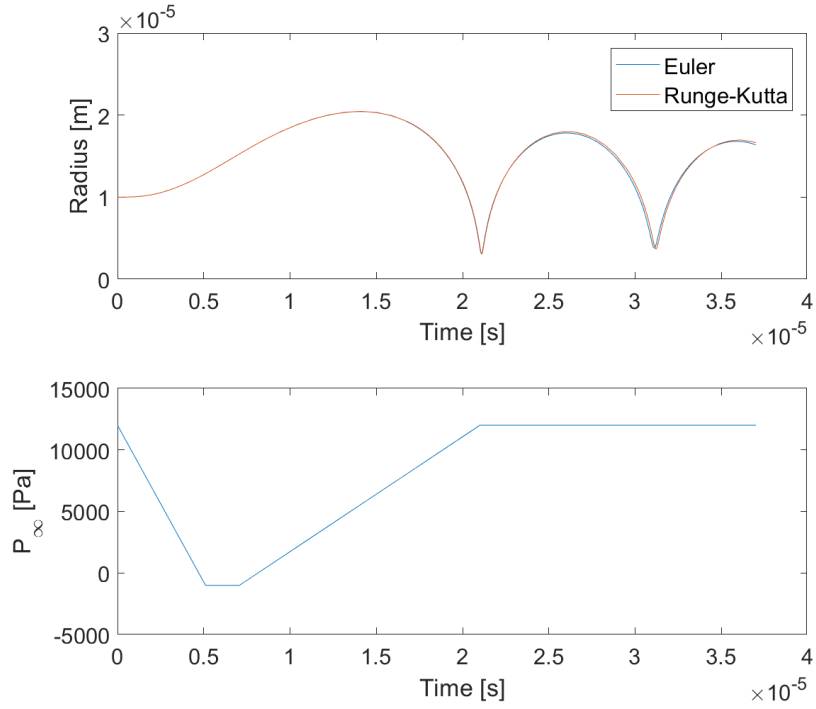


Figure 8.2: Bubble radius and driving pressure.

8.2.4. BUBBLE RESPONSE TO WATER HAMMER PRESSURES

Compared to the pressure changes in Sec. 8.2.3, the actual pressure changes in a water hammer event is usually both steeper and larger. Therefore it will be more difficult to resolve the collapse and rebound of the bubble. The response with three different initial bubble sizes are also tested.

In Fig. 8.3 the driving pressure during case 2 is illustrated.

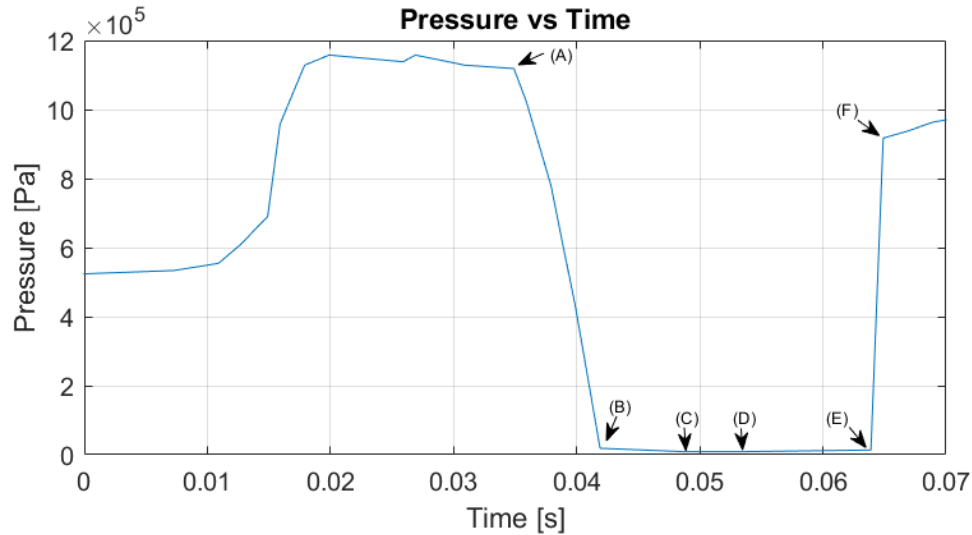


Figure 8.3: Driving pressure during water hammer event.

Where point (A) is the end of the first high pressure zone, from point (A) to (B) is the change from the high pressure zone to the low pressure zone, from point (B) to (C) there is a small decline in pressure until it reaches the vapour pressure in (C), from (C) to (D) the pressure is at the vapour pressure, from point (D) to (E) there is a slight increase in pressure, and from point (E) to (F) it changes from the low pressure zone to the second high pressure zone. The pressure data was extracted with the program ScanIt and linear interpolation between the points is used when solving the Rayleigh-Plesset equation.

In Fig. 8.4, the response of three bubbles, using different initial radii, can be seen for the driving pressure in Fig. 8.3.

From time equals to zero until point (A), all three bubbles have the same behaviour i.e. initially staying at R_0 followed by a compression of the radius caused by an increase in pressure. Also from point (A) to (B), i.e. the period where the pressure changes from the high pressure zone to low pressure zone, the behaviour is similar with an increase in radius resembling an exponential increase. Then from point (B) to (C) the behaviour of the three bubbles begin to differ, but still exhibiting the same tendency. The bubble with the initial radius of $10^{-5}m$ starts to oscillate directly after point (B), but the oscillations are damped quickly and thereafter the bubble starts to grow exponentially until point (C). The bubbles with initial radii of $5 \cdot 10^{-5}m$ and $10^{-4}m$ start to oscillate directly after point (B) as with the smallest bubble, but with larger and slower oscillations.

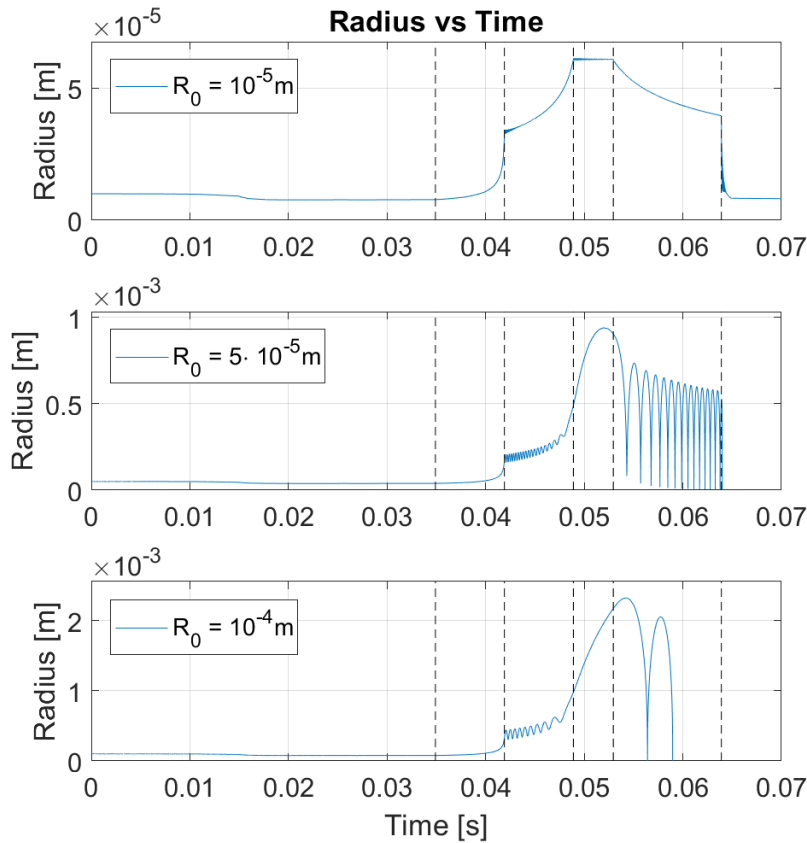


Figure 8.4: Bubble response with different initial bubble radius. The dashed lines indicate positions (A) to (E).

After the oscillations both bubbles start to grow, but now the characteristics of the growth is not of an exponential growth. From point (C) to (D) the smallest bubble seems to quickly reach an equilibrium state since there is no change in radius. The two larger bubbles do not reach an equilibrium. Instead they both grow initially and for the bubble with an initial radius of $5 \cdot 10^{-5}m$ starts to decrease again before point (D). Since the pressure is constant at the vapour pressure an explanation of this could be due to it overshooting the radius that would bring it into equilibrium. From point (D) to (E) the smallest bubble experiences a decrease in radius due to an increase in pressure. The two largest bubbles both collapse and rebound. The collapse experienced by the bubble with an initial radius of $10^{-4}m$ is so violent that the "ode45" solver fails. After point (F) the smallest bubble collapses and reaches a new equilibrium state while the bubble with the initial radius of $5 \cdot 10^{-5}m$ collapses so violent that the solver fails.

There are three possible conclusions that can be made. It seems that the larger the bubble the slower it will respond to the pressure or that the oscillations of the bubble

becomes larger and slower. The reverse is true for smaller bubbles which should respond quickly to the pressure causing only small oscillations. The second is that during water hammers it seems that it is possible for the bubbles to reach an equilibrium state even if the pressure is equal to the vapour pressure. This is a consequence of the assumption that the mass transfer across the bubble interface can be neglected. It also seems that the larger the bubble the more violent the collapse. These violent collapses caused the "ode45" solver to fail because integration tolerances could not be met without lowering the timestep below the minimum allowed value of $1.11 \cdot 10^{-6}$.

The radius that causes the bubble to be in equilibrium at the vapour pressure can be determined by combining Eq. (8.4) to Eq. (8.6), and setting $dR/dt = d^2R/dt^2 = 0$ and $P_\infty = P_v$ and solving for R .

$$R = \left(\frac{2S}{P_{G0}R_0^3} \right)^{-\frac{1}{2}} \quad (8.9)$$

To test whether the bubbles do indeed reach an equilibrium point the pressure will be kept at the vapour pressure from point (B) and onwards. The results are plotted in Fig. 8.5.

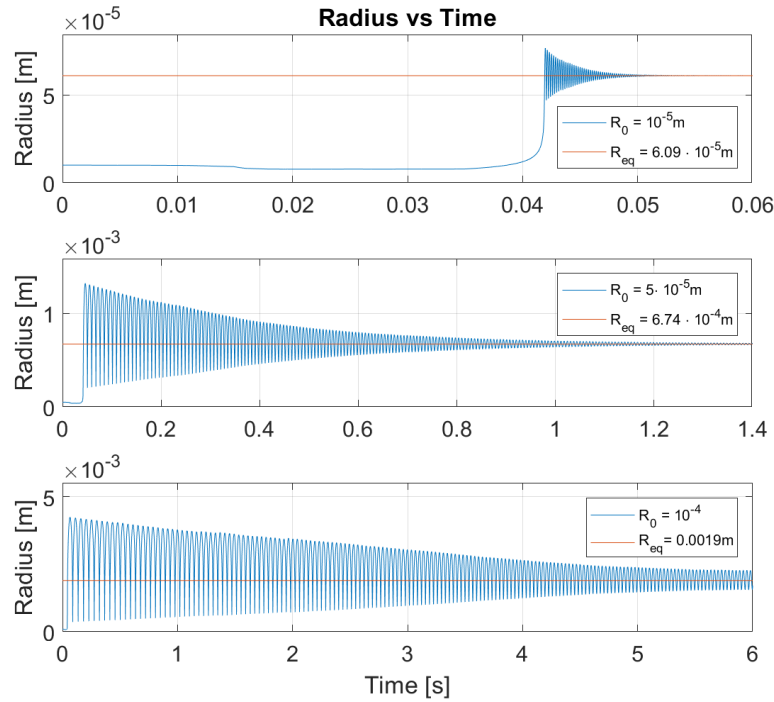


Figure 8.5: Bubble response with different initial bubble radius and equilibrium radius at vapour pressure.

From this it is clear that the bubbles actually respond to the change to the vapour pressure, but that they oscillate around the radius that causes them to be in equilibrium.

It can also be seen that the larger the initial bubble radius is, the longer the oscillation will be present. This is a problem since the bubble would not grow even though the fluid is at the vapour pressure. As explained before this is caused by the assumption that there is no mass transfer through the bubble interface. This assumption is only valid if the bubble is only a short time in the vapour pressure region. Which is not necessarily the case during a water hammer event. Therefore, for application to water hammer events, the mass transfer through the interface should be modelled. For the implementation of the Rayleigh-Plesset equation another solver than the "ode45" should be used during a water hammer event since the collapse of the bubble is too violent. Other solvers such as the stiff solvers "ode23s" and "ode15s" were also used, but they yielded similar results and also failed to solve the Rayleigh-Plesset equation. The used solver should be a solver that can handle the discontinuity during the collapse and rebound.

8.3. IMPLEMENTATION

If the problems with the Rayleigh-Plesset equation are solved the next step would be to implement it into the governing equations, Eq. (8.1) and Eq. (8.2), via the void fraction.

Kalwijk et al. [28] implemented Eq. (8.1) and Eq. (8.2) into the MOC without the Rayleigh-Plesset equation governing the void fraction. They found that for low pressure, i.e. at vapour pressure, that the governing equations turned from hyperbolic to elliptic which is not physical. This might be a problem as well with the implementation of the Rayleigh-Plesset equation.

Another problem, if the Rayleigh-Plesset equation is implemented, is that at the collapse and rebound, extremely small time steps are needed to resolve the bubble growth. This time step is very small compared to the time step normally needed to calculate a water hammer event with the MOC. This decrease in the time step would also increase the number of reaches in the MOC since dt and dx is related by Eq. (5.18) and thereby increase the calculation time significantly. To decrease the calculation time, a variable time step could be used, but it would cause the characteristics grid to resemble the variable grid in Fig. 7.1 which introduces other problems.

It seems therefore that the implementation is not straight forward in the explicit MOC and perhaps other methods should be considered.

9. CFD MODELLING OF TWO PHASE FLOW

In this section, the CFD theory for two phase simulations with the choice in multiphase and cavitation model is presented, and CFD simulations are performed for Case 2, 3 and 4.

9.1. MULTIPHASE MODEL

To model the multiphase flow ANSYS Fluent 19.0 has three different models available; Volume of Fluid (VOF), the Mixture model and the Eulerian model. All three models uses the Euler-Euler approach but only the mixture and Eulerian model is available with the cavitation models. With the Eulerian model only the k- ϵ turbulence models is available. If the Mixture model is chosen, both the k- ϵ and the k- ω turbulence models is available. The Mixture model is less computational heavy as it has less equations to solve compared to the Eulerian model which also can be less computationally stable because it is more complex [23].

The Mixture model solves the mixture momentum equation to calculate the relative velocities of the dispersed phases, but can also be used without relative velocities.

The Mixture model can model an infinite number of fluids by solving the continuity, momentum, and energy equation of the mixture and the void fraction for the secondary phase. The limitations of the Mixture model is that only a pressure-based solver is available, only one phase can be defined as compressible, and a specified mass flow rate boundary condition is not possible.

For a multiphase flow the continuity, momentum equation and the transport equations for the turbulence models has been changed such that the mass averaged velocity, the density and viscosity is based on a mixture of the phases. The mass averaged velocity can be calculated with Eq. (9.1).

$$\vec{v}_m = \frac{1}{\rho_m} \sum_{k=1}^n \alpha_k \rho_k \vec{v}_k \quad (9.1)$$

Where α_k is the void fraction of phase k. The mixture density is calculated with Eq. (9.2).

$$\rho_m = \sum_{k=1}^n \alpha_k \rho_k \quad (9.2)$$

The mixture viscosity is calculated with Eq. (9.3).

$$\mu_m = \sum_{k=1}^n \alpha_k \mu_k \quad (9.3)$$

The compressible Navier-Stokes momentum equation for the mixture can be obtained by summing the individual momentum equation for each phase.

9.2. CAVITATION MODEL

ANSYS Fluent 19.0 have three available cavitation models: The Schnerr and Sauer [34], the Zwart-Berber-Belamri, and the Singhal et al. model. The two first models converge quickly and are robust where Singhal et al. is numerically less stable. The Schnerr and Sauer and the Zwart-Berber-Belamri models have the same options for the simulations, but as the Schnerr and Sauer model has shown to give good results in other studies [35, 36, 37]. Therefore the Schnerr and Sauer model is chosen to determine the mass transfer between the liquid and vapour phases. The model is based on a simplified Rayleigh-Plesset equation for the effect of bubble dynamics. The bubble growth is described as in Eq. (9.4) [34] and it is a simplified form of the Rayleigh-Plesset equation from Eq. (8.4) in Sec. 8.2.1.

$$\frac{dR}{dt} = \sqrt{\frac{2}{3} \frac{P(R) - P_\infty}{\rho_l}} \quad (9.4)$$

Where $P(R)$ is the pressure at the bubble boundary in the liquid (set to the vapour pressure), P_∞ is the pressure in the liquid far from the bubble and ρ_l is the liquid density. The net mass transfer rate for the vapour void fraction, M_v , is calculated with Eq. (9.5).

$$\frac{\partial}{\partial t}(\alpha \rho_v) + \frac{\partial}{\partial x_j}(\alpha \rho_v \vec{u}_v) = M_v \quad (9.5)$$

Where α is the nucleation site void fraction, \vec{u}_v is the vapour phase velocity (which is equal to the liquid phase velocity when there is no slip velocity).

The Schnerr og Sauer connects the void fraction to the number of bubbles per volume of liquid to determine the nucleation site void fraction with Eq. (9.6).

$$\alpha = \frac{n_b \frac{4}{3} \pi R_B^3}{1 + n_b \frac{4}{3} \pi R_B^3} \quad (9.6)$$

Where n_b is the bubble number density and R_B is the bubble radius.

In this model, the only parameter which has to be user defined is the number of spherical bubbles and the vaporization pressure. Schnerr and Sauer determines both the mass transfer for the evaporation and for the condensation, where, if no bubbles are created or destroyed, the bubble density will be constant. Mass transfer for the evaporation, M_e , and condensation, M_c , can be seen in Eq. (9.7) and (9.8) respectively.

$$M_e = \frac{\rho_v \rho_l}{\rho_m} \alpha (1 - \alpha) \frac{3}{R_B} \sqrt{\frac{2}{3} \frac{(P_v - P_\infty)}{\rho_l}} \quad (9.7)$$

$$M_c = \frac{\rho_v \rho_l}{\rho_m} \alpha (1 - \alpha) \frac{3}{R_B} \sqrt{\frac{2}{3} \frac{(P_\infty - P_v)}{\rho_l}} \quad (9.8)$$

Where ρ_v , ρ_l and ρ_m is respectively the density for the vapour, liquid and the mixture, P_v is the vapour pressure and P_∞ is the far-field pressure.

The bubble radius can be determined with Eq. (9.9).

$$R_B = \left(\frac{\alpha}{1 - \alpha} \frac{3}{4\pi} \frac{1}{n_b} \right)^{\frac{1}{3}} \quad (9.9)$$

The limitation of using the cavitation models in ANSYS Fluent 19.0, is that, it is only possible to simulate a single cavitation process (single liquid undergoes cavitation). Which means that it is not possible to model cavitation in a multi-component flow. Also Schnerr and Sauer does not by default take the effect of non-condensable gases into account. [23]

9.3. CFD SIMULATION OF SOARES ET AL. EXPERIMENT

A two phase CFD simulation is performed on Case 2. In this section, the fluent settings are described and a grid independency analysis and a turbulence model test have been performed.

9.3.1. ASSUMPTIONS

The geometry is drawn as 2D axisymmetric to simulate the pipe flow. The bulk modulus of the water has been calculated such that it incorporate the effect of the pipe elasticity as described in Sec. 6.4.5.

9.3.2. BOUNDARY CONDITIONS

The boundary conditions chosen is a "velocity-inlet" with a reversed velocity as described in Sec. 6.4.3 and a "pressure-outlet". The "velocity-outlet" and "mass flow-outlet" is not available in the Mixture model but, the "velocity-inlet" is, as described in Sec. 9.1. A UDF is used for the "velocity-inlet" to control the valve closure as in Sec. 6.4.4. The UDF can be seen in App. B.

9.3.3. PRESSURE VELOCITY COUPLING SCHEME

The pressure based coupled algorithm is chosen for solving the system of equations. The coupled solver has an improved convergence rate compared to the segregated solvers [23].

9.3.4. TIME STEP SIZE

To ensure that the pressure wave is calculated through each cell at each time step, a proper time step size has to be determined. The time step size is chosen based on a Courant number of 1 calculated with Eq. (5.19).

9.3.5. CONVERGENCE ANALYSIS

To analyse if the solution has converged, the residuals were monitored. An absolute convergence criteria was set to 10^{-5} and the maximum number of iterations were limited

to 200 per time step. When the vapour pressure was reached all iterations were used as the solution of the continuity equation solution would not meet the convergence criteria. After about 20-40 iterations the solution would not improve and the residual would be around 10^{-3} as seen in Fig. 9.1.

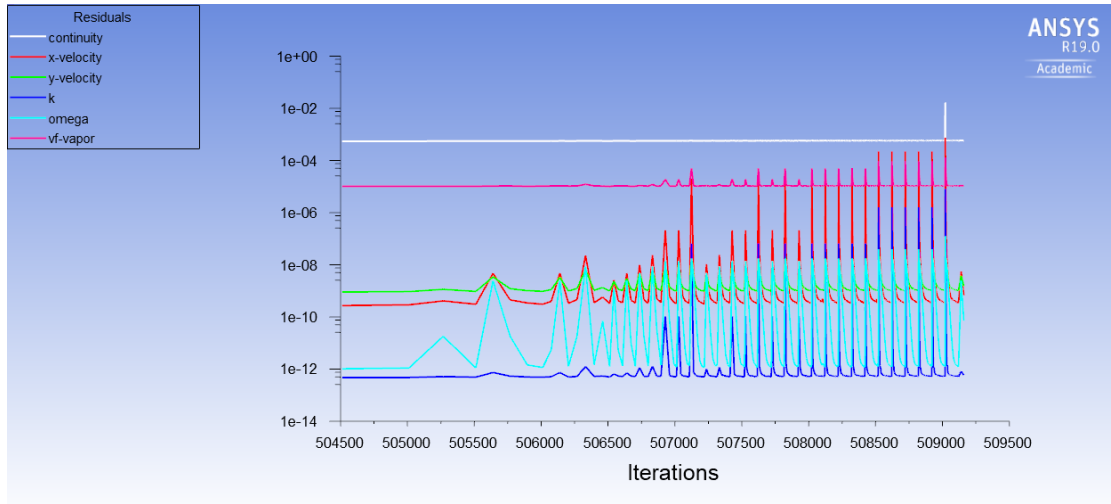


Figure 9.1: Residuals for cavitation flow.

As it can be seen the problem was only detected with the continuity equation. When the flow was not cavitating, the convergence criteria was obtained and the solution used between 20-40 iterations, the residuals can be seen in Fig. 9.2.

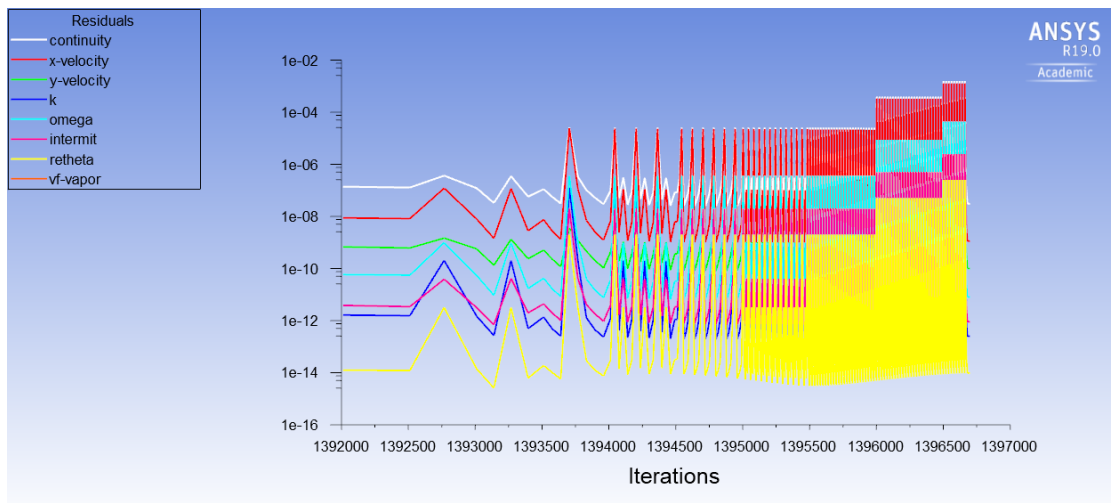


Figure 9.2: Residuals for high pressure non-cavitation flow.

9.3.6. FLUENT SETTING OVERVIEW

An overview of the chosen parameters for the CFD simulations in ANSYS Fluent are listed in Table 9.1.

Table 9.1: Fluent settings.

Settings	Parameters
Solver type	Pressure-based
Velocity formulation	Absolute
Time	Transient
2D Space	Axissymmetric
Multiphase model	Mixture model
Cavitation model	Schnerr and Sauer
Fluid	Water-liquid
Vapour	Water-vapour
Inlet boundary	Velocity-inlet
Outlet boundary	Pressure-outlet
Wall boundary	Wall
Shear Condition	No Slip
Wall roughness	$1.5 \cdot 10^{-6}m$
Pressure velocity coupling	Coupled
Discretisation	QUICK
Absolute convergence criteria	$1 \cdot 10^{-5}$
Solution initialization	Hybrid initialization
Time step size	$5.9690 \cdot 10^{-6}s$
Number of time steps	41884
Max Iterations/Time step	200

9.3.7. GRID INDEPENDENCY STUDY

The grid is generated with an inflation as in Sec. 6.4.1. To analyze if the pressure wave is properly resolved, a grid independency study has been carried out. The purpose of the study is to determine if the result of a more coarse mesh is sufficient compared to a finer grid. To determine if there is a change in the grid results, the pressure at the valve is measured. As the pressure is almost equal at all nodes on the valve boundary, an average is taken over all the nodes. The chosen cell numbers for the different meshes are listed in Table 9.2.

Table 9.2: Different grid cell numbers.

Number of cells	Mesh size	$y+$ at steady state	Time step size
3.000	$6 \cdot 500$	15.5 – 19.5	$2.3876 \cdot 10^{-5} s$
12.000	$12 \cdot 1000$	3 – 6.7	$1.1938 \cdot 10^{-5} s$
48.000	$24 \cdot 2000$	0.3 – 2	$5.9690 \cdot 10^{-6} s$
192.000	$48 \cdot 4000$	0.02 – 0.6	$2.9845 \cdot 10^{-6} s$

The grid with respectively 48000 and 192000 cells have a $y+$ value below 5 (in the viscous sublayer) where the grids with 3000 and 12000 cells is chosen to also analyze how large dependence the $y+$ value has on the mean pressure at the valve. The time step size is different for each mesh to ensure all models have a Courant number of 1 (calculated as in Sec. 9.3.4).

The result for the grid independency study is as seen in Fig. 9.3.

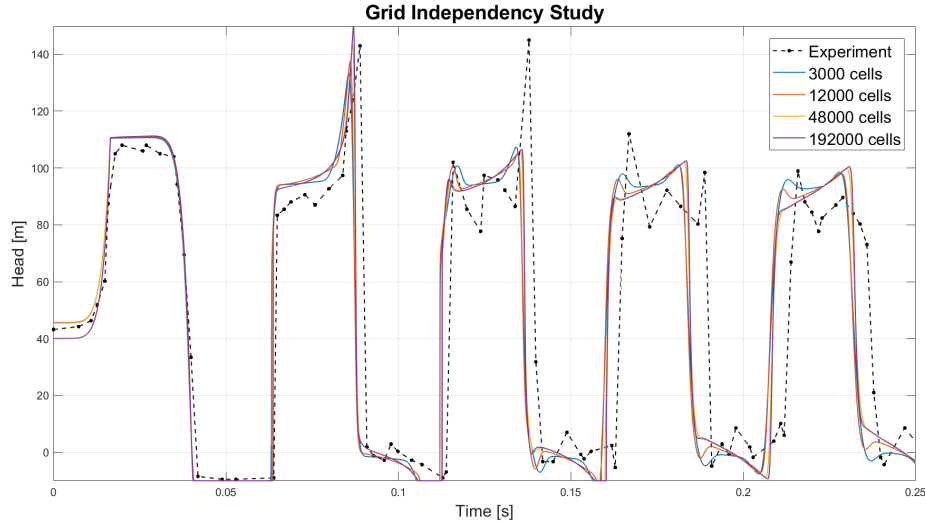


Figure 9.3: Grid independency test.

At the first high pressure zone and low pressure zone, all mesh sizes produce identical results. At the second high pressure zone, the mesh with 3000 and 12000 cells underestimate the pressure where the mesh with 48000 cells gives a good representation of the pressure and the mesh with 192000 cells overestimate the pressure.

At the third high pressure zone, the mesh with 3000 and 12000 cells have an accurate description of the first peak, while the mesh with 48000 and 192000 cells underestimate the pressure. For the second peak on the third high pressure zone, all of the mesh sizes give similar results, but they all seriously underestimate the pressure. This problem was also observed for MOC, with the experiment having its largest peak at the third high

pressure zone, while the simulations have their highest peak at the second high pressure zone. When comparing the largest peaks, it can be seen that the mesh with 48000 cells slightly underestimate the pressure while the mesh with 192000 cells slightly overestimates the pressure. Despite missing the peak behaviour from the third high pressure zone, the mesh with 48000 cells is chosen as it gives the best results for the second high pressure zone and seem to have converged with the larger model of 192000 cells every where else.

9.3.8. TURBULENCE MODELS TEST

A turbulence model test is performed to analyse if the choice in turbulence model has an effect on the result. Three turbulence models are tested: Realizable $k - \epsilon$, Standard $k - \omega$ and SST $k - \omega$ (which are described in Sec. 6.3).

A wall function was only used with the Realizable $k - \epsilon$ model as the other models resolve the flow at the wall. The enhanced wall treatment was used as it does not rely on empirical relations and the criteria of $y^+ \approx 1$ is satisfied [23].

As for the grid test, the pressure is analysed as an average for all notes at the valve. The comparison of the turbulence models can be seen in Fig. 9.4.

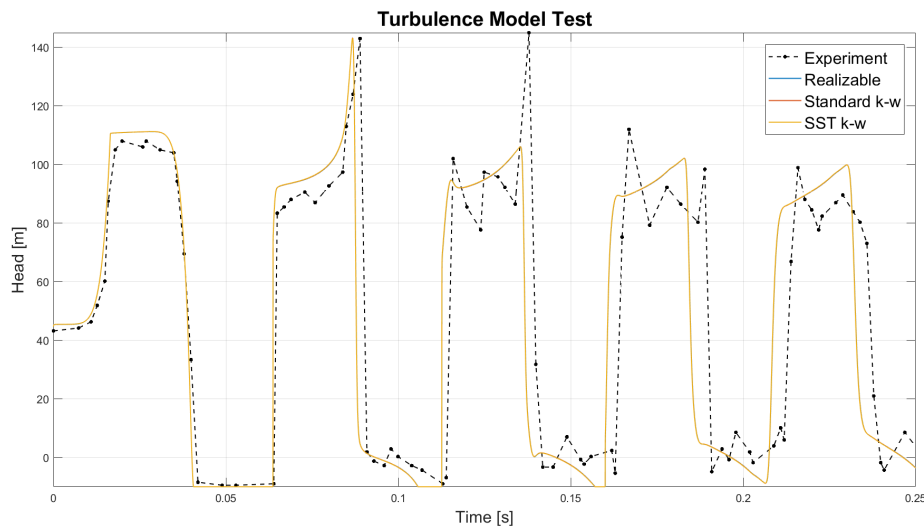


Figure 9.4: Turbulence models test.

It is only possible to see the SST $k - \omega$ model as all models give similar results. Theoretically following Sec. 6.3.3, the SST $k - \omega$ model should give the best results and as the simulation is independent of the turbulence model used, the SST $k - \omega$ model is used for further calculation.

9.4. CFD SIMULATION OF BERGANT ET AL. EXPERIMENTS

For the simulation of the Bergant et al. experiments (Case 3 and 4), the same assumptions for the, boundary conditions, pressure velocity coupling scheme, and fluent settings were used.

The time step size was calculated based on a Courant number of 1, as with the Soares et al. experiment (Case 2). It was not possible to obtain proper CFD simulation results for Case 3 and 4 even though a variety of methods were carried out for better results.

CONVERGENCE

The problem with the Bergant et al. simulations are the fact that when the pressure wave reaches the vapour pressure, the residuals for the continuity is too high (as seen in Fig. 9.5). The convergence criteria is set to 10^{-5} .

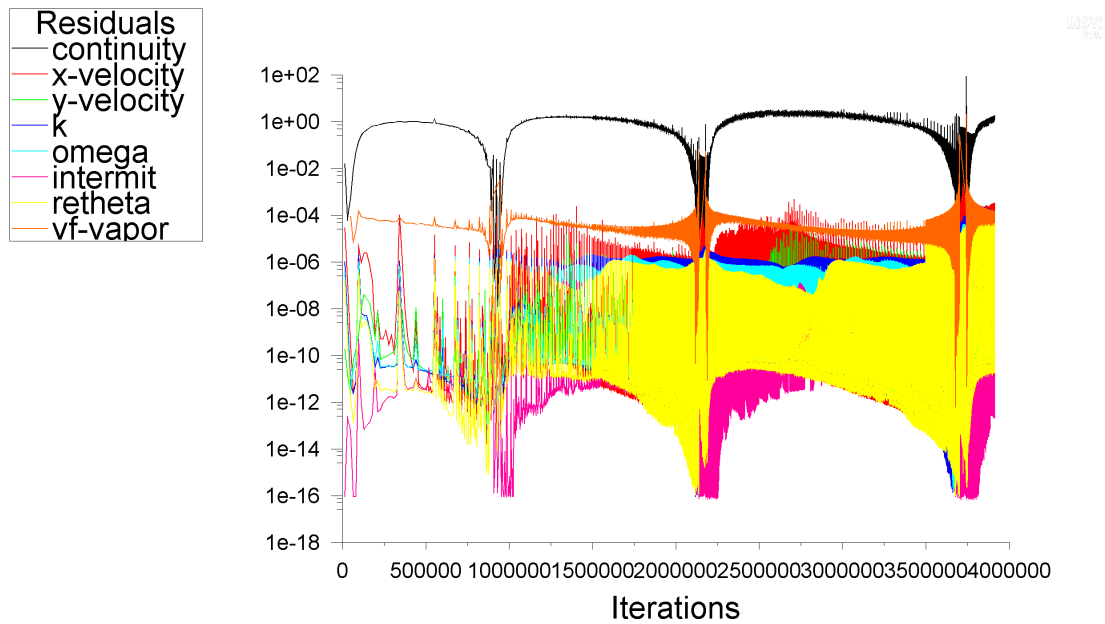


Figure 9.5: Residuals for the Bergant experiment with high velocity and 6000 cells.

On Fig. 9.5 the residuals uphold the convergence criteria for the high pressure zones, but for the cavitation zones the residuals of the continuity equation are almost equal to 1.

MESH

To achieve more precise residuals the mesh was refined and the time step size was decreased correspondingly. The refinement did not improve the residuals.

PRESSURE VELOCITY COUPLING SCHEME

The PISO solver was tried as this should also be a precise solver for transient flow [23], but this only made the residuals for continuity and void fraction of the vapour higher.

UNDER-RELAXTION FACTORS

Decreasing the under-relaxation factors for the void fraction and the vaporization mass made the residuals more stable and the calculation time slower but did not increase the accuracy of the residuals.

CAVITATION MODELS

To analyse if the cavitation model had an effect on the residuals, the Zwart-Berber-Belamri model was tried. The shift in cavitation model only increased the residuals of the continuity equation to around 10.

TIME STEP SIZE

The time step size used for a Courant number of 1 does not seem to be low enough even though, the tested meshes had a time step size of between $2 \cdot 10^{-5}s$ - $10^{-6}s$. Various CFD-forums suggest a time step size as low as $10^{-7}s$ - $10^{-8}s$ for cavitation simulations. A simulation was run with a time step size of $5 \cdot 10^{-8}s$ but unfortunately the computer (Windows 10) chose to update after 5 days of simulation without reaching the cavitation zone. Because of time constraints it has not been possible to do another simulation with a time step size that low.

BERGANT ET AL. SIMULATION RESULTS

It was seen that the Soares et al. two phase simulation with a grid of $6 \cdot 500$ cells gave relatively good results. To decrease the simulation time and as the Bergant et al. pipe is almost twice as long, a mesh with $6 \cdot 1000$ cells was used. With a Courant number of 1, the time step size is $2.8067 \cdot 10^{-5}s$. The results of the Bergant et al. simulations with low and high velocity can be seen in Fig. 9.6 (Case 3) and 9.7 (Case 4).

In Fig 9.6 it can be seen that the CFD model accurately describe the first pressure peak. In the first low pressure zone it can be seen that the vapour pressure of the model is smaller than the one in the experiment and the time in the low pressure zone is also slightly longer. The second pressure peak is overestimated by the CFD model and a slight offset in time. It is suspected that these two effects can be attributed to the additional time in the first low pressure zone. In the second low pressure zone, the CFD model has a behaviour reminiscent of the experimental data, but it greatly overestimates the time in the zone. This again causes the an overestimation of the pressure and an offset of the pressure peak compared to the experimental data.

Again it can be seen from Fig. 9.7 that the CFD model accurately describe the first pressure peak. It is also clear that the CFD model overestimates the time in the low

pressure zone, which causes, in this case, a large overestimation of the pressure. It can be seen that the model has a behaviour opposite of the experimental results. In the experimental data it is clear that the pressure reduces for each pressure peak followed by a decrease of the time in the low pressure zone at vapour pressure. This is caused by friction in the pipe. In the CFD model the pressure increases for each pressure peak followed by an increase of the time in the low pressure zone. This is clearly incorrect as the energy should dissipate through friction. These problems are for both Case 3 and 4 attributed to the large residuals in the cavitation zone.

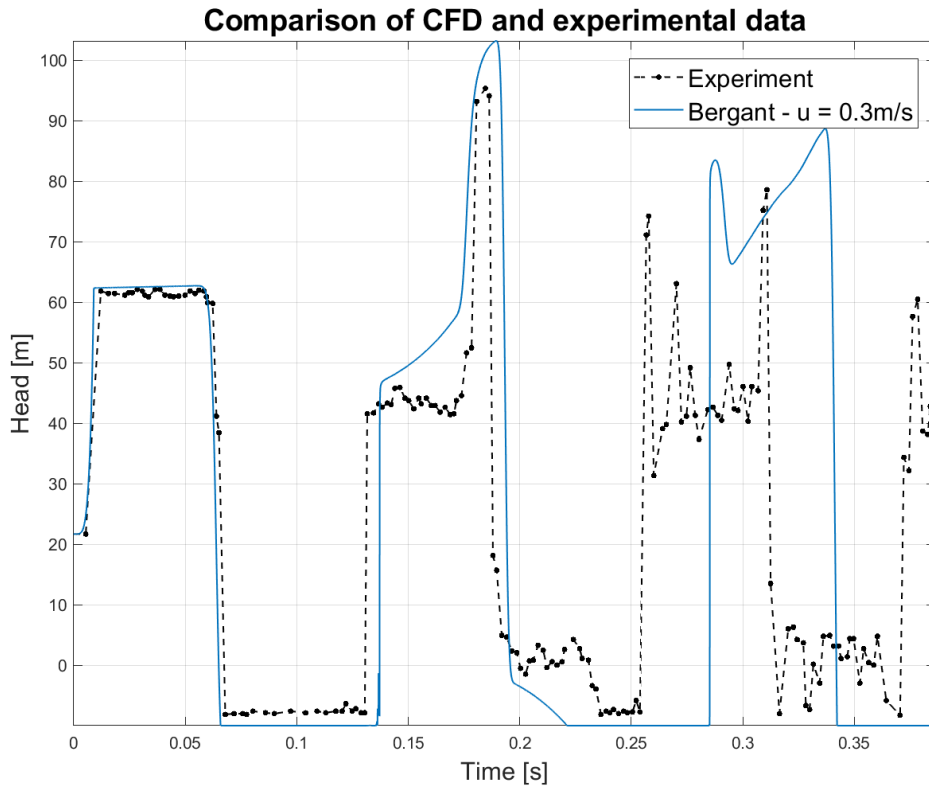


Figure 9.6: Bergant experiment with $u = 0.3\text{m/s}$ and 6000 cells.

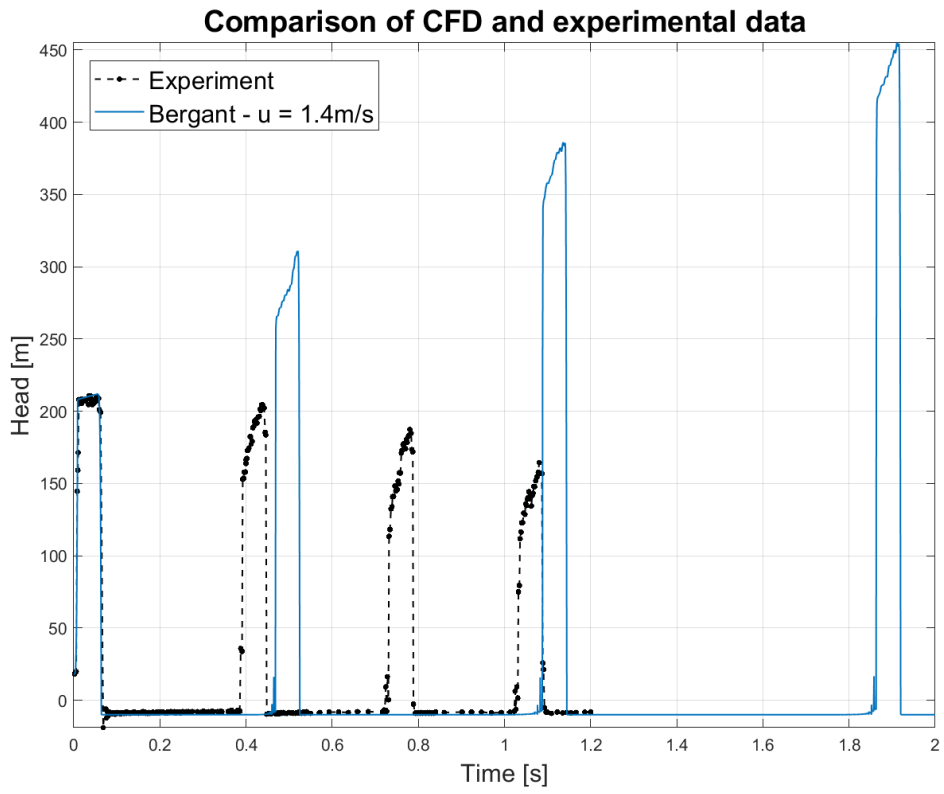


Figure 9.7: Bergant experiment with $u= 1.4m/s$ and 6000 cells.

10. RESULTS

The results for Case 2, 3 and 4 are presented in this section.

10.1. SOARES ET AL. EXPERIMENT

The simulations of Case 2 can be seen in Fig. 10.1. DVCM, DGCM, and CFD simulations are compared to the experimental data for a flow time of 0.5s.

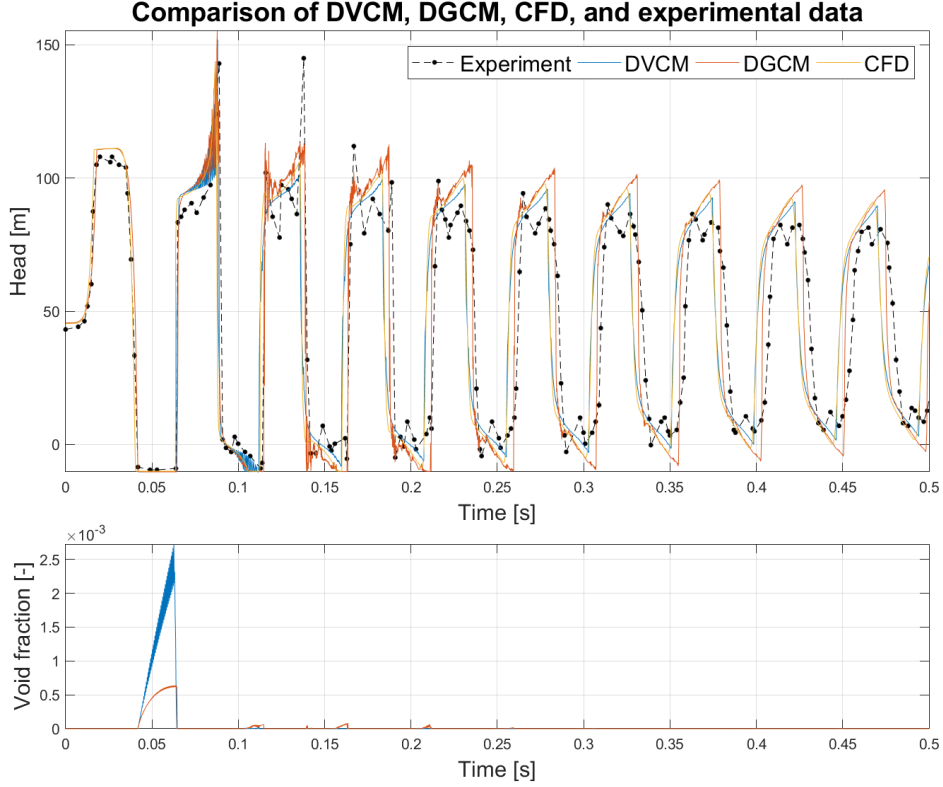


Figure 10.1: Comparison of head and void fraction for DVCM, DGCM, CFD, and the experimental data.

The comparison of the simulations has been performed in the same manner as in Sec. 7.3.2. The highest peaks of the high pressure zones for DVCM, DGCM, and CFD simulation have been determined and the size of the peaks are compared to the experiment as seen in Fig. 10.2. The size of the peaks and the deviation from the experiment can also be seen in Table 10.1. To analyse if the simulations have phase shifts, the time between the high pressure peaks are summarized in Table 10.2.

Comparing the high pressure peaks with Fig. 10.2 and Table 10.1 it can be seen that the pressure for all of the simulations are almost equal for the first pressure peak with a deviation of +3% from the experiment. A part of this deviation can be because of a

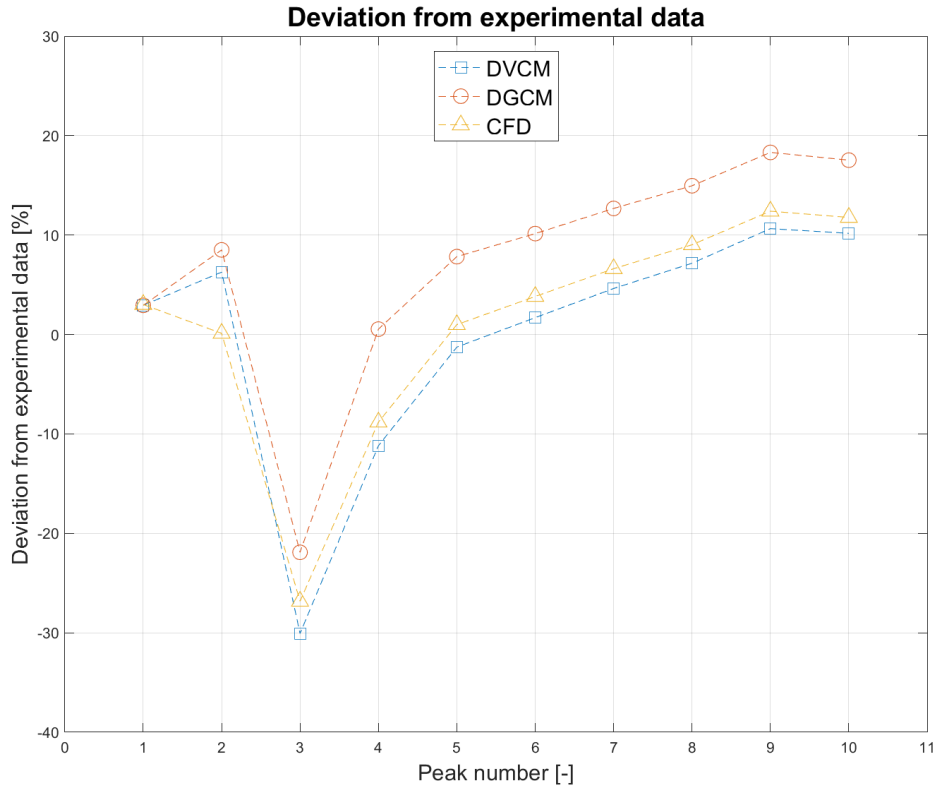


Figure 10.2: Deviation from the experimental data.

Table 10.1: Difference in head at peaks.

Peak	Experiment	DVCM		DGCM		CFD	
	Head [m]	Head [m]	Deviation [%]	Head [m]	Deviation [%]	Head [m]	Deviation [%]
1	108.00	111.17	2.93	111.16	2.93	111.25	3.01
2	143.00	151.98	6.28	155.16	8.51	143.16	0.11
3	145.00	101.40	-30.07	113.23	-21.91	106.10	-26.83
4	112.00	99.48	-11.18	112.61	0.54	102.13	-8.81
5	98.90	97.65	-1.27	106.64	7.83	99.88	0.99
6	94.30	95.90	1.69	103.87	10.14	97.91	3.82
7	90.10	94.27	4.63	101.52	12.67	96.06	6.62
8	86.50	92.70	7.17	99.44	14.96	94.30	9.02
9	82.40	91.17	10.65	97.49	18.31	92.62	12.40
10	81.40	89.68	10.17	95.67	17.53	90.98	11.77

higher pressure at steady state, as it can be seen in Fig. 10.1 that the head at time zero is higher for the simulations than for the experiment. For the second peak, the CFD

simulation reaches almost precisely the head of the experiment with only a deviation of +0.11% where DVCM and DGCM overestimate the head with +6.28% and +8.51% respectively. For the third peak, it can be seen that none of the simulations can accurately describe the peak. The reason for this is, as explained in Sec. 7.3.2, that for the experiment, the third peak is the largest, while for the simulations, the second peak is the largest. However, when looking at Fig. 10.1, it can be seen that for DVCM and DGCM, their second peak is higher than the third peak for the experiment, which means these models are actually able to predict the largest pressure (overestimation at +4.8% and +7% respectively). However, CFD is not able to predict the largest pressure peak and has an underestimation of -1.3% of the largest peak.

As the pressure wave propagates, the DVCM and CFD simulations follow the experimental results with a small overestimation, whereas the deviation from the experiment to the DGCM simulation is almost twice as high as the deviation for the DVCM simulation.

It can be seen in Fig. 10.1 that the vapour void fraction for the DGCM simulation is much lower than for the DVCM simulation. This behaviour of the DGCM simulation was described in Sec. 7.3.1 where it was a general observation for the Vardy % Brown friction model. The void fraction for the CFD simulation is not plotted, as in the exported data, the void fraction was only given for two of the 25 nodes at the boundary valve.

Table 10.2: Time of period of oscillation.

Friction models	Largest	Average	Smallest
Experiment [s]	0.0690	0.0494	0.0290
DVCM [s]	0.0602	0.0491	0.0475
DGCM [s]	0.0599	0.0496	0.0465
CFD [s]	0.0581	0.0488	0.0472

Comparing the phase shift for the simulations, it can be seen from Fig. 10.1 and Table 10.2 that the DGCM simulation follows the average time period of the experiment most precisely, whereas when analysing Fig. 10.1 DVCM and CFD simulations are almost identical. The time between the high pressure peaks are almost identical for the simulations as seen in Table 10.2 but as it can be seen in Fig. 10.1 the DGCM simulation has the smallest phase shift from the experiment.

The overall most accurate simulation is chosen, from an engineering point of view, as the DVCM simulation. The DVCM simulation overestimates the second high pressure peak more than the CFD simulation, but as the third pressure peak is higher than the second for the experiment and the CFD simulation is below that, the DVCM simulation is chosen as the best representation for this experiment. The DVCM simulation has a reminiscent behaviour of the wave and the phase shift.

10.2. BERGANT ET AL. LOW VELOCITY EXPERIMENT

The simulations of Case 3 can be seen in Fig. 10.3. Only DVCM and DGCM simulations is compared as the CFD simulation did not converge properly as described in Sec. 9.4.

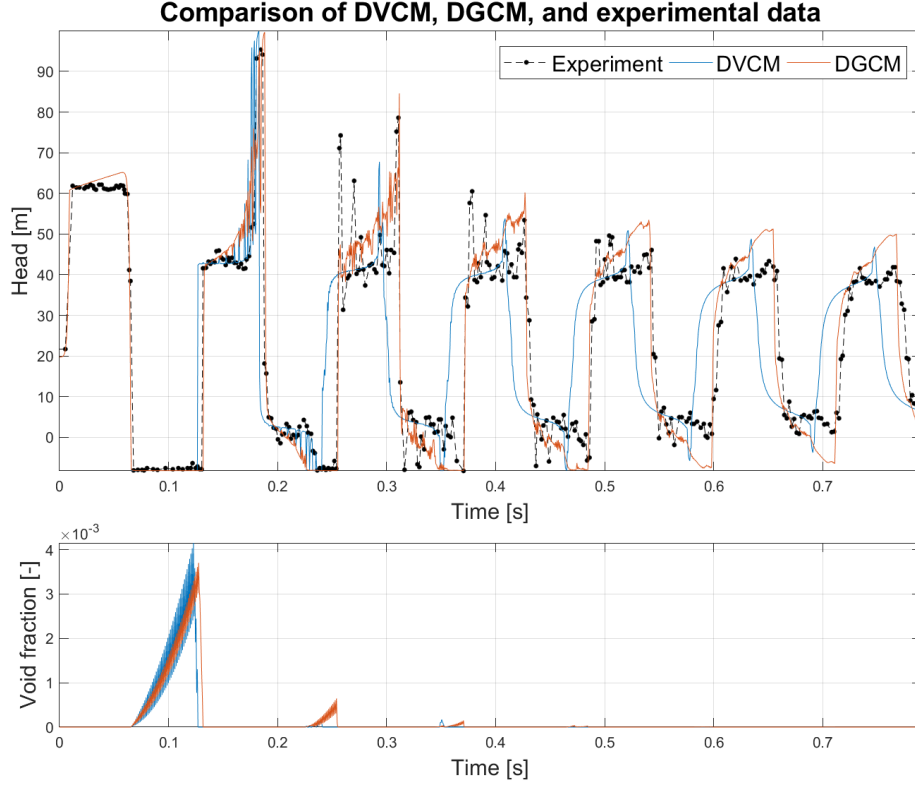


Figure 10.3: Comparison of head and void fraction for DVCM, DGCM, and the experimental data.

When comparing the high pressure peaks, using Fig. 10.4 and Table 10.3, it can be seen that for the first pressure peak, both simulations overestimates the pressure with almost +5%. For the second pressure peak the two simulations are almost identical and has a deviation of +5% from the experiment. The DGCM simulation estimates the third pressure peak much better than the DVCM simulation which underestimates the pressure with -13.8% , which is almost the case for the fourth pressure peak too. Neither of the simulations identify the first pressure peak of the high pressure zones but only the last as seen in Fig. 10.3. As the wave propagates, both simulations underestimate the dampening and as the DVCM simulation underestimates the pressure for the third and fourth peak, the size of its pressure peaks for the further peaks are close to the experimental pressure peaks.

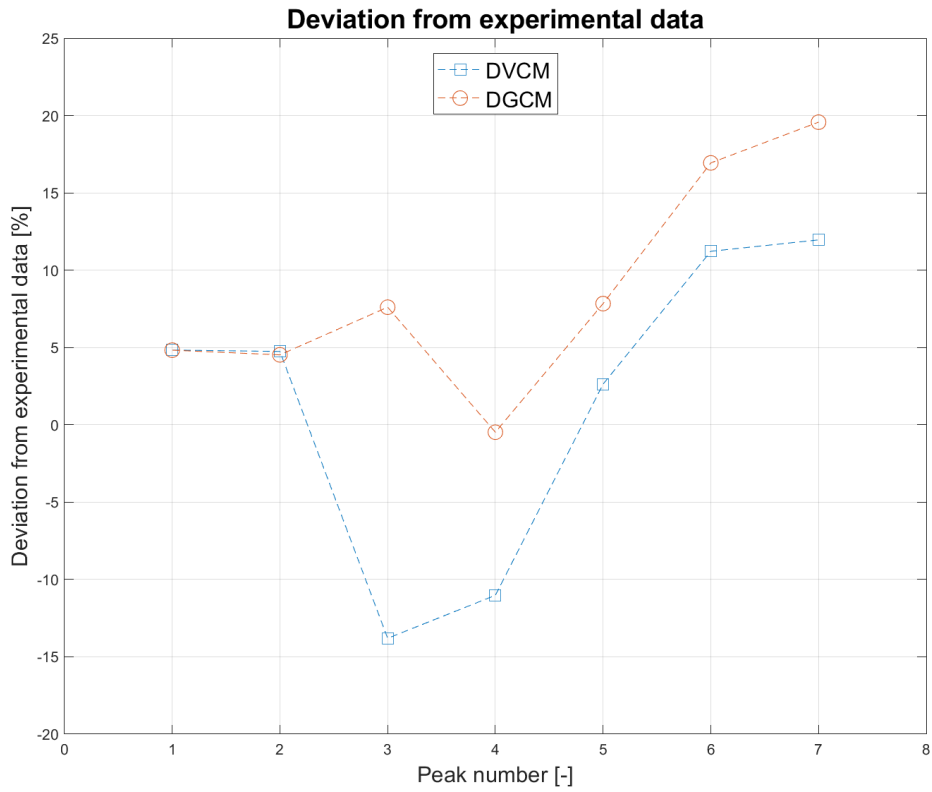


Figure 10.4: Deviation from the experimental data.

Table 10.3: Difference in head at peaks.

Peak	Experiment	DVCM		DGCM	
	Head [m]	Head [m]	Deviation [%]	Head [m]	Deviation [%]
1	62.13	65.14	4.84	65.13	4.83
2	95.37	99.90	4.75	99.69	4.53
3	78.62	67.76	-13.80	84.60	7.61
4	60.50	53.83	-11.02	60.21	-0.48
5	49.60	50.91	2.63	53.49	7.84
6	43.88	48.81	11.22	51.31	16.94
7	41.84	46.84	11.96	50.03	19.57

In the first cavitation zone, it can be seen in Fig. 10.3 that the DVCM and DGCM simulations give almost the same void fractions, whereas for the second cavitation zone it is only possible to see the void fraction for the DGCM simulation. This is because the

DGCM simulation is at vapour pressure for a longer period in the second low pressure zone.

Table 10.4: Time of period of oscillation.

Friction models	Largest	Average	Smallest
Experiment [s]	0.1561	0.1227	0.0676
DVCM [s]	0.1247	0.1149	0.1106
DGCM [s]	0.1300	0.1182	0.1129

Comparing the time period for the simulations, it can be seen from Fig. 10.3 and Table 10.4 that the average time period for the DGCM simulation is more reminiscent of the experiment compared to the DVCM simulation. In Fig. 10.3 the pressure history for the DGCM simulation has almost no phase shift whereas the DVCM simulation has a relatively large phase shift from the experiment.

Based on the size of the pressure peaks, the behaviour of the pressure waves and the phase shift, the DGCM simulation is the most precise simulation for Case 3.

10.3. BERGANT ET AL. HIGH VELOCITY EXPERIMENT

For Case 4 only the DGCM simulations gave proper results. As described in Sec. 7.5 the DVCM simulations had a too large dampening and has therefore not been included. The CFD simulation has not been included either, as it did not converge properly as described in Sec. 9.4.

Table 10.5: Difference in head at peaks.

Peak	Experiment		DGCM	
	Head [m]	Head [m]	Head [m]	Deviation [%]
1	210.69	215.53	215.53	2.30
2	204.58	212.96	212.96	4.10
3	187.40	198.32	198.32	5.83
4	164.41	197.45	197.45	20.09

Comparing the four pressure zones with Fig. 10.6 and Table 10.5, it can be seen that the DGCM simulation give an accurate estimation of the first three peaks. However, for the fourth peak, a relatively large overestimation is achieved at +20%. It is uncertain whether this increase in deviation is only for this peak or, if more data were available, the deviation would continue to increase.

It can be seen from Fig. 10.5 that the void fraction reaches almost 15% in the first cavitation zone and as the velocity decreases and the time in the cavitation zones are

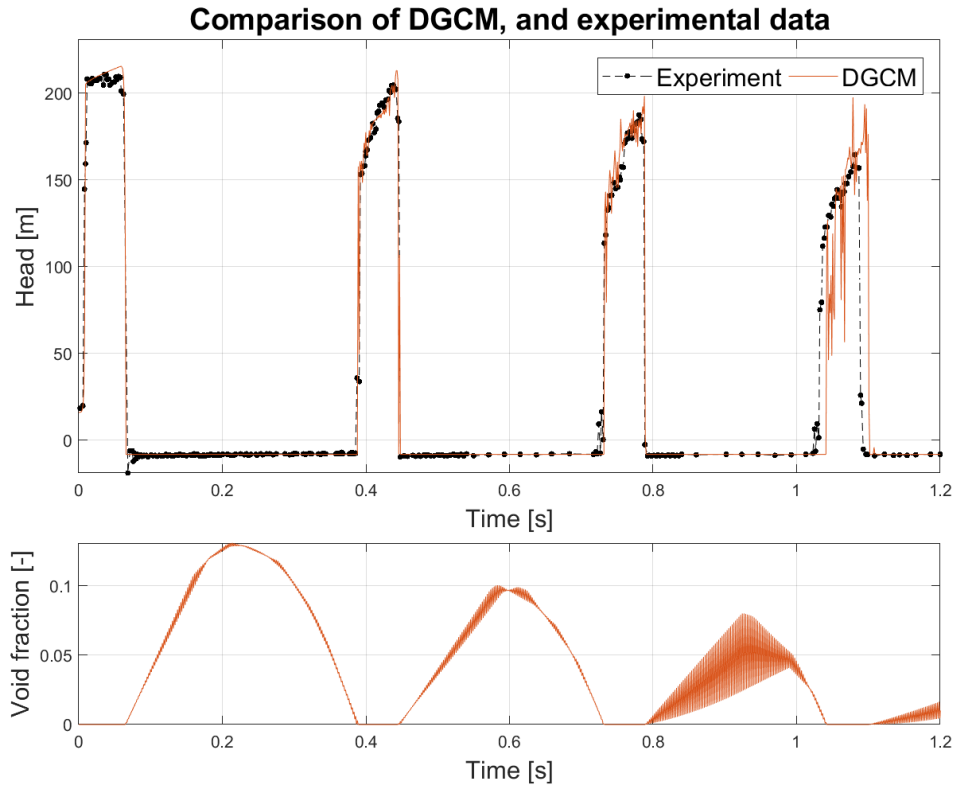


Figure 10.5: Comparison of head and void fraction for DGCM and the experimental data.

reduced, the void fractions decrease.

Table 10.6: Time of period of oscillation.

Friction models	1st	2nd	3rd
Experiment [s]	0.4024	0.3420	0.3005
DGCM [s]	0.3846	0.3446	0.2905

From Fig. 10.5 and Table 10.5, it can be seen that the time between each peak for the simulation is very reminiscent of the experiment with almost no phase shift. It can be concluded that the DGCM simulation gives an accurate estimation of the first three pressure peaks and a behaviour reminiscent of the experimental data. However, more data is needed to ensure that the damping is described properly.

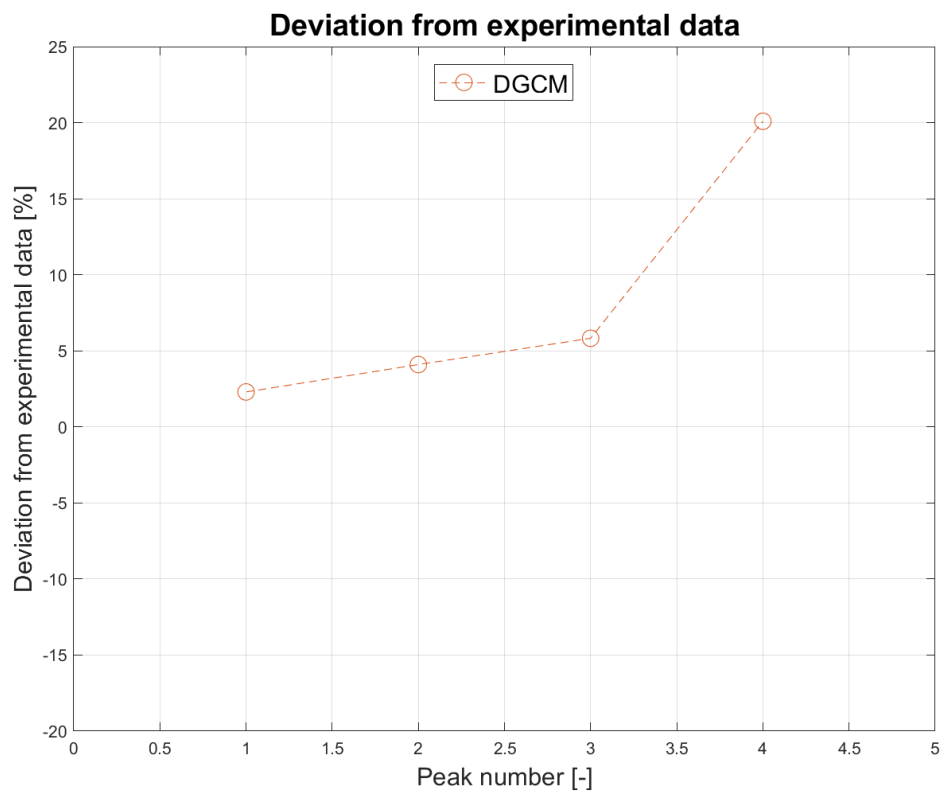


Figure 10.6: Deviation from the experimental data.

11. DISCUSSION

Comparing the results of the single phase water hammer experiment (Case 1) with simulation results showed that the best results are obtained by MOC combined with the friction model suggested by Brunone. It can also be seen that the behaviour of the pressure history with the model suggested by Brunone is similar to the one obtained with quasi-steady friction just damped. This seems to imply that the behaviour of the pressure wave is not necessarily modelled correctly, but that the dampening coefficient suggested by Vardy & Brown gives a good approximation of the friction. It can also be seen that the CFD results and the results obtained by MOC with the friction model suggested by Vardy & Brown have similar behaviour. Initially the CFD and friction model suggested by Vardy & Brown give near identical results, but as time increases they start to differ with the results obtained by CFD giving the best results. It is known that the assumption that the turbulent viscosity is constant can cause the Vardy & Brown friction model to initially give good results, but as time increases lead to discrepancies [38]. Perhaps this can partly explain why CFD and Vardy & Brown give similar results initially and start to differ with increasing time as the turbulent viscosity is updated in CFD.

The valve closure is usually modelled with Eq. 5.31 in MOC and as MOC is one dimensional the velocity is constant over the entire valve. In CFD the same valve closure is implemented with two different boundary conditions. As a mass outlet and a velocity inlet and the resulting velocity profiles are illustrated in Fig. 6.2. Both boundary conditions results in similar pressures when compared to the MOC and experiments. Therefore, it is concluded that the reverse "velocity-inlet" boundary condition is valid, if only the pressure is of interest. If the flow features at the valve is also of interest the valve should be modelled more accurately.

In CFD the fluid and wall interaction is implemented via the modified bulk modulus in Eq. 6.12. This implementation seems to be sufficient to model a water event as the pressure amplitudes and wave speed are close to the experimental values. Other methods could be used such as actually modelling the wall and fluid interaction by fluid structure interaction, if the wall behaviour is also of interest.

In two phase MOC, two different models are investigated: The DVCM and DGCM. With these two models, three different friction models are applied. To make sure that the solution has converged, a grid independency analysis is conducted. The first parameter investigated is the weighting factor, ψ , and the optimum value is decided from a grid consisting of 24 reaches. It is assumed that the optimal weighting factor at 24 reaches is the optimal value for every grid. This could potentially be incorrect and cause some extra oscillations, that another choice of weighting factor could have avoided. But because of the amount of data that otherwise would have been needed to be processed, this method was chosen. From the chosen values it can be seen that the quasi-steady friction generally needs a larger weighting function than the friction models suggested by Vardy & Brown and Brunone. A likely explanation for this is that the quasi-steady friction is known to underestimate the friction, causing the pressure to be at vapour pressure for

more low pressure zones. It is also found that the optimal number of reaches is around 24-48 reaches for all cases except for the quasi-steady friction model in Case 2, where 96 reaches is the optimal amount of reaches. Another parameter that has been observed is the void fraction at the valve. For the quasi-steady friction model, the void fraction at the valve increases with increasing reaches in all the experiments. For the friction model suggested by Brunone, there does not seem to be any clear correlation between number of reaches and the size of the void fraction in any of the experiments. For the friction model suggested by Vardy & Brown, there is an increase in the vapour void fraction in all experiments, except for in case 2 using DGCM. For all the experiments for both two phase models, it is the friction model suggested by Vardy & Brown that gives the best results. This seems to agree with the results from the conclusions of the 9th semester project, where it was concluded that the Vardy & Brown friction model is the most versatile and generally most accurate friction model for single phase flows [1]. This also indicates that the assumption, that only the skin friction between the liquid and the wall is taken into account is valid for these void fractions.

The grid independency analysis of the CFD model is only conducted for Case 2, as there are troubles with simulating Case 3 and 4. The grids tested consisted of 3000, 12000, 48000, and 192000 cells. As the number of cells are increased some of the flow features disappear that are present in the experiment, but the CFD model seems to have converged with 48000 cells. A test of three turbulence models, the Realizable $k - \epsilon$, the Standard $k - \omega$, and SST $k - \omega$ model have been made, and it was seen that all of the models gave almost identical results. The continuity residuals of the CFD models in the low pressure zones for each experiment are higher than in the high pressure zones. This indicates that there might be some convergence problems with the cavitation models. For case 2, the continuity residuals converge to a satisfactory level, while for Case 3 and 4, they converged to high values, providing inaccurate solutions. This could possibly be the reason for the overestimation of the low pressure zones in Case 3 and 4, which in turn causes the overestimation of the pressure. Another cavitation model, than the one suggested by Schnerr and Saur, was also tested, but the results obtained by Swart-Berber-Belamri gave even more inaccurate results. It is possible that the cavitation models converge better with a decrease in time step size, but this was not possible due to the length of the simulations and time restraints.

For Case 2, all the models gave satisfying results. For the second peak the best results were obtained by CFD followed by DVCM and DGCM. The third peak in the experimental data are larger than the second peak. This is surprising since the time the pressure is at vapour pressure is shorter for the third pressure peak than for the second peak. None of the models can predict the pressure of the third peak, but results obtained on second peak with DVCM were closest to the third peak of the experiment while still overestimating the pressure. Therefore, from the engineering point of view the DVCM model is chosen as the best model.

For Case 3, only DVCM and DGCM gave satisfying results. The DGCM model had some advantages compared to the DVCM model. It models the peaks from high pressure zone

2-4, which is the peaks after the vapour pressure has been attained in the underpressure, more accurately than the DVCM model. The DGCM model also accurately model the oscillation. This means that the assumption of a constant small vapour bubble gives significantly better results.

For Case 4, only DGCM gave satisfying results. Since the void fraction at the pipe for this experiment is significantly higher than for the other experiments it seems that the DVCM has some problems with large void fractions. Therefore, if large void fractions are expected the DGCM model is preferred. The void fraction of both DGCM and DVCM had a strange behaviour of decreasing while still at vapour pressure in the first low pressure zone. For the two nodes for the CFD simulation, this behaviour was not present and the void fraction only decreased after the pressure was increased above vapour pressure. Therefore, it was unfortunate that the residuals of the momentum equation were large since the development intuitively seems more realistic than the ones obtained with DVCM and DGCM.

Another parameter that is of interest, when comparing DVCM, DGCM and CFD, is the calculation time. The calculation time with DVCM and DGCM are both in the range of seconds to minutes depending on the grid, where the calculation time for CFD is in the range of days or weeks. Therefore, it is clear that the DVCM and DGCM have a clear advantage, especially when also taking the robustness into account.

The Rayleigh-Plesset equation was not implemented in a 1D model because of the difficulties explained in Sec. 8.3 and time constraints. A reason why it would be interesting to implement the Rayleigh-Plesset equation in either MOC or other methods is that perhaps it would have the same behaviour of the void fraction obtained by the CFD model for Case 4 and avoid the behaviour of DVCM and DGCM. The thought behind this is, that the cavitation model used in CFD is based on a simplified Rayleigh-Plesset equation with mass transfer.

12. CONCLUSION

In the first part, a single phase water hammer is modelled with MOC using the quasi-steady, Vardy & Brown, and Brunone friction models and with a CFD model. These models are compared to experimental data collected by Soares et al. [8] (Case 1). This comparison was done to ascertain that the boundary conditions of the CFD model were correct and see how it performed compared to MOC models. The comparison showed that the MOC utilizing the Brunone friction model outperformed the more advanced MOC model utilizing the Vardy & Brown friction model as well as the CFD model. Additionally, it was verified that the choice in boundary conditions gave no difference in pressure.

In the second part, three water hammer experiments performed by Soares et al. (Case 2) and Bergant et al. (Case 3 and 4) are modelled by the two phase MOC models DVCM and DGCM as well as a two phase CFD model. Additionally, both DVCM and DGCM are tested with the three friction models also tested in Case 1. For both DVCM and DGCM the friction model suggested by Vardy & Brown gave the best results in all three cases. It was attempted to implement the Rayleigh-Plesset equation, however a number of complications were observed and these would have to be addressed in order to continue the work.

In Case 2 the DVCM is chosen as the best model as it is the model that has the smallest deviation while overestimating the maximum pressure and giving the overall best description of the pressure from peak 4 and onwards compared to the experiment. The CFD model gave the second best results followed by the DGCM model.

In Case 3 only the DVCM and DGCM models gave satisfying results. In this case it was the DGCM model that gave the best results. The DGCM model outperformed the DVCM model when comparing the estimation of the pressure and in predicting the timing of the oscillation. CFD did not produce proper results and it is expected to be because of improper time step sizes.

In Case 4 satisfying results was only obtained with the DGCM model. The DGCM model produced an accurate estimation of the pressure and of the timing of the oscillation. The reason for the DVCM model not giving proper results is believed to be due to the high void fractions in this case.

Therefore, the overall best two phase water hammer model is the DGCM model as it is robust as it can handle large void fractions (largest void fraction seen in this study is about 15%). It also gave an accurate estimation of the pressure while never underestimating it.

REFERENCES

- [1] Rune Kjerrumgaard Jensen, Jesper Kær Larsen, and Kasper Lindgren Lassen. Comparative Study of 1D Water Hammer Friction Models. *Internal CES Conference at Aalborg University*, 2018.
- [2] Joel Carlsson. Water Hammer Phenomenon Analysis using the Method of Characteristics and Direct Measurements using a stripped Electromagnetic Flow Meter, 2016.
- [3] E. B. Wylie and V. L. Streeter. *Fluid Transients in Systems*. Prentice-Hall, 1st edition, 1993.
- [4] Christopher E. Brennen. *Cavitation and Bubble Dynamics*. Oxford University Press, 1 edition, 1995.
- [5] Y. Tomita and A. Shima. High-Speed Photographic Observations of Laser-Induced Cavitation Bubbles in Water. *ACUSTICA*, vol. 71, 1990.
- [6] C.C Bonin. Water-hammer damage to Oigawa Power Station. *ASME Journal of Engineering for Power*, vol. 82, 1960.
- [7] A. Bergant, J.M.C. van 't Westende, T. Koppel, J. Gale, Q. Hou, Z. Pandula, and A.S. Tijsseling. Water hammer and column separation due to accidental simultaneous closure of control valves in a large scale two-phase flow experimental test rig. *CASA-report*, vol. 1037, 2010.
- [8] Alexandre K. Soares, Nuno Martins, and Dídia I.C. Covas. Investigation of Transient Vaporous Cavitation: Experimental and Numerical Analyses. *Procedia Engineering*, 119:235–242, 2015.
- [9] A. Bergant, U. Karadzic, J. Vitkovsky, I. Vusanovic, and A. R. Simpson. A Discrete Gas-Cavity model that Considers the Friction Effects of Unsteady Pipe Flow. *Journal of Mechanical Engineering*, vol. 51, 2005.
- [10] M. Casey and T. Wintergerste. *ERCRAFTAC Special Interest Group on "Quality and Trust in Industrial CFD" - Best Practice Guidelines*. ERCRAFTAC, ver. 1 edition, January 2000.
- [11] P. G. Provenzano, F. Baroni, and R. J. Aguerre. The Closing Function in the Waterhammer Modeling. *Latin American Applied Research*, 2011.
- [12] John Vítkovský, Angus R. Simpson, and Anton Bergant. Advances in unsteady friction modelling in transient pipe flow. *The 8th international conference on pressure surges*, 2000.
- [13] M. H. Chaudry. *Applied Hydraulic Transients*. Springer, 3rd edition, 2014.

- [14] A. Adamkowski and M. Lewandowski. Experimental examination of unsteady friction models for transient pipe flow simulation. *Journal of Fluids Engineering*, vol. 128, 2006.
- [15] M.-F. Duan, M. S. Ghidaoui, P. J. Lee, and Y. K. Tung. Relevance of unsteady friction to pipe size and length in pipe fluid transients. *Journal of Hydraulic Engineering*, vol. 138:157–166, 2012.
- [16] W. Zielke. Frequency-dependent friction in transient pipe flow. *Journal of basic engineering*, vol. 91, 1969.
- [17] Bruno Brunone, Bryan W. Karney, Michele Mecarelli, and Marco Ferrante. Velocity profiles and unsteady pipe friction in transient flow. *Journal of water resources, planning and management*, vol. 126:236–244, 2000.
- [18] A. E. Vardy and J. M. B. Brown. Transient turbulent friction in smooth pipe flows. *Journal of sound and vibration*, vol. 259:1011–1036, 2003.
- [19] Yunus A. Cengel, John M. Cimbala, and Robert H. Turner. *Fundamentals of Thermal-Fluid Sciences*. McGraw-Hill, 4 edition, 2012.
- [20] K. Urbanowicz and Z. Zarzycki. Convolution integral in transient pipe flow. *Task Quarterly 16 no. 3-4*, 2012.
- [21] Anton Bergant, Angus R. Simpson, and John Vítkovský. Developments in unsteady pipe flow friction modelling. *Journal of hydraulic research*, vol. 39:249–257, 2001.
- [22] John Vítkovský, Martin Lambert, Angus Simpson, and Anton Bergant. Advances in unsteady friction modelling in transient pipe flow. In *The 8th international conference on pressure surges*, 2000.
- [23] ANSYS, Inc. *Fluent User’s Guide*, 2018. Release 19.0.
- [24] M. R. Nikpour, A. H. Nazemi, A. Hosseinzadeh Dalir, F. Shoja, and P. Varjavand. Experimental and Numerical Simulation of Water Hammer. *Arabian Journal for Science and Engineering*, vol. 39:2669–2675, 2014.
- [25] A. R. Simpsons and A. Bergant. Numerical comparison of pipe-column-separation models. *Journal of Hydraulic Engineering*, vol. 120, 1994.
- [26] Z. Zarzycki, Sylwester Kudzma, and Kamil Urbanowicz. Improved method for simulating transients of turbulent pipe flow. *Journal of theoretical and applied mechanics*, vol. 49:135–158, 2011.
- [27] D. Jiang, S. Li, K. A. Edge, and W. Zeng. Modeling and Simulation of Low Pressure Oil-Hydraulic Pipeline Transients. *Computers & Fluids*, vol. 67, 2012.
- [28] J. P. Th. Kalwijk and C. Kranenburg. Cavitation in horizontal pipelines. Technical report, Delft University of Technology, 1971.

- [29] J. Sauer and G. H. Schnerr. Unsteady cavitating flow - a new cavitation model based on a modified front capturing method and bubble dynamics. In *Proceedings of FEDSM'00 - 2000 ASME Fluids Engineering Summer Conference*, 2000.
- [30] K. S. Suslick and D. J. Flannigan. Inside a collapsing bubble: Sonoluminescence and the conditions during cavitation. *Annual Review of Physical Chemistry*, vol. 59, 2008.
- [31] H. Alehossein and Z. Qin. Numerical analysis of rayleigh-plesset equation for cavitating water jets. *International Journal for Numerical Methods in Engineering*, vol. 72:780–807, 2012.
- [32] H. S. Lee and H. Merte JR. Spherical vapor bubble growth in uniformly superheated liquids. *International Journal of Heat and Mass Transfer*, vol. 39:2427–2447, 1996.
- [33] MATLAB. *version 9.3.0.713579 (R2017b)*. The MathWorks Inc., 2017.
- [34] Günter H. Schnerr and Jürgen Sauer. Physical and Numerical Modeling of Unsteady Cavitation Dynamics. *4th International Conference on Multiphase Flow*, 2001.
- [35] Huan Wang, Ling Zhou, Deyou Liu, Bryan Karney, Pei Wang, Lin Xia, Jiajie Ma, and Chang Xu. CFD Approach for Column Separation in Water Pipelines. *Journal of Hydraulic Engineering*, vol. 142, 2016.
- [36] Xiaoxi Zhang, Yongguang Cheng, Linsheng Xia, and Jiandong Yang. CFD simulation of reverse water-hammer induced by collapse of draft-tube cavity in a model pumpturbine during runaway process. *IOP Conference Series: Earth and Environmental Science* 49, 2016.
- [37] Marcus Jansson, Magnus Andersson, Maria Pettersson, and Matts Karlsson. CFD simulation of reverse water-hammer induced by collapse of draft-tube cavity in a model pumpturbine during runaway process. *The 15th Scandinavian International Conference on Fluid Power*, 2017.
- [38] A. Rufelt. Numerical studies of unsteady friction in transient pipe flow. Master's thesis, KTH Computer Science and Communication, 2010.

APPENDIX

A. RAYLEIGH-PLESSET EQUATION DERIVATION

The full derivation of the Rayleigh-Plesset equation, Eq. (8.4), from the conservation of mass and momentum for a bubble experiencing cavitation is presented in this appendix. In Fig. A.1 a single bubble surrounded by liquid is illustrated.

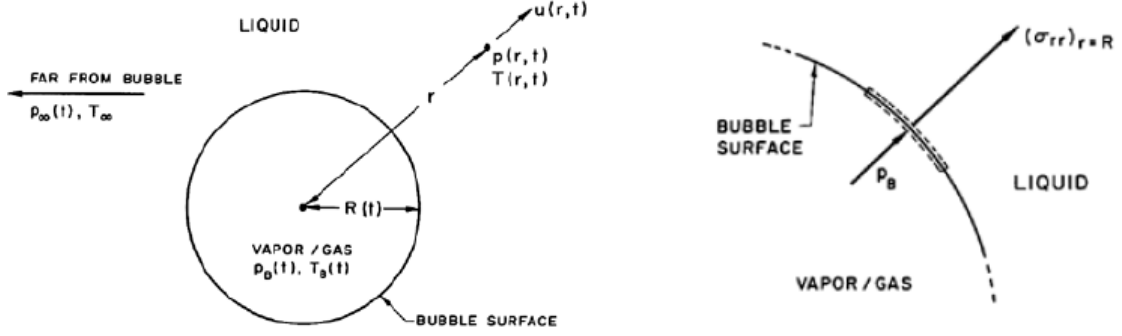


Figure A.1: On the left side is illustrated the bubble in a liquid and on the right a slice of the bubble interface. [4]

A.1. MASS CONSERVATION

Conservation of mass requires that the radial outward velocity, $u(r, t)$, is inversely proportional to the square of distance from the center of bubble.

$$u(r, t) = \frac{F(t)}{r^2} \quad (\text{A.1})$$

Where $F(t)$ is a function that is related to the radius at the bubble/liquid interface. Therefore to determine $F(t)$, the radial outward velocity at R , $u(R, t)$, must be determined. The first step is to write the mass conservation of the bubble. Which is the change in mass of the vapour equal to the change in mass of the liquid, as in Eq. (A.2).

$$\frac{dm_v}{dt} = \frac{dm_l}{dt} \quad (\text{A.2})$$

Where m_v is the vapour mass and m_l is the liquid mass. The change in the mass of vapour must be related to the change in bubble volume, as in Eq. (A.3), and the change in the mass of liquid is related to the liquid flow through the bubble interface, as in Eq. (A.4).

$$\frac{dm_v}{dt} = \rho_v \frac{dV_v}{dt} = 4\pi\rho_v R^2 \frac{dR}{dt} \quad (\text{A.3})$$

$$\frac{dm_l}{dt} = \rho_l A u_l = 4\pi\rho_l R^2 u_l \quad (\text{A.4})$$

Solving for u_l in Eq. (A.2) yields:

$$u_l = \frac{\rho_v}{\rho_l} \frac{dR}{dt} \quad (\text{A.5})$$

Then $u(R, t)$ is:

$$u(R, t) = \frac{dR}{dt} - \frac{\rho_v}{\rho_l} \frac{dR}{dt} = \left(1 - \frac{\rho_v}{\rho_l}\right) \frac{dR}{dt} \quad (\text{A.6})$$

Then $F(t)$ is:

$$F(t) = R^2 u(R, t) = \left(1 - \frac{\rho_v}{\rho_l}\right) R^2 \frac{dR}{dt} \quad (\text{A.7})$$

Then it can be seen that if $\rho_v \ll \rho_l$, as is normal for vapour and water, Eq. (A.7) simplifies to:

$$F(t) = R^2 \frac{dR}{dt} \quad (\text{A.8})$$

Inserting Eq. (A.8) into (A.1) yields:

$$u(r, t) = \frac{R^2}{r^2} \frac{dR}{dt} \quad (\text{A.9})$$

A.2. MOMENTUM CONSERVATION

The Navier-Stokes equation for motion in the radial direction is:

$$\rho_l \left(\frac{\partial u}{\partial t} + u \frac{\partial u}{\partial r} \right) = -\frac{\partial P}{\partial r} + \mu_l \left(\frac{1}{r^2} \frac{\partial}{\partial r} \left(r^2 \frac{\partial u}{\partial r} \right) - \frac{2u}{r^2} \right) \quad (\text{A.10})$$

Rearranging Eq. (A.10) so that the pressure term is isolated:

$$-\frac{\partial P}{\partial r} = \rho_l \left(\frac{\partial u}{\partial t} + u \frac{\partial u}{\partial r} \right) - \mu_l \left(\frac{1}{r^2} \frac{\partial}{\partial r} \left(r^2 \frac{\partial u}{\partial r} \right) - \frac{2u}{r^2} \right) \quad (\text{A.11})$$

Utilizing that the total derivative of $u(R, t)$ is equal to $\frac{\partial u}{\partial t} = \frac{\partial u}{\partial t} + \frac{dR}{dt} \frac{\partial u}{\partial R}$ and inserting u from Eq. (A.9) into Eq. (A.11) yields:

$$-\frac{\partial P}{\partial r} = \rho_l \left(\frac{R^2}{r^2} \frac{d^2 R}{dt^2} + \frac{2R}{r^2} \left(\frac{dR}{dt} \right)^2 - \frac{2R^4}{r^5} \left(\frac{dR}{dt} \right)^2 \right) \quad (\text{A.12})$$

Note that with the substitution of u the viscous terms cancel out. Then integrating Eq. (A.12) from R to infinitely far away from the bubble, as in Eq. (A.13), yields Eq. (A.14).

$$-\int_{P(R)}^{P(\infty)} dP = \rho_l \int_R^\infty \left(\frac{R^2}{r^2} \frac{d^2 R}{dt^2} + \frac{2R}{r^2} \left(\frac{dR}{dt} \right)^2 - \frac{2R^4}{r^5} \left(\frac{dR}{dt} \right)^2 \right) dr \quad (\text{A.13})$$

$$P(R) - P_\infty = \rho_l \left(R \frac{d^2 R}{dt^2} + \frac{3}{2} \left(\frac{dR}{dt} \right)^2 \right) \quad (\text{A.14})$$

A.3. BUBBLE BOUNDARY CONDITION

The last thing needed is to evaluate the boundary condition at the bubble interface. If it is assumed that the bubble interface is infinitely thin and there is no mass transfer across the interface, then the net force per area acting at the interface is:

$$\sigma_{rr}(R) + P_B - \frac{2S}{R} = 0 \quad (\text{A.15})$$

Where P_B is the internal bubble pressure, S is the surface tension and $\sigma_{rr}(R)$ is the normal stress evaluated at R pointing out radially from the bubble center. $\sigma_{rr}(R)$ is defined as in Eq. (A.16).

$$\sigma_{rr}(R) = -P(R) + 2\mu_l \frac{\partial u}{\partial r} \Big|_{r=R} = -P(R) - \frac{4\mu_l}{R} \frac{dR}{dt} \quad (\text{A.16})$$

Inserting the result of Eq. (A.16) into Eq. (A.15) and solving for $P(R)$ yields:

$$P(R) = P_B - \frac{4\mu_l}{R} \frac{dR}{dt} - \frac{2S}{R} \quad (\text{A.17})$$

Then the last step to get the Rayleigh-Plesset equation is substituting $P(R)$ from Eq. (A.17) into Eq. (A.14).

$$\rho \left(R \frac{d^2 R}{dt^2} + \frac{3}{2} \left(\frac{dR}{dt} \right)^2 \right) = P_B - P_\infty - \frac{2S}{R} - \frac{4\mu}{R} \frac{dR}{dt} \quad (\text{A.18})$$

B. USER DEFINED FUNCTION

```
1 #include "udf.h"
2
3 DEFINE_PROFILE(Velocity_magnitude, t, i)
4 {
5     real velocity;
6     real the_current_time;
7     face_t f;
8
9     the_current_time = CURRENT_TIME;
10
11     if ((the_current_time >= 0) && (the_current_time < 0.018))
12     {
13         velocity = -0.4966 * (1 - pow((the_current_time / 0.018), 5));
14     }
15     if ((the_current_time >= 0.018))
16     {
17         velocity = 0;
18     }
19
20
21     begin_f_loop(f, t)
22     {
23         F_PROFILE(f, t, i) = velocity;
24     }
25     end_f_loop(f, t)
26 }
```

C. GRID INDEPENDENCY ANALYSIS

C.1. BERGANT ET AL. - LOW VELOCITY EXPERIMENT

The grid independency analysis was performed on meshes with 6, 12, 24, 48, 96, and 192 reaches respectively for each friction model for each two phase model. For the analysis, three parameters were investigated, the head at the valve over time, the void fraction at the valve over time, and the total amount of vapour/gas in the pipe over time. As with Case 2, there can be problems with an increased amount of vapour/gas as the number of reaches increases.

In Table C.1, it is possible to see which mesh has been chosen for each friction model, with their corresponding two phase model. It can be seen that DVCM with Brunone, DVCM with Vardy & Brown, and DGCM with Vardy & Brown requires 48 reaches while the remaining combinations use the recommended mesh.

Table C.1: Number of reaches in the appropriate mesh for each friction model.

Friction models	DVCM	DGCM
Quasi-steady	24	24
Brunone	48	24
Vardy & Brown	48	48

For DVCM with the quasi-steady friction model (see Fig. C.1), the mesh with 24 reaches was chosen because of a lack of double peaks on high pressure zone 4-7. The reason for this lack being deemed more accurate, is because there is no consistency in when the first of each double peaks happens on the high pressure zone, and what size they have. When looking at α , it can be seen that as the number of reaches increase, the void fraction increases. However, the total amount of vapour in the pipe is relatively constant when the number of reaches increase, which could indicate that more of the vapour is formed in the valve, when a higher number of reaches is used.

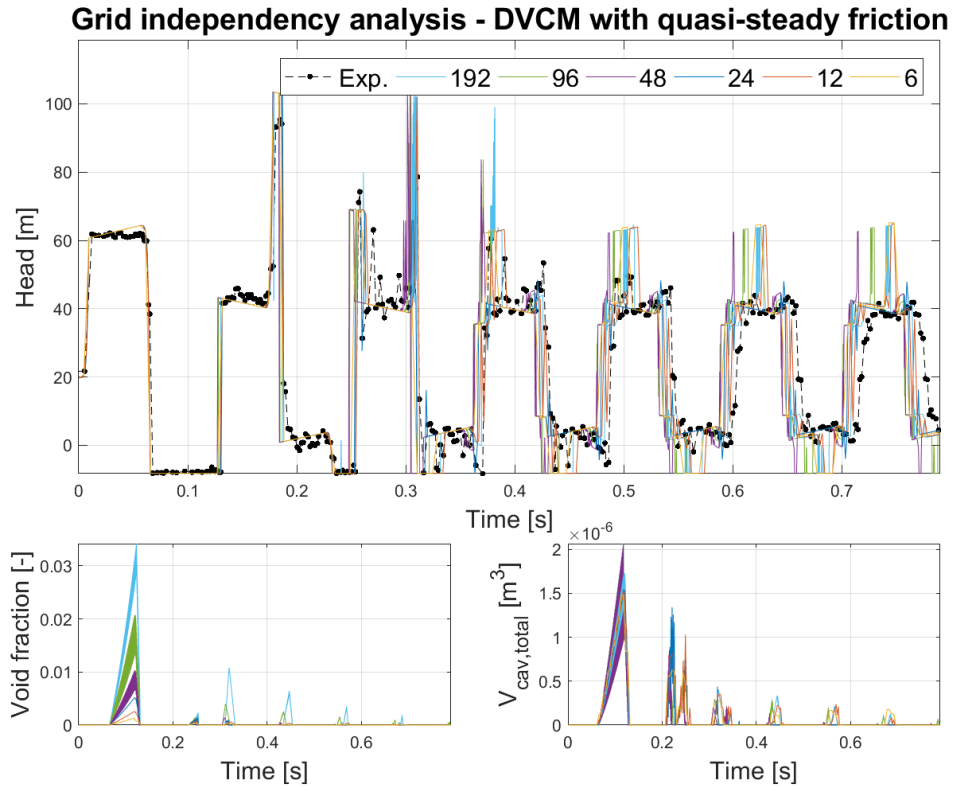


Figure C.1: Grid independency analysis of Case 3 with DVCM using the quasi-steady friction model.

For DVCM with Brunone’s unsteady friction model (see Fig. C.2), the mesh with 48 reaches was chosen because of a relatively small difference in head and total vapour volume between the mesh with 24, 48, and 96 reaches. It was observed that the first peak on the third high pressure became smaller and smaller as the amount of reaches increased and it was therefore chosen to use the mesh with 48 reaches rather than 24 reaches, because this first peak was way smaller than for 24 reaches. When looking at α , there were no consistency for what happened when the number of reaches were increased. An increase was seen when the number of reaches was increase from 6 to 48 reaches, however this was followed by a decrease for 96 reaches. For 192 reaches, an increase was seen again, but the behaviour of the void fraction increase over time was also different compared to the other meshes. Despite the inconsistency in α , the total amount of vapour still remained relatively constant when the amount of reaches increased.

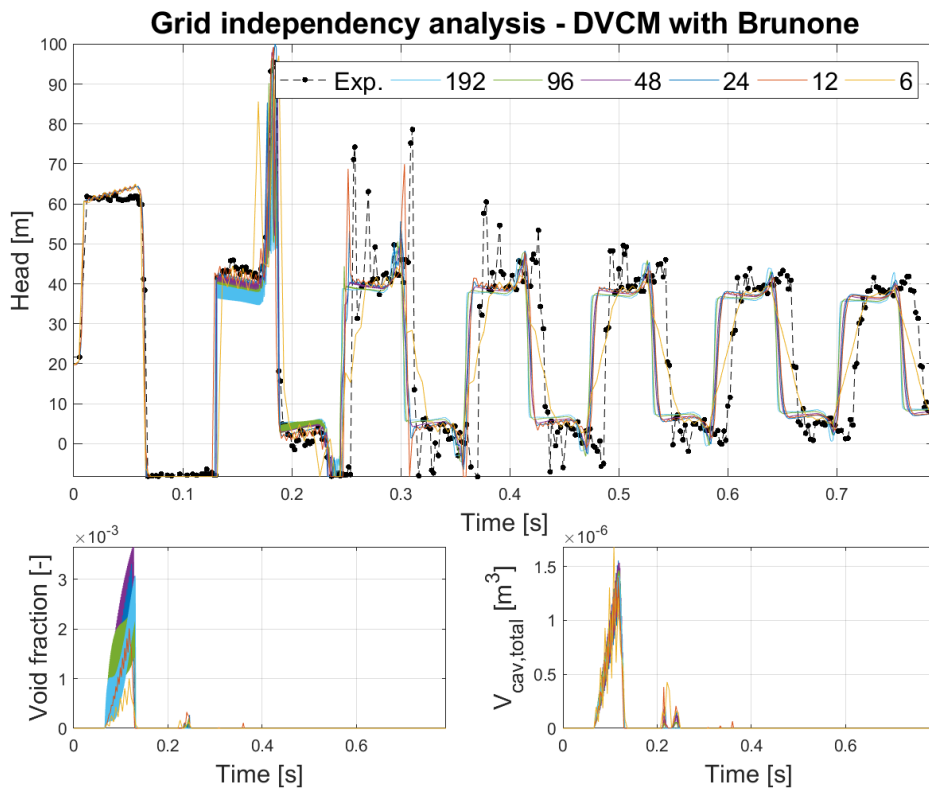


Figure C.2: Grid independency analysis of Case 3 with DVCM using Brunone’s unsteady friction model.

For DVCM with Vardy & Brown's unsteady friction model (see Fig. C.3), the mesh with 48 reaches was chosen. The mesh with 24 reaches was not chosen because it had a lower head at most of the peaks compared to the mesh with 48, 96, and 192 reaches. The mesh 96 and 192 reaches were not chosen because they both had an extra peak on the third and fourth high pressure zone, which was not seen in any of the other meshes. When looking at α , it was seen that as the amount of reaches increased, the size of α also increased, which was also seen in DVCM using the quasi-steady friction model. However, the total amount of vapour in the pipe still remained relatively constant, which indicates that more vapour is formed at the valve as the number of reaches increase. This behaviour for Vardy & Brown's unsteady friction model was also seen for the other unsteady friction models, which were used in the previous work (Zielke and Zarzycki), which was also seen for Case 2.

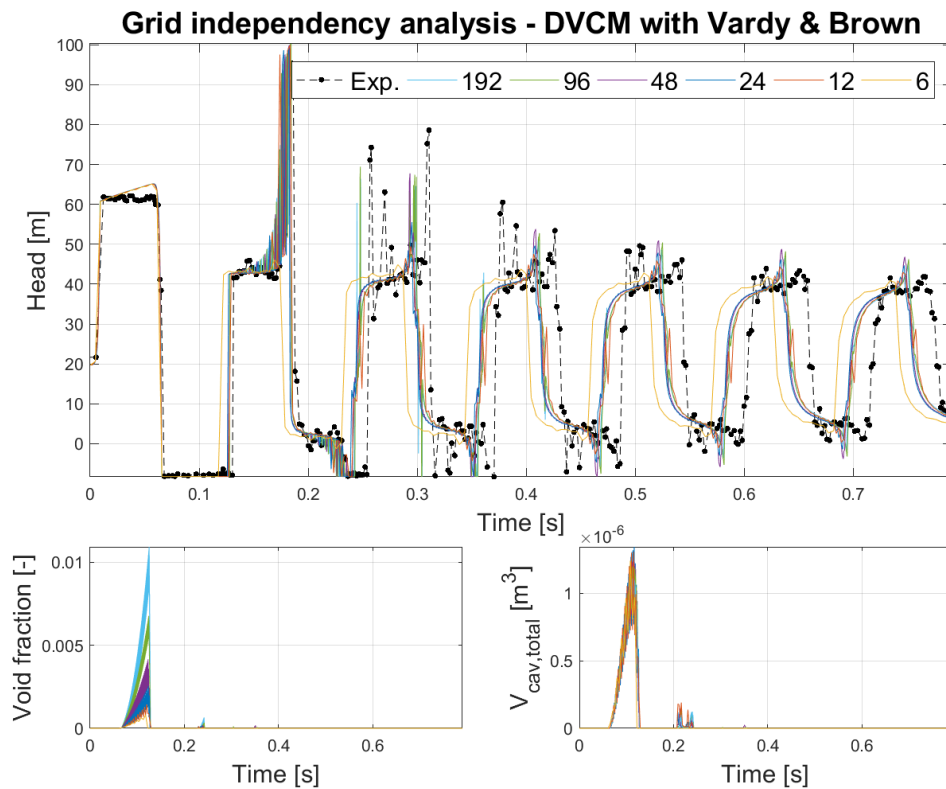


Figure C.3: Grid independency analysis of Case 3 with DVCM using Vardy & Brown's unsteady friction model.

For DGCM with the quasi-steady friction model (see Fig. C.4), the mesh with 24 reaches was chosen because it had many features from the mesh with 48, 96, 192 reaches, while not having a very large peak on the fifth and sixth high pressure zone. The mesh with 12 reaches was not chosen because it had a phase shift not seen on any of the other. The mesh with 48 and 192 reaches was not chosen because they had a very large peak on the fifth high pressure zone, which is very late for such a high pressure peak. The mesh with 96 reaches was not chosen because it had a similar peak, which happened at the sixth high pressure zone. When looking at α , the same tendency as for DVCM using quasi-steady friction was observed, however with significantly less numerical oscillation. Again, it was also seen that the total gas volume in the pipe remained relatively constant.

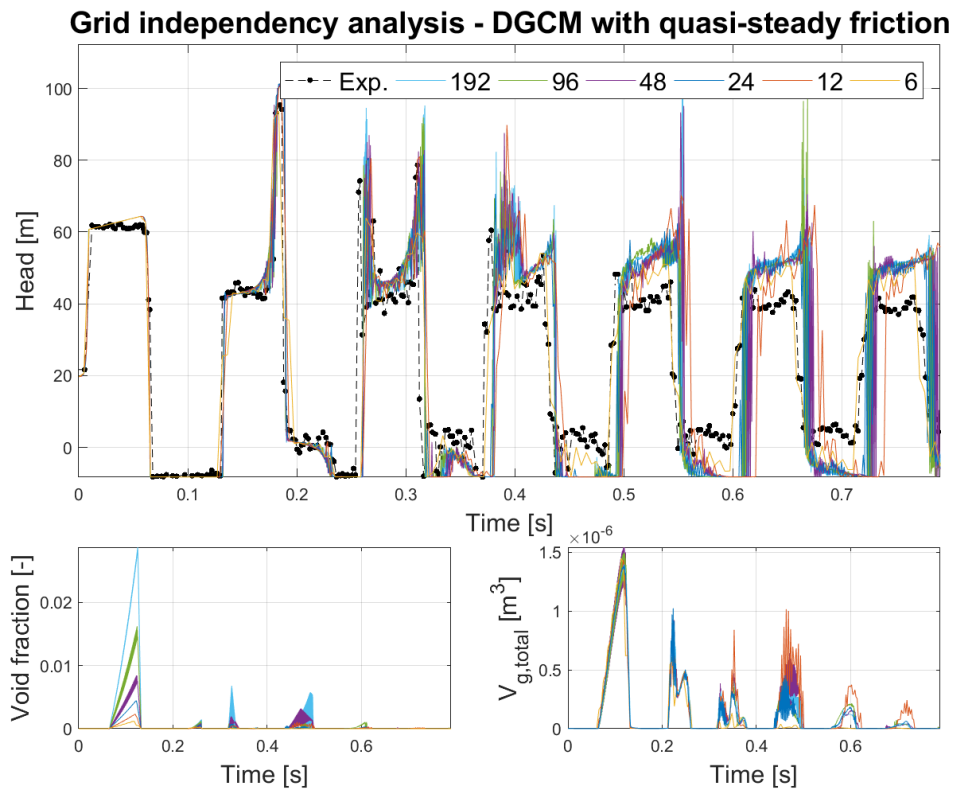


Figure C.4: Grid independency analysis of Case 3 with DGCM using the quasi-steady friction model.

For DGCM with Brunone’s unsteady friction model (see Fig. C.5), the mesh with 24 reaches was chosen because there were no clear convergence for the head. It was seen that as the number of reaches increased, the amount of damping between each high pressure zone increased. The reason for choosing the mesh with 24 reaches over the others is because it had the highest head at four out of six high pressure zones (not including the first high pressure zone). The two high pressure zones where the mesh with 24 reaches was not highest is the third and fourth, where the mesh with 6 reaches has the highest head. When looking at α , the same tendency as for DVCM using Brunone’s unsteady friction model was observed, i.e. no consistency in size when the number of reaches increased, but with less numerical oscillation. The same tendency was also observed for the total amount of gas in the pipe, which remained relatively constant as the number of reaches increased.

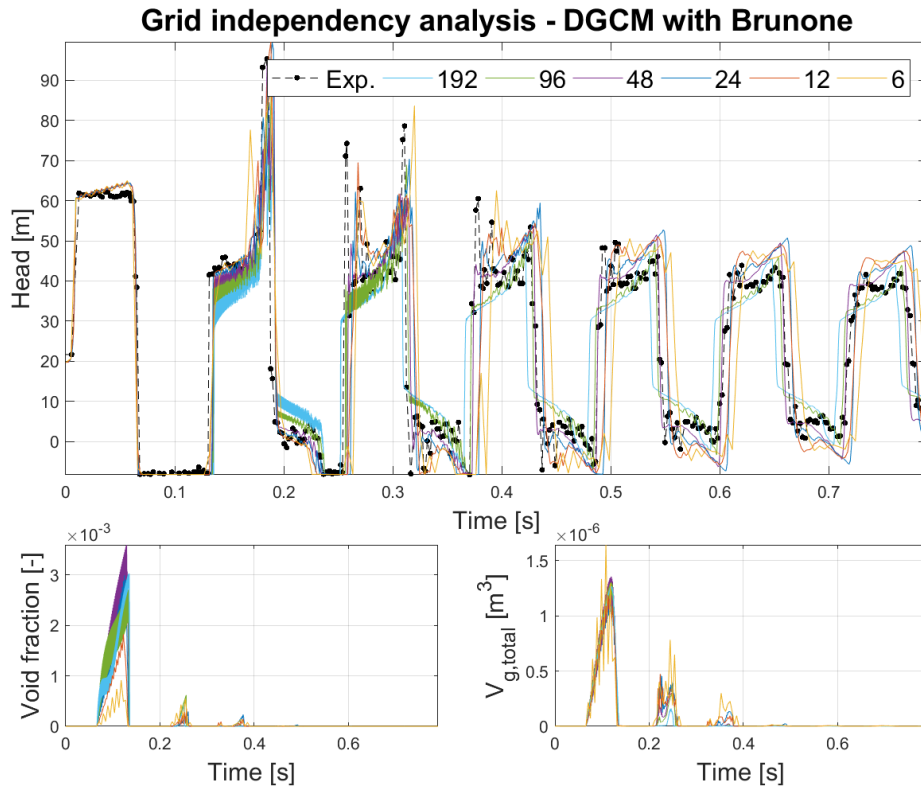


Figure C.5: Grid independency analysis of Case 3 with DGCM using Brunone’s unsteady friction model.

For DGCM with Vardy & Brown’s unsteady friction model (see Fig. C.6), the mesh with 48 reaches was chosen because of relatively small difference in head and the total gas volume between the mesh with 48, 96, and 192 reaches. The mesh with 24 reaches was not chosen because it had two peaks on each high pressure zone after the second high pressure zone, which was not seen for any of the other meshes. When looking at α , the same tendency as for DVCM, using Vardy & Brown, was observed, where α increases as the number of reaches increase. However, for DGCM, there is significantly less numerical oscillation. The same tendency was also observed for the total gas volume in the pipe, with a relatively constant amount as the number of reaches increase.

The behaviour for DGCM using Vardy & Brown’s unsteady friction model was, as with DVCM, the same for the other unsteady friction models used in the previous work. This supports the conclusion from Sec. 7.3.1, that the choice of convolution based unsteady friction model is of less importance when modelling a two phase water hammer.

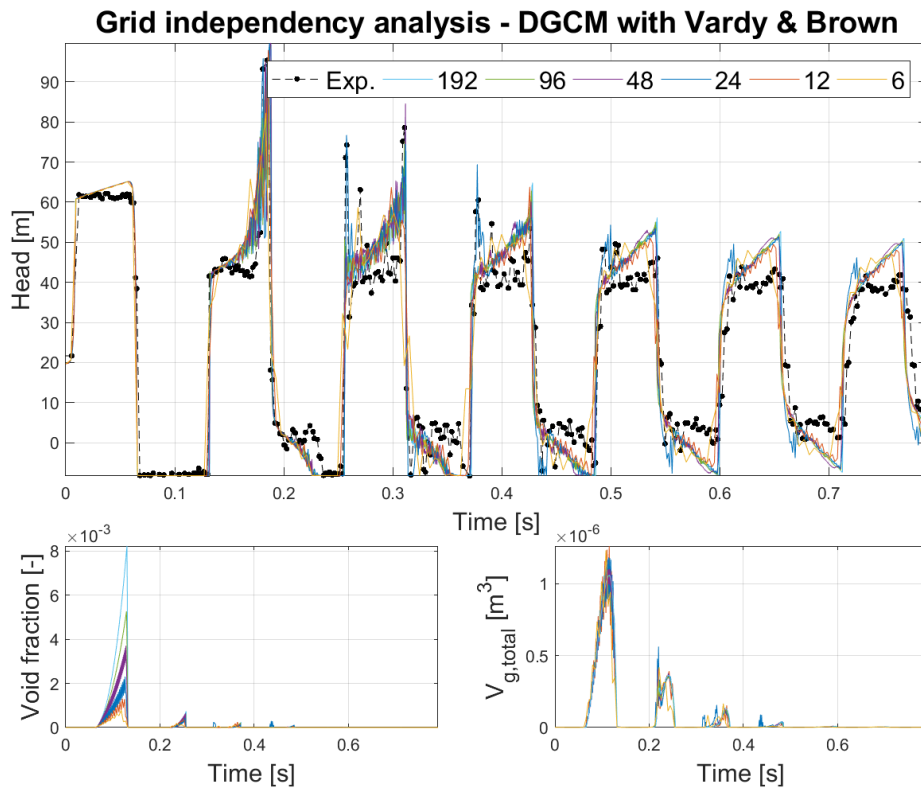


Figure C.6: Grid independency analysis of Case 3 with DGCM using Vardy & Brown’s unsteady friction model.

The friction models, with the chosen mesh, are compared for DVCM and DGCM respectively in Sec. 7.4.1.

C.2. BERGANT ET AL. - HIGH VELOCITY EXPERIMENT

The grid independency analysis was performed on meshes with 6, 12, 24, 48, 96, and 192 reaches for Brunone and Vardy & Brown using DGCM. For the analysis, three parameters were investigated, the head at the valve over time, the void fraction at the valve over time, and the total amount of gas in the pipe over time. As with Case 2, there can be problems with an increased amount of gas as the number of reaches increases.

In Table 7.14 it is possible to see which mesh has been chosen for Brunone and Vardy & Brown. It can be seen that both friction models uses the recommended mesh.

Table C.2: Number of reaches in the appropriate mesh for each friction model.

Friction models	DGCM
Brunone	24
Vardy & Brown	24

For DGCM using Brunone's unsteady friction model (see Fig. C.7), the mesh with 24 reaches was chosen because of a relatively small difference in head and the total gas volume between the mesh with 24, 48, 96, and 192 reaches. The mesh with 12 reaches was not chosen because it had higher head at the second and third high pressure zones. When looking at α , the same strange behaviour as described in Sec. 7.5 can be seen and it is unknown if the behaviour for 24 or 48 reaches is the correct behaviour. There is a relatively high void fraction for the mesh with 6 and 24 reaches (maximum at 0.366), while the mesh with 12 reaches is below 0.2. The other 3 meshes are all below 0.14. For the total amount of gas in the pipe, all mesh sizes have relatively similar values for the first cavitation zone, with varying degree of numerical oscillation.

For DGCM using Vardy & Brown's unsteady friction model (see Fig. C.8), the mesh with 24 reaches was chosen because of relatively small difference in head and the total gas volume between the mesh with 24 and 48 reaches. The mesh with 96 and 192 reaches were not considered because they had a too high void fraction. The mesh with 12 reaches was not chosen because of the amount of numerical oscillation present on the third high pressure zone. When looking at α , it can be seen that the void fraction increases when the number of reaches is increased. However, the total amount of gas in the pipe remains relatively constant, not accounting for the extreme amount of numerical oscillation in the mesh with 48 reaches.

The friction models, with the chosen mesh, are compared for DVCM and DGCM respectively in Sec. 7.5.1.

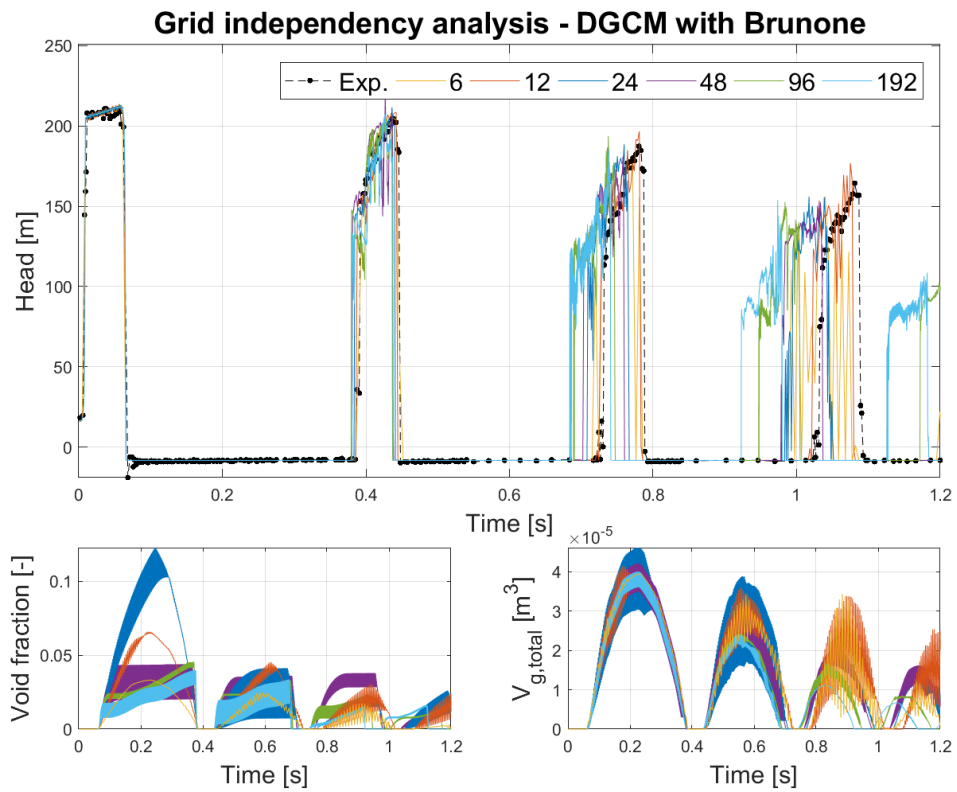


Figure C.7: Grid independency analysis of Case 4 with DGCM using Brunone's unsteady friction model.

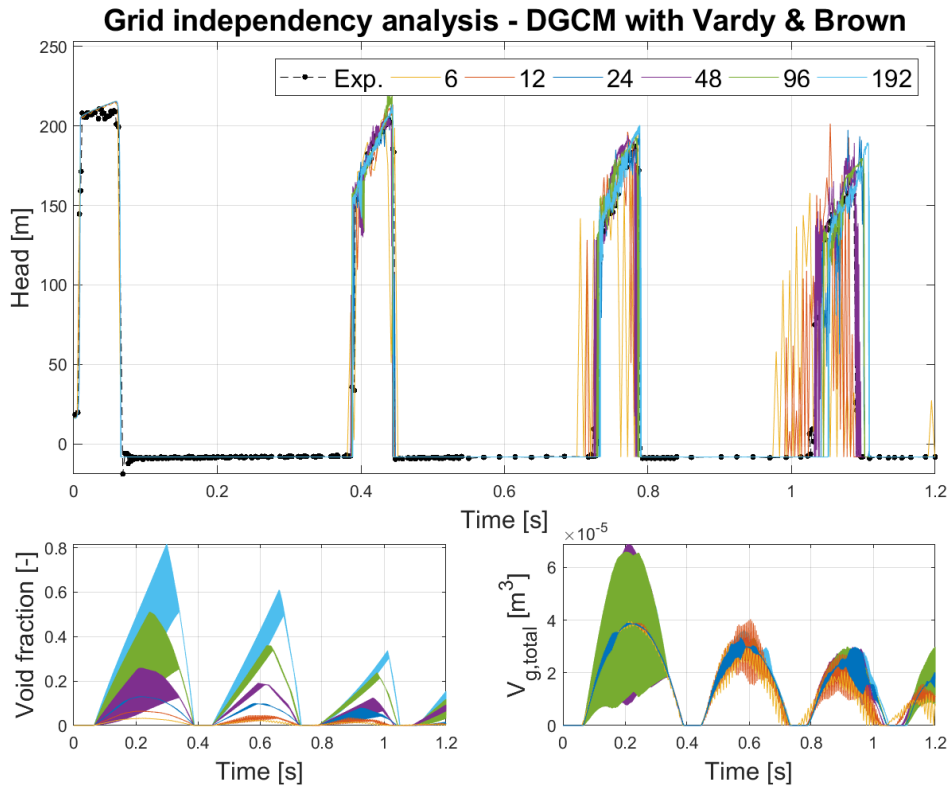


Figure C.8: Grid independency analysis of Case 4 with DGCM using Vardy & Brown's unsteady friction model.

D. MATLAB CODE

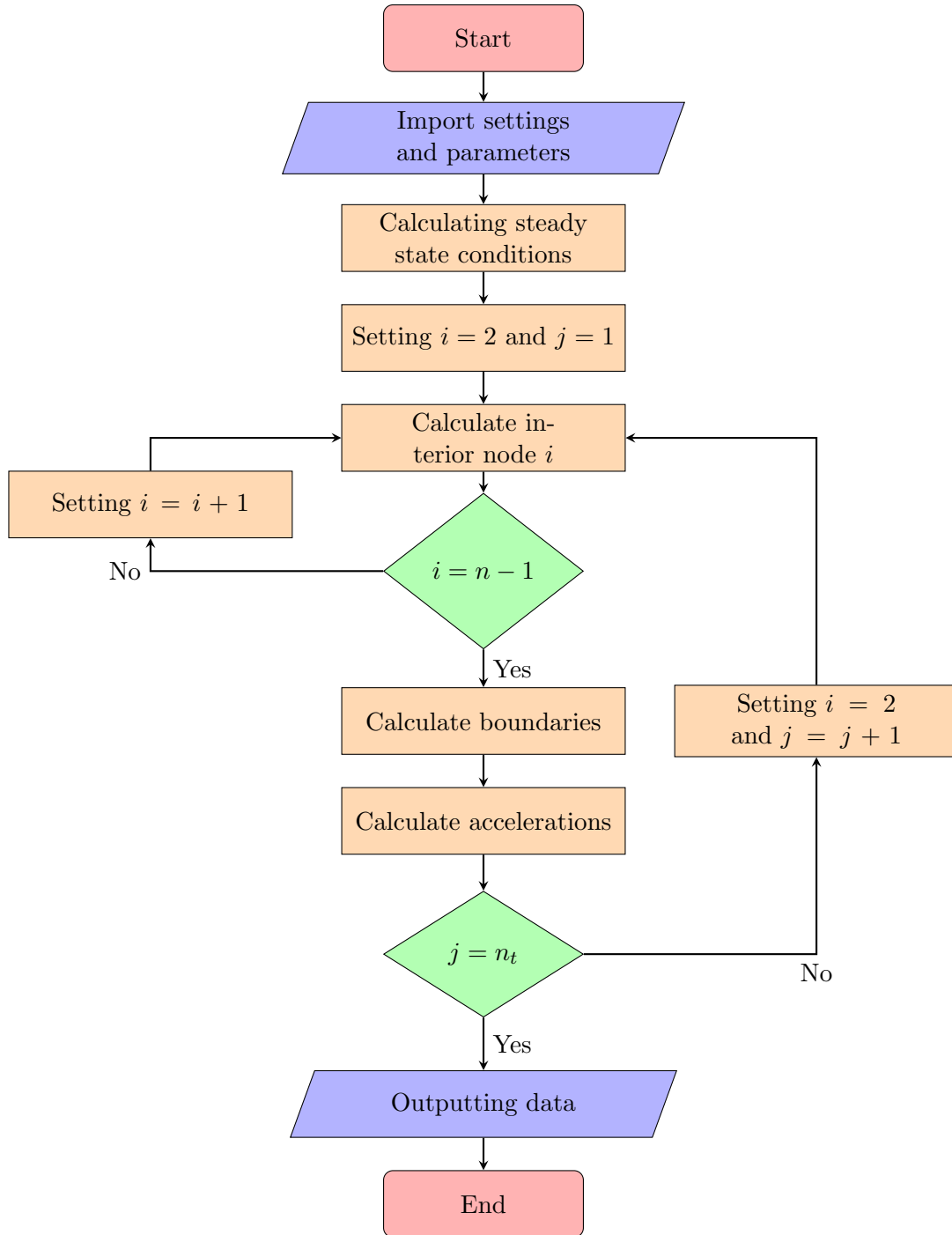


Figure D.1: Flow chart of the MOC code in Matlab.

MASTER

```
1 %%-%%-%%-%% MASTER %%-%%-%%-%%
2 clear
3 clc
4
5 %% Starting timer
6 tic
7
8 %% Adding folders to directory
9 addpath('Functions','Output','Solver','Solver\Boundary',...
10        'Solver\InteriorNodes','Solver\SteadyState','Output\Plot','Input')
11
12 %% Specify Input File
13 %Input
14 %Input_OnePhase_Traudt
15 %Input_OnePhase_Covas
16 %Input_OnePhase_Adamkowski
17 %Input_OnePhase_Soares
18 %Input_TwoPhase_Soares_DVCM
19 %Input_TwoPhase_Soares_DGCM
20 %Input_TwoPhase_Bergant_Low_DVCM
21 %Input_TwoPhase_Bergant_Low_DGCM
22 %Input_TwoPhase_Bergant_High_DVCM
23 %Input_TwoPhase_Bergant_High_DGCM
24
25 %% Calculating the size and number of the reaches and time steps.
26 % Travelling time for the pressure wave, from downstream to upstream
27 t_trav = L/a;
28 % Time step size [s]
29 dt = t_trav/Reaches;
30 % Maximum time [s]
31 t_max = 4*Oscillations*t_trav;
32 % Reach length (distance between nodes) [m]
33 dx = a*dt;
34 % Number of time steps [-]
35 n_t = round(t_max/dt + 1);
36 % Number of nodes [-]
37 n = round(L/dx + 1);
38
39 %% Calculating the weighting function for unsteady friction
40 W = 0;
41 switch Friction_Type
42     case 'Unsteady_Friction_Zielke'
43         W = WeightFuncZielke(viscosity ,dt,D,rho ,n_t);
44     case 'Unsteady_Friction_VardyBrown'
45         W = WeightFuncVardyBrown(viscosity , dt, D, rho, Re_0,n_t);
46     case 'Unsteady_Friction_Zarzycki'
47         W = WeightFuncZarzycki(viscosity , dt, D, rho, Re_0, n_t);
48 end
49
50 %% Solver
51 switch Solver
52     case '1D_SinglePhase'
```

```

53     Solver_SinglePhase
54     case '1D_TwoPhase_DVCM'
55         Solver_DVCM
56     case '1D_TwoPhase_DGCM'
57         Solver_DGCM
58 end
59
60 %% Displaying and storing the calculation time
61 toc
62 % Calculation time [s]
63 t_cal = toc;
64
65 %% Output
66 Output

```

INPUT

```

1 %% Choose Solver , Boundary Conditions , Wave Speed method and Friction Type
2 % Choose solver:
3 % 1)    1D_SinglePhase
4 % 2)    1D_TwoPhase_DVCM
5 % 3)    1D_TwoPhase_DGCM
6 Solver = '1D_TwoPhase_DGCM';
7
8 % Choose upstream boundary condition:
9 % 1)    Reservoir
10 Upstream_boundary = 'Reservoir';
11
12 % Choose downstream boundary condition:
13 % 1)    Valve_Instantaneous_Closure
14 % 2)    Valve_Transient_Closure
15 Downstream_boundary = 'Valve_Transient_Closure';
16
17 % Choose wave speed method: already known or need calculation:
18 % 1)    WaveSpeed_Known
19 % 2)    WaveSpeed_Calculate
20 WaveSpeed_Type = 'WaveSpeed_Calculate';
21
22 % Choose friction type:
23 % 1)    Prescribed_Steady_State_Friction (insert value in f_pre)
24 % 2)    Steady_State_Friction
25 % 3)    Quasi_Steady_Friction
26 % 4)    Unsteady_Friction_Brunone
27 % 5)    Unsteady_Friction_Zielke
28 % 6)    Unsteady_Friction_VardyBrown
29 % 7)    Unsteady_Friction_Zarzycki
30 Friction_Type = 'Unsteady_Friction_VardyBrown';
31
32 %% Mesh
33 % Number of divisions of the pipe [-]
34 Reaches = 48;
35 % One oscillation is four times the traveling time of the pressure wave [-]
36 Oscillations = 20;
37

```

```

38 %% Universal Constants
39 % Gravitational acceleration [m/s^2]
40 g = 9.8;
41
42 %% Pipe Dimensions and Parameters
43 % Length of pipe [m]
44 L = 15.22;
45 % Diameter of pipe [m]
46 D = 0.02;
47 % Cross sectional area of pipe [m^2]
48 A = pi * D^2/4;
49 % Thickness of pipe [m]
50 e = 0.001;
51 % Young's modulus [Pa]
52 E = 120E9;
53 % Absolute roughness [m]
54 roughness = 0.0015E-3;
55 % Poisson's ratio [-]
56 nu_p = 0.35;
57 % Angle of inclination [deg]
58 theta = 0;
59
60 %% Fluid Properties
61 % Density of water [kg/m^3]
62 rho = 998.2;
63 % Bulk modulus of water [Pa]
64 K = 2.2E9;
65 % Dynamic viscosity [kg/m*s]
66 viscosity = 1.002E-3;
67
68 switch Solver
69     case '1D_TwoPhase_DVCM'
70         % Vapour pressure in piezometric head [m]
71         H_vap = 0.10793;
72         % Barometric pressure head [m]
73         H_b = 101325/(rho*g);
74         % Vapour pressure in gauge piezometric head [m]
75         H_v = H_vap - H_b;
76     case '1D_TwoPhase_DGCM'
77         % Saturation pressure in piezometric head [m]
78         H_sat = 0.10793;
79         % Barometric pressure head [m]
80         H_b = 101325/(rho*g);
81         % Saturation pressure in gauge piezometric head [m]
82         H_v = H_sat - H_b;
83         % Void fraction at reference pressure [-]
84         alpha_0 = 1e-7;
85 end
86
87 %% Weighting factor for DVCM and DGCM
88 % Weighting factor [-]
89 psi = 0.55;
90
91 %% Flow Inputs

```

```

92 % Initial flow velocity [m/s]
93 u_0 = 0.156e-3/A;
94 % Initial volumetric flow rate [m^3/s]
95 Q_0 = u_0*A;
96 % Initial Reynolds number [-]
97 Re_0 = rho*u_0*D/viscosity;
98
99 %% Upstream reservoir / Initial head
100 % Height/pressure of the reservoir [m]
101 H_r = 46;
102
103 %% Downstream valve
104 % Closing time of valve [s]
105 t_c = 18/1000;
106
107 switch Downstream_boundary
108     case 'Valve_Instantaneous_Closure'
109         % Valve closure coefficient [-]
110         m = 0;
111     case 'Valve_Transient_Closure'
112         % Valve closure coefficient [-]
113         m = 5;
114 end
115
116 %% Wave speed – pure liquid
117 switch WaveSpeed_Type
118     case 'WaveSpeed_Calculate'
119         % Speed of the pressure wave [m/s]
120         a = WaveSpeed(e,D,K,rho,E,nu_p);
121     case 'WaveSpeed_Known'
122         % Speed of the pressure wave [m/s]
123         a = 1200;
124 end
125
126 %% Prescribed steady state friction coefficient (do not remove or hide)
127 % Prescribed steady state friction coefficient [-]
128 f_pre = 0;

```

WAVESPEED

```

1 function a = WaveSpeed(e, D, K, rho, E, nu_p)
2 %% Calculation of c_1
3 % The pipeline is anchored against longitudinal movement
4 if D/e < 25
5     % Constant [-]
6     c_1 = 2*e/D*(1 + nu_p) + D*(1-nu_p^(2))/(D + e);
7 else
8     % Coefficient [-]
9     c_1 = 1-nu_p^(2);
10 end
11
12 %% Calculation of the wave speed
13 % Wave speed [m/s]
14 a = sqrt(K/rho)/sqrt(1+(K*D/(E*e))*c_1);

```

15

16 end

WEIGHTINGFUNCVARDYBROWN

```
1 function W = WeightFuncVardyBrown(viscosity , dt , D , rho , Re_0 , n_t)
2 %% Vardy and Brown's weighting function
3 % Dimensionless time step [-]
4 dtau = 4*viscosity*dt/(D^2*rho);
5 % Constant [-]
6 A_star = 1/(2*sqrt(pi));
7 % Constant [-]
8 Kappa = log10(15.29*Re_0^(-0.0567));
9 % Constant [-]
10 B_star = Re_0^Kappa/12.86;
11
12 for j = 1:n_t-2
13     % Dimensionless time [-]
14     tau(j) = j*dtau - 0.5*dtau;
15     % Weighting function [-]
16     W(j) = A_star * exp(-B_star*tau(j))/sqrt(tau(j));
17 end
18 end
```

SOLVER SINGLEPHASE

```
1 %% Initialize matrices to reduce calculation time
2 % Volumetric flow rate [m^3/s]
3 Q(1:n,1:n_t) = 0;
4 % Piezometric head [m]
5 H(1:n,1:n_t) = 0;
6 % Time [s]
7 t(1:n_t) = 0;
8 % Height from datum [m]
9 z(1:n) = 0;
10 % Volumetric flow rate acceleration [m^3/s^2]
11 dQ(n,n_t-2) = 0;
12
13 %% Calculating the offset of each node from the datum (reference height)
14 % i indicate node number [-]
15 for i = 1:n
16     % Height from datum [m]
17     z(i) = (i-1)*dx*sind(theta);
18 end
19
20 %% Steady State
21 [Q, H] = SteadyState(Q_0, H_r, rho, D, viscosity, a, A, roughness, g,...
22     dx, Q, H, n, theta, Friction_Type, f_pre);
23
24 %% Transient flow
25 % j indicate time step number [-]
26 for j = 2:n_t
27     % Time [s]
28     t(j) = t(j-1) + dt;
```

```

29
30 %% Interior Nodes
31 for i = 2:n-1
32     [Q(i,j), H(i,j)] = InteriorNodes_SinglePhase(a, g, A, rho, D,...
33         viscosity, roughness, dx, theta, Q(i-1,j-1), H(i-1,j-1), ...
34         Q(i+1,j-1), H(i+1,j-1), Q, Re_0, i, j, dt, Friction_Type, ...
35         Q_0, f_pre, W, dQ, n_t);
36 end
37
38 %% Upstream Boundary
39 switch Upstream_boundary
40     case 'Reservoir'
41         [Q(1,j), H(1,j)] = Reservoir_Upstream(a, g, A, rho, D, dx, ...
42             viscosity, roughness, theta, Q(2,j-1), H(2,j-1), H_r, ...
43             Q, Re_0, i, j, dt, Friction_Type, Q_0, f_pre, W, dQ, n_t);
44     end
45
46 %% Downstream Boundary
47 switch Downstream_boundary
48     case 'Valve_Instantaneous_Closure'
49         [Q(n,j), H(n,j)] = Valve_Closure(a, g, A, D, dx, roughness, ...
50             rho, viscosity, t(j), t_c, m, theta, Q(n,1), H(n,1), ...
51             Q(n-1,j-1), H(n-1,j-1), Q, Re_0, i, j, dt, ...
52             Friction_Type, f_pre, W, dQ, n_t);
53     case 'Valve_Transient_Closure'
54         [Q(n,j), H(n,j)] = Valve_Closure(a, g, A, D, dx, roughness, ...
55             rho, viscosity, t(j), t_c, m, theta, Q(n,1), H(n,1), ...
56             Q(n-1,j-1), H(n-1,j-1), Q, Re_0, i, j, dt, ...
57             Friction_Type, f_pre, W, dQ, n_t);
58     end
59
60 %% Calculating the change in volumetric flow rate for unsteady friction
61 switch Friction_Type
62     case 'Unsteady_Friction_Zielke'
63         if j < n_t
64             dQ(:, n_t-j+1) = Q(:, j)-Q(:, j-1);
65         end
66     case 'Unsteady_Friction_VardyBrown'
67         if j < n_t
68             dQ(:, n_t-j+1) = Q(:, j)-Q(:, j-1);
69         end
70     case 'Unsteady_Friction_Zarzycki'
71         if j < n_t
72             dQ(:, n_t-j+1) = Q(:, j)-Q(:, j-1);
73         end
74     end
75 end

```

SOLVER DVCM

```

1 %% Initialize matrices to reduce calculation time
2 % Volumetric flow rate [m^3/s]
3 Q_u(1:n,1:n_t) = 0;
4 % Volumetric flow rate [m^3/s]

```

```

5 Q(1:n,1:n_t) = 0;
6 % Piezometric head [m]
7 H(1:n,1:n_t) = 0;
8 % Time [s]
9 t(1:n_t) = 0;
10 % Height from datum [m]
11 z(1:n) = 0;
12 % Volumetric flow rate acceleration [m^3/s^2]
13 dQ(n,n_t-2) = 0;
14 % Vapour cavity volume [m^3]
15 V_cav(1:n,1:n_t) = 0;
16
17 %% Calculating the offset of each node from the datum (reference height)
18 % i indicate node number [-]
19 for i = 1:n
20     % Height from datum [m]
21     z(i) = (i-1)*dx*sind(theta);
22 end
23
24 %% Steady State
25 [Q, H] = SteadyState(Q_0, H_r, rho, D, viscosity, a, A, roughness, g,...
26     dx, Q, H, n, theta, Friction_Type, f_pre);
27 Q_u(:,1) = Q(:,1);
28
29 %% Transient
30 % j indicate time step number [-]
31 for j = 2:n_t
32     % Time [s]
33     t(j) = t(j-1) + dt;
34
35     %% Interior Nodes
36     % The different formulaton for j = 2 and j > 2 is because Eq. 7.9
37     % requires a vapour cavity volume from two time steps back. However as
38     % there is no j = -1, the steady state values (j = 1) will be used for
39     % V_cav, Q, and Q_u in Eq. 7.9.
40     if j == 2
41         for i = 2:n-1
42             [Q_u(i,j), Q(i,j), H(i,j), V_cav(i,j)] = InteriorNodes_DVCM(...
43                 a, g, A, rho, D, viscosity, roughness, dx, theta,...
44                 Q(i-1,j-1), H(i-1,j-1), Q_u(i+1,j-1), H(i+1,j-1), Q,...
45                 Q_u, Re_0, i, j, dt, Friction_Type, Q_0, f_pre, W, dQ,...
46                 n_t, V_cav(i,j-1), V_cav(i,j-1), Q(i,j-1), Q_u(i,j-1),...
47                 psi, z(i), H_v);
48         end
49     else
50         for i = 2:n-1
51             [Q_u(i,j), Q(i,j), H(i,j), V_cav(i,j)] = InteriorNodes_DVCM(...
52                 a, g, A, rho, D, viscosity, roughness, dx, theta,...
53                 Q(i-1,j-1), H(i-1,j-1), Q_u(i+1,j-1), H(i+1,j-1), Q,...
54                 Q_u, Re_0, i, j, dt, Friction_Type, Q_0, f_pre, W, dQ,...
55                 n_t, V_cav(i,j-1), V_cav(i,j-2), Q(i,j-2), Q_u(i,j-2),...
56                 psi, z(i), H_v);
57         end
58     end

```

```

59
60 %% Upstream Boundary
61 switch Upstream_boundary
62     case 'Reservoir'
63         [Q(1,j), H(1,j)] = Reservoir_Upstream(a, g, A, rho, D, dx, ...
64             viscosity, roughness, theta, Q_u(2,j-1), H(2,j-1), H_r, ...
65             Q_u, Re_0, 1, j, dt, Friction_Type, Q_0, f_pre, W, dQ, n_t)
66         ;
67     end
68     Q_u(1,j) = Q(1,j);
69 %% Downstream Boundary
70 % Again, because there is no j = -1, the steady state values are used
71 % for V_cav, Q, and Q_u in Eq. 7.9.
72 if j == 2
73     switch Downstream_boundary
74         case 'Valve_Instantaneous_Closure'
75             [Q_u(n,j), Q(n,j), H(n,j), V_cav(n,j)] = Valve_Closure_DVCM
76                 (...
77                 a, g, A, D, dx, roughness, rho, viscosity, ...
78                 t(j), t_c, m, theta, Q(n,1), H(n,1), Q(n-1,j-1), ...
79                 H(n-1,j-1), Q, Re_0, n, j, dt, Friction_Type, f_pre, ...
80                 W, dQ, n_t, V_cav(n,j-1), V_cav(n,j-1), Q(n,j-1), ...
81                 Q_u(n,j-1), psi, z(n), H_v);
82         case 'Valve_Transient_Closure'
83             [Q_u(n,j), Q(n,j), H(n,j), V_cav(n,j)] = Valve_Closure_DVCM
84                 (...
85                 a, g, A, D, dx, roughness, rho, viscosity, ...
86                 t(j), t_c, m, theta, Q(n,1), H(n,1), Q(n-1,j-1), ...
87                 H(n-1,j-1), Q, Re_0, n, j, dt, Friction_Type, f_pre, ...
88                 W, dQ, n_t, V_cav(n,j-1), V_cav(n,j-1), Q(n,j-1), ...
89                 Q_u(n,j-1), psi, z(n), H_v);
90     end
91 else
92     switch Downstream_boundary
93         case 'Valve_Instantaneous_Closure'
94             [Q_u(n,j), Q(n,j), H(n,j), V_cav(n,j)] = Valve_Closure_DVCM
95                 (...
96                 a, g, A, D, dx, roughness, rho, viscosity, ...
97                 t(j), t_c, m, theta, Q(n,1), H(n,1), Q(n-1,j-1), ...
98                 H(n-1,j-1), Q, Re_0, n, j, dt, Friction_Type, f_pre, ...
99                 W, dQ, n_t, V_cav(n,j-1), V_cav(n,j-2), Q(n,j-2), ...
100                Q_u(n,j-2), psi, z(n), H_v);
101         case 'Valve_Transient_Closure'
102             [Q_u(n,j), Q(n,j), H(n,j), V_cav(n,j)] = Valve_Closure_DVCM
103                 (...
104                 a, g, A, D, dx, roughness, rho, viscosity, ...
105                 t(j), t_c, m, theta, Q(n,1), H(n,1), Q(n-1,j-1), ...
106                 H(n-1,j-1), Q, Re_0, n, j, dt, Friction_Type, f_pre, ...
107                 W, dQ, n_t, V_cav(n,j-1), V_cav(n,j-2), Q(n,j-2), ...
108                 Q_u(n,j-2), psi, z(n), H_v);
109     end
110 end

```

```

108     %% Calculating the change in volumetric flow rate for unsteady friction
109     switch Friction_Type
110         case 'Unsteady_Friction_Zielke'
111             if j<n_t
112                 dQ(:,n_t-j+1) = Q(:,j)-Q(:,j-1);
113             end
114         case 'Unsteady_Friction_VardyBrown'
115             if j<n_t
116                 dQ(:,n_t-j+1) = Q(:,j)-Q(:,j-1);
117             end
118         case 'Unsteady_Friction_Zarzycki'
119             if j<n_t
120                 dQ(:,n_t-j+1) = Q(:,j)-Q(:,j-1);
121             end
122     end
123 end

```

SOLVER DGCM

```

1  %% Initialize matrices to reduce calculation time
2  % Volumetric flow rate [m^3/s]
3  Q_u(1:n,1:n_t) = 0;
4  % Volumetric flow rate [m^3/s]
5  Q(1:n,1:n_t) = 0;
6  % Piezometric head [m]
7  H(1:n,1:n_t) = 0;
8  % Time [s]
9  t(1:n_t) = 0;
10 % Height from datum [m]
11 z(1:n) = 0;
12 % Volumetric flow rate acceleration [m^3/s^2]
13 dQ(n,n_t-2) = 0;
14 % Gas cavity volume [m^3]
15 V_g(1:n,1:n_t) = 0;
16
17 %% Calculating the offset of each node from the datum (reference height)
18 for i = 1:n
19     % Height from datum [m]
20     z(i) = (i-1)*dx*sind(theta);
21 end
22
23 %% Calculating the pipe volume associated to each node
24 % Volume associated to the node at the upstream boundary [m^3]
25 V_total(1,1) = A*dx/2;
26 % Volume associated to the individual interior nodes [m^3]
27 V_total(2:n-1,1) = A*dx;
28 % Volume associated to the node at the downstream boundary [m^3]
29 V_total(n,1) = A*dx/2;
30
31 %% Steady State
32 [Q, H, V_g] = SteadyState_DGCM(Q_0, H_r, rho, D, viscosity, a, A,...
33     roughness, g, dx, Q, H, n, theta, Friction_Type, f_pre, alpha_0,...
34     V_total, V_g, z, H_v);
35 Q_u(:,1) = Q(:,1);

```

```

36
37 %% Transient
38 % j indicate time step number [-]
39 for j = 2:n_t
40     % Time [s]
41     t(j) = t(j-1) + dt;
42
43 %% Interior Nodes
44 % The different formulaton for j = 2 and j > 2 is because Eq. 7.9
45 % requires a vapour cavity volume from two time steps back. However as
46 % there is no j = -1, the steady state values (j = 1) will be used for
47 % V_g, Q, and Q_u in Eq. 7.9.
48 if j == 2
49     for i = 2:n-1
50         [Q_u(i,j), Q(i,j), H(i,j), V_g(i,j)] = InteriorNodes_DGCM(...
51             a, g, A, rho, D, viscosity, roughness, dx, theta, ...
52             Q(i-1,j-1), H(i-1,j-1), Q_u(i+1,j-1), H(i+1,j-1), Q, ...
53             Q_u, Re_0, i, j, dt, Friction_Type, Q_0, f_pre, W, dQ, ...
54             n_t, H(i,1), alpha_0, V_total(i,1), V_g(i,j-1), Q(i,j-1)
55             , ...
56             Q_u(i,j-1), psi, z(i), H_v);
57     end
58 else
59     for i = 2:n-1
60         [Q_u(i,j), Q(i,j), H(i,j), V_g(i,j)] = InteriorNodes_DGCM(...
61             a, g, A, rho, D, viscosity, roughness, dx, theta, ...
62             Q(i-1,j-1), H(i-1,j-1), Q_u(i+1,j-1), H(i+1,j-1), Q, ...
63             Q_u, Re_0, i, j, dt, Friction_Type, Q_0, f_pre, W, dQ, ...
64             n_t, H(i,1), alpha_0, V_total(i,1), V_g(i,j-2), Q(i,j-2)
65             , ...
66             Q_u(i,j-2), psi, z(i), H_v);
67     end
68 %% Upstream Boundary
69 switch Upstream_boundary
70     case 'Reservoir'
71         [Q_u(1,j), Q(1,j), H(1,j), V_g(1,j)] = Reservoir_Upstream_DGCM
72             (...
73             a, g, A, rho, D, dx, viscosity, roughness, theta, ...
74             Q_u(2,j-1), H(2,j-1), H_r, Q_u, Re_0, 1, j, dt, ...
75             Friction_Type, Q_0, f_pre, W, dQ, n_t, H(1,1), alpha_0, ...
76             V_total(1,1), z(1), H_v);
77     end
78 %% Downstream Boundary
79 % Again, because there is no j = -1, the steady state values are used
80 % for V_g, Q, and Q_u in Eq. 7.9.
81 if j == 2
82     switch Downstream_boundary
83         case 'Valve_Instantaneous_Closure'
84             [Q_u(n,j), Q(n,j), H(n,j), V_g(n,j)] = Valve_Closure_DGCM
85                 (...

```

```

86         t(j), t_c, m, theta, Q(n,1), H(n,1), Q(n-1,j-1), ...
87         H(n-1,j-1), Q, Re_0, n, j, dt, Friction_Type, f_pre, ...
88         W, dQ, n_t, alpha_0, V_total(n,1), V_g(n,j-1), ...
89         Q(n,j-1), Q_u(n,j-1), psi, z(n), H_v);
90     case 'Valve_Transient_Closure'
91         [Q_u(n,j), Q(n,j), H(n,j), V_g(n,j)] = Valve_Closure_DGCM
92         (...
93         a, g, A, D, dx, roughness, rho, viscosity, ...
94         t(j), t_c, m, theta, Q(n,1), H(n,1), Q(n-1,j-1), ...
95         H(n-1,j-1), Q, Re_0, n, j, dt, Friction_Type, f_pre, ...
96         W, dQ, n_t, alpha_0, V_total(n,1), V_g(n,j-1), ...
97         Q(n,j-1), Q_u(n,j-1), psi, z(n), H_v);
98     end
99     else
100     switch Downstream_boundary
101     case 'Valve_Instantaneous_Closure'
102         [Q_u(n,j), Q(n,j), H(n,j), V_g(n,j)] = Valve_Closure_DGCM
103         (...
104         a, g, A, D, dx, roughness, rho, viscosity, ...
105         t(j), t_c, m, theta, Q(n,1), H(n,1), Q(n-1,j-1), ...
106         H(n-1,j-1), Q, Re_0, n, j, dt, Friction_Type, f_pre, ...
107         W, dQ, n_t, alpha_0, V_total(n,1), V_g(n,j-2), ...
108         Q(n,j-2), Q_u(n,j-2), psi, z(n), H_v);
109     case 'Valve_Transient_Closure'
110         [Q_u(n,j), Q(n,j), H(n,j), V_g(n,j)] = Valve_Closure_DGCM
111         (...
112         a, g, A, D, dx, roughness, rho, viscosity, ...
113         t(j), t_c, m, theta, Q(n,1), H(n,1), Q(n-1,j-1), ...
114         H(n-1,j-1), Q, Re_0, n, j, dt, Friction_Type, f_pre, ...
115         W, dQ, n_t, alpha_0, V_total(n,1), V_g(n,j-2), ...
116         Q(n,j-2), Q_u(n,j-2), psi, z(n), H_v);
117     end
118     end
119     %% Calculating the change in volumetric flow rate for unsteady friction
120     switch Friction_Type
121     case 'Unsteady_Friction_Zielke'
122         if j < n_t
123             dQ(:, n_t-j+1) = Q(:, j)-Q(:, j-1);
124         end
125     case 'Unsteady_Friction_VardyBrown'
126         if j < n_t
127             dQ(:, n_t-j+1) = Q(:, j)-Q(:, j-1);
128         end
129     case 'Unsteady_Friction_Zarzycki'
130         if j < n_t
131             dQ(:, n_t-j+1) = Q(:, j)-Q(:, j-1);
132         end
133     end
134 end

```

STEADYSTATE

```

1 function [Q, H] = SteadyState(Q_0, H_r, rho, D, viscosity, a, A, ...

```

```

2     roughness, g, dx, Q, H, n, theta, Friction_Type, f_pre)
3 %% Steady State Solver
4 % Volumetric flow rate [m^3/s]
5 Q(:,1) = Q_0;
6 % Piezometric head at reservoir [m]
7 H(1,:) = H_r;
8
9 % R is a resistance coefficient, which describes the friction at steady
10 % state where unsteady friction is zero.
11 switch Friction_Type
12     case 'Prescribed_Steady_State_Friction'
13         % Resistance coefficient [s^2/m^5]
14         R = f_pre*dx/(2*g*D*A^2);
15     otherwise
16         % Resistance coefficient [s^2/m^5]
17         R = ResistanceCoeff(g, D, A, dx, roughness, rho, Q_0, viscosity);
18 end
19
20 for i = 2:n
21     % Piezometric head, disregarding friction [m]
22     H_0 = H(i-1,1) - dx * sind(theta);
23     % Piezometric head [m]
24     H(i,1) = H_0 - R*Q_0*abs(Q_0) + dx/(a*A)*sind(theta)*Q_0;
25 end
26
27 end

```

STEADYSTATE DGCM

```

1 function [Q, H, V_g] = SteadyState_DGCM(Q_0, H_r, rho, D, viscosity, a,...
2     A, roughness, g, dx, Q, H, n, theta, Friction_Type, f_pre, alpha_0,...
3     V_total, V_g, z_P, H_v)
4 %% Steady State Solver
5 % Volumetric flow rate [m^3/s]
6 Q(:,1) = Q_0;
7 % Piezometric head at reservoir [m]
8 H(1,:) = H_r;
9
10 % R is a resistance coefficient, which describes the friction at steady
11 % state where unsteady friction is zero.
12 switch Friction_Type
13     case 'Prescribed_Steady_State_Friction'
14         % Resistance coefficient [s^2/m^5]
15         R = f_pre*dx/(2*g*D*A^2);
16     otherwise
17         % Resistance coefficient [s^2/m^5]
18         R = ResistanceCoeff(g, D, A, dx, roughness, rho, Q_0, viscosity);
19 end
20
21 for i = 2:n
22     % Piezometric head, disregarding friction [m]
23     H_0 = H(i-1,1) - dx * sind(theta);
24     % Piezometric head [m]
25     H(i,1) = H_0 - R*Q_0*abs(Q_0) + dx/(a*A)*sind(theta)*Q_0;

```

```

26 end
27
28 for i = 1:n
29     % Gas cavity volume [m^3]
30     V_g(i,1) = alpha_0*V_total(i,1);
31 end
32
33 end

```

INTERIORNODES SINGLEPHASE

```

1 function [Q_P, H_P] = InteriorNodes_SinglePhase(a, g, A, rho, D,...
2     viscosity, roughness, dx, theta, Q_A, H_A, Q_u_B, H_B, Q, Re_0, i, j
3     ,...
4     dt, Friction_Type, Q_0, f_pre, W, dQ, n_t)
5 %% Interior nodes
6 % Pipe constant [s/m^2]
7 B = PipeConst(a, g, A);
8 % Positive characteristics equation [m]
9 C_p = Characteristic_Plus(a, g, A, D, dx, roughness, rho, viscosity, ...
10     theta, Q_A, H_A, Q, Re_0, i, j, dt, Friction_Type, Q_0, f_pre, W, ...
11     dQ, n_t);
12 % Negative characteristics equation [m]
13 C_m = Characteristic_Minus(a, g, A, D, dx, roughness, rho, viscosity, ...
14     theta, Q_u_B, H_B, Q, Re_0, i, j, dt, Friction_Type, Q_0, f_pre, W, ...
15     dQ, n_t);
16 % Piezometric head [m]
17 H_P = (C_p + C_m)/2;
18 % Volumetric flow rate [m^3/s]
19 Q_P = (H_P - C_m)/B;
20 end

```

INTERIORNODES DVCM

```

1 function [Q_u_P, Q_P, H_P, V_cav_P] = InteriorNodes_DVCM(a, g, A, rho, ...
2     D, viscosity, roughness, dx, theta, Q_A, H_A, Q_u_B, H_B, Q, Q_u, ...
3     Re_0, i, j, dt, Friction_Type, Q_0, f_pre, W, dQ, n_t, V_cav_t, ...
4     V_cav_P0, Q_P0, Q_u_P0, psi, z_P, H_v)
5 %% Interior nodes
6 % Pipe constant [s/m^2]
7 B = PipeConst(a, g, A);
8 % Positive characteristics equation [m]
9 C_p = Characteristic_Plus(a, g, A, D, dx, roughness, rho, viscosity, ...
10     theta, Q_A, H_A, Q, Re_0, i, j, dt, Friction_Type, Q_0, f_pre, W, ...
11     dQ, n_t);
12 % Negative characteristics equation [m]
13 C_m = Characteristic_Minus(a, g, A, D, dx, roughness, rho, viscosity, ...
14     theta, Q_u_B, H_B, Q_u, Re_0, i, j, dt, Friction_Type, Q_0, f_pre, ...
15     W, dQ, n_t);
16
17 % Checking if a vapour cavity was present at the previous time step.
18 if V_cav_t > 0
19     %% Vapour cavity was present at the previous time step.
20     % Piezometric head [m]

```

```

21     H_P = z_P + H_v;
22     % Volumetric flow rate [m^3/s]
23     Q_u_P = (C_p - H_P)/B;
24     % Volumetric flow rate [m^3/s]
25     Q_P = (H_P - C_m)/B;
26     % Vapour cavity volume [m^3]
27     V_cav_P = V_cav_P0 + 2*dt*(psi*(Q_P - Q_u_P) + (1 - psi)*(Q_P0 - Q_u_P0
    ));
28
29     % Checking if the vapour cavity disappears.
30     if V_cav_P <= 0
31         %% Vapour cavity disappears because of a rise in head.
32         % Vapour cavity volume [m^3]
33         V_cav_P = 0;
34         % Piezometric head [m]
35         H_P = (C_p + C_m)/2;
36
37         if H_P < z_P + H_v
38             % Piezometric head [m]
39             H_P = z_P + H_v;
40         end
41
42         % Volumetric flow rate [m^3/s]
43         Q_u_P = (C_p - H_P)/B;
44         % Volumetric flow rate [m^3/s]
45         Q_P = Q_u_P;
46
47     end
48 else
49     %% No vapour cavity was present in the previous time step.
50     % Piezometric head [m]
51     H_P = (C_p + C_m)/2;
52
53     % Checking if the head falls below the level where vapour cavities are
    created.
54     if H_P <= z_P + H_v
55         %% Head fell below vapourization level.
56         % Piezometric head [m]
57         H_P = z_P + H_v;
58         % Volumetric flow rate [m^3/s]
59         Q_u_P = (C_p - H_P)/B;
60         % Volumetric flow rate [m^3/s]
61         Q_P = (H_P - C_m)/B;
62         % Vapour cavity volume [m^3]
63         V_cav_P = V_cav_P0 + 2*dt*(psi*(Q_P - Q_u_P) + (1 - psi)*(Q_P0 -
    Q_u_P0));
64
65     % Checking if a vapour cavity is created.
66     if V_cav_P <= 0
67         %% No vapour cavity is created.
68         % Vapour cavity volume [m^3]
69         V_cav_P = 0;
70         % Piezometric head [m]
71         H_P = (C_p + C_m)/2;

```

```

72
73         if H_P < z_P + H_v
74             % Piezometric head [m]
75             H_P = z_P + H_v;
76         end
77
78         % Volumetric flow rate [m^3/s]
79         Q_u_P = (C_p - H_P)/B;
80         % Volumetric flow rate [m^3/s]
81         Q_P = Q_u_P;
82
83     end
84 else
85     %% Head is above vapourization level.
86     % Vapour cavity volume [m^3]
87     V_cav_P = 0;
88     % Volumetric flow rate [m^3/s]
89     Q_u_P = (C_p - H_P)/B;
90     % Volumetric flow rate [m^3/s]
91     Q_P = Q_u_P;
92 end
93 end
94
95 end

```

INTERIORNODES DGCM

```

1 function [Q_u_P, Q_P, H_P, V_g_P] = InteriorNodes_DGCM(a, g, A, rho, D,...
2     viscosity, roughness, dx, theta, Q_A, H_A, Q_u_B, H_B, Q, Q_u, Re_0,...
3     i, j, dt, Friction_Type, Q_0, f_pre, W, dQ, n_t, H_0, alpha_0,...
4     V_total, V_g_P0, Q_P0, Q_u_P0, psi, z_P, H_v)
5 %% Interior nodes
6 % Pipe constant [s/m^2]
7 B = PipeConst(a, g, A);
8 % Positive characteristics equation [m]
9 C_p = Characteristic_Plus(a, g, A, D, dx, roughness, rho, viscosity,...
10     theta, Q_A, H_A, Q, Re_0, i, j, dt, Friction_Type, Q_0, f_pre, W,...
11     dQ, n_t);
12 % Negative characteristics equation [m]
13 C_m = Characteristic_Minus(a, g, A, D, dx, roughness, rho, viscosity,...
14     theta, Q_u_B, H_B, Q_u, Re_0, i, j, dt, Friction_Type, Q_0, f_pre, W
15     ,...
16     dQ, n_t);
17 %% Calculation of head - Fluid Transients in Systems
18 % Pressure at steady state [Pa]
19 P_0 = rho*g*(H_0 - z_P - H_v);
20 % Constant [m^4]
21 C_3 = P_0*alpha_0*V_total/(rho*g);
22 % Constant [-]
23 B_2 = 0.5/2;
24 % Constant [m^2]
25 C_4 = B_2*B*C_3/(psi*dt);
26 % Constant [m^3/s]

```

```

27 B_v = (V_g_P0/(2*dt) + (1 - psi)*(Q_P0 - Q_u_P0))/psi;
28
29 if B_v <= 0
30     % Constant [m^3/s]
31     B_v = 0;
32 end
33
34 % Constant [m/s]
35 B_1 = -B_2*(C_m + C_p) + B_2*B*B_v + (z_P + H_v)/2;
36
37 if B_1 == 0
38     % Piezometric head [m]
39     H_P = sqrt(C_4) + z_P + H_v;
40 else
41     % Constant [-]
42     B_B = C_4/B_1^2;
43
44     if B_1 < 0 && B_B > 0.001
45         % Piezometric head [m]
46         H_P = -B_1*(1 + sqrt(1 + B_B)) + z_P + H_v;
47     elseif B_1 > 0 && B_B > 0.001
48         % Piezometric head [m]
49         H_P = -B_1*(1 - sqrt(1 + B_B)) + z_P + H_v;
50     elseif B_1 < 0 && B_B < 0.001
51         % Piezometric head [m]
52         H_P = -2*B_1 - C_4/(2*B_1) + z_P + H_v;
53     elseif B_1 > 0 && B_B < 0.001
54         % Piezometric head [m]
55         H_P = C_4/(2*B_1) + z_P + H_v;
56     end
57 end
58
59 if H_P < z_P + H_v
60     % Piezometric head [m]
61     H_P = z_P + H_v;
62 end
63
64 %% Calculation of flows and vapour sizes
65 % Volumetric flow rate [m^3/s]
66 Q_u_P = (C_p - H_P)/B;
67 % Volumetric flow rate [m^3/s]
68 Q_P = (H_P - C_m)/B;
69 % Gas cavity volume [m^3]
70 V_g_P = V_g_P0 + (psi*(Q_P - Q_u_P) + (1-psi)*(Q_P0 - Q_u_P0))*2*dt;
71
72 if V_g_P < 0
73     % Gas cavity volume [m^3]
74     V_g_P = C_3/(H_P - z_P - H_v);
75 end
76
77 end

```

RESERVOIR UPSTREAM

```

1 function [Q_P, H_P] = Reservoir_Upstream(a, g, A, rho, D, dx,...
2     viscosity, roughness, theta, Q_B, H_B, H_r, Q, Re_0, i, j, dt,...
3     Friction_Type, Q_0, f_pre, W, dQ, n_t)
4 %% Boundary conditions for upstream reservoir
5 % Pipe constant [s/m^2]
6 B = PipeConst(a, g, A);
7 % Piezometric head [m]
8 H_P = H_r;
9 % Negative characteristics equation [m]
10 C_m = Characteristic_Minus(a, g, A, D, dx, roughness, rho, viscosity,...
11     theta, Q_B, H_B, Q, Re_0, i, j, dt, Friction_Type, Q_0, f_pre, W,...
12     dQ, n_t);
13 % Volumetric flow rate [m]
14 Q_P = (H_P - C_m)/B;
15 end

```

RESERVOIR UPSTREAM DGCM

```

1 function [Q_u_P, Q_P, H_P, V_g_P] = Reservoir_Upstream_DGCM(a, g, A,...
2     rho, D, dx, viscosity, roughness, theta, Q_u_B, H_B, H_r, Q_u, Re_0,...
3     i, j, dt, Friction_Type, Q_0, f_pre, W, dQ, n_t, H_0, alpha_0,...
4     V_total, z_P, H_v)
5 %% Boundary conditions for upstream reservoir
6 % Pipe constant [s/m^2]
7 B = PipeConst(a, g, A);
8 % Negative characteristics equation [m]
9 C_m = Characteristic_Minus(a, g, A, D, dx, roughness, rho, viscosity,...
10     theta, Q_u_B, H_B, Q_u, Re_0, i, j, dt, Friction_Type, Q_0, f_pre,...
11     W, dQ, n_t);
12 % Piezometric head [m]
13 H_P = H_r;
14 % Volumetric flow rate [m^3/s]
15 Q_P = (H_P - C_m)/B;
16 % Volumetric flow rate [m^3/s]
17 Q_u_P = Q_P;
18 % Pressure at steady state [Pa]
19 P_0 = rho*g*(H_0 - z_P - H_v);
20 % Constant [m^4]
21 C_3 = P_0*alpha_0*V_total/(rho*g);
22 % Gas cavity volume [m^3]
23 V_g_P = C_3/(H_P - z_P - H_v);
24 end

```

VALVE CLOSURE

```

1 function [Q_P, H_P] = Valve_Closure(a, g, A, D, dx, roughness, rho,...
2     viscosity, t, t_c, m, theta, Q_0, H_0, Q_A, H_A, Q, Re_0, i, j, dt,...
3     Friction_Type, f_pre, W, dQ, n_t)
4 %% Calculating the dimensionless closure time for the valve
5 if t < t_c
6     % Dimensionless valve closure time [-]
7     tau_v = 1 - (t/t_c)^m;
8 else
9     % Dimensionless valve closure time [-]

```

```

10     tau_v = 0;
11 end
12
13 %% Calculating the volumetric flow rate at the valve
14 % Pipe constant [s/m^2]
15 B = PipeConst(a, g, A);
16 % Positive characteristics equation [m]
17 C_p = Characteristic_Plus(a, g, A, D, dx, roughness, rho, ...
18     viscosity, theta, Q_A, H_A, Q, Re_0, i, j, dt, ...
19     Friction_Type, Q_0, f_pre, W, dQ, n_t);
20 % Variable [m^5/s^2]
21 C_v = (Q_0*tau_v)^2/(2*H_0);
22 % Volumetric flow rate [m^3/s]
23 Q_P = - B*C_v + sqrt((B*C_v)^2 + 2*C_v*C_p);
24
25 %% Calculation of the head
26 % Piezometric head [m]
27 H_P = C_p - B*Q_P;
28
29 end

```

VALVE CLOSURE DVCM

```

1 function [Q_u_P, Q_P, H_P, V_cav_P] = Valve_Closure_DVCM(a, g, A, D, dx, ...
2     roughness, rho, viscosity, t, t_c, m, theta, Q_0, H_0, Q_A, H_A, Q, ...
3     Re_0, i, j, dt, Friction_Type, f_pre, W, dQ, n_t, V_cav_t, V_cav_P0, ...
4     Q_P0, Q_u_P0, psi, z_P, H_v)
5 %% Calculating the dimensionless closure time for the valve
6 if t < t_c
7     % Dimensionless valve closure time [-]
8     tau_v = 1 - (t/t_c)^m;
9 else
10    % Dimensionless valve closure time [-]
11    tau_v = 0;
12 end
13
14 %% Calculating the volumetric flow rate at the valve
15 % Pipe constant [s/m^2]
16 B = PipeConst(a, g, A);
17 % Positive characteristics equation [m]
18 C_p = Characteristic_Plus(a, g, A, D, dx, roughness, rho, viscosity, ...
19     theta, Q_A, H_A, Q, Re_0, i, j, dt, Friction_Type, Q_0, f_pre, W, ...
20     dQ, n_t);
21 % Variable [m^5/s^2]
22 C_v = (Q_0*tau_v)^2/(2*H_0);
23 % Volumetric flow rate [m^3/s]
24 Q_P = - B*C_v + sqrt((B*C_v)^2 + 2*C_v*C_p);
25
26 %% Calculation of the head
27 % Checking if a vapour cavity was present at the previous time step.
28 if V_cav_t > 0
29     %% Vapour cavity was present at the previous time step.
30     % Piezometric head [m]
31     H_P = z_P + H_v;

```

```

32 % Volumetric flow rate [m^3/s]
33 Q_u.P = (C_p - H.P)/B;
34 % Vapour cavity volume [m^3]
35 V_cav.P = V_cav.P0 + 2*dt*(psi*(Q.P - Q_u.P) + (1 - psi)*(Q.P0 - Q_u.P0
    ));
36
37 % Checking if the vapour cavity disappears.
38 if V_cav.P <= 0
39     %% Vapour cavity disappears because of a rise in head
40     % Vapour cavity volume [m^3]
41     V_cav.P = 0;
42     % Volumetric flow rate [m^3/s]
43     Q_u.P = Q.P;
44     % Piezometric head [m]
45     H.P = C_p - B*Q.P;
46
47     if H.P < z.P + H_v
48         % Piezometric head [m]
49         H.P = z.P + H_v;
50     end
51 end
52 else
53 %% No vapour cavity was present in the previous time step
54 % Volumetric flow rate [m^3/s]
55 Q_u.P = Q.P;
56 % Piezometric head [m]
57 H.P = C_p - B*Q_u.P;
58
59 % Checking if the head falls below the level where vapour cavities are
60 created.
61 if H.P <= z.P + H_v
62     %% Head fell below vapourization level.
63     % Piezometric head [m]
64     H.P = z.P + H_v;
65     % Volumetric flow rate [m^3/s]
66     Q_u.P = (C_p - H.P)/B;
67     % Vapour cavity volume [m^3]
68     V_cav.P = V_cav.P0 + 2*dt*(psi*(Q.P - Q_u.P) + (1 - psi)*(Q.P0 -
        Q_u.P0));
69
70 % Checking if a vapour cavity is created.
71 if V_cav.P <= 0
72     %% No vapour cavity is created
73     % Vapour cavity volume [m^3]
74     V_cav.P = 0;
75     % Piezometric head [m]
76     H.P = C_p - B*Q.P;
77
78     if H.P < z.P + H_v
79         % Piezometric head [m]
80         H.P = z.P + H_v;
81     end
82

```

```

83         % Volumetric flow rate [m^3/s]
84         Q_u_P = Q_P;
85     end
86 else
87     %% Head is above vapourization level
88     % Vapour cavity volume [m^3]
89     V_cav_P = 0;
90 end
91 end
92
93 end

```

VALVE CLOSURE DGCM

```

1 function [Q_u_P, Q_P, H_P, V_g_P] = Valve_Closure_DGCM(a, g, A, D, dx,...
2     roughness, rho, viscosity, t, t_c, m, theta, Q_0, H_0, Q_A, H_A, Q,...
3     Re_0, n, j, dt, Friction_Type, f_pre, W, dQ, n_t, alpha_0, V_total,...
4     V_g_P0, Q_P0, Q_u_P0, psi, z_P, H_v)
5 %% Calculating the dimensionless closure time for the valve
6 if t < t_c
7     % Dimensionless valve closure time [-]
8     tau = 1 - (t/t_c)^m;
9 else
10    % Dimensionless valve closure time [-]
11    tau = 0;
12 end
13
14 %% Calculating the volumetric flow rate at the valve
15 % Pipe constant [s/m^2]
16 B = PipeConst(a, g, A);
17 % Positive characteristics equation [m]
18 C_p = Characteristic_Plus(a, g, A, D, dx, roughness, rho, viscosity,...
19     theta, Q_A, H_A, Q, Re_0, n, j, dt, Friction_Type, Q_0, f_pre, W,...
20     dQ, n_t);
21 % Variable [m^5/s^2]
22 C_v = (Q_0*tau)^2/(2*H_0);
23 % Volumetric flow rate [m^3/s]
24 Q_P = - B*C_v + sqrt((B*C_v)^2 + 2*C_v*C_p);
25
26 %% Calculation of the head
27 % Pressure at steady state [Pa]
28 P_0 = rho*g*(H_0 - z_P - H_v);
29 % Constant [m^4]
30 C_3 = P_0*alpha_0*V_total/(rho*g);
31 % Constant [-]
32 B_2 = 1/2;
33 % Constant [m^2]
34 C_4 = B_2*B*C_3/(psi*dt);
35 % Constant [m^3/s]
36 B_v = (V_g_P0/(2*dt) + (1 - psi)*(Q_P0 - Q_u_P0))/psi;
37
38 if B_v <= 0
39     % Constant [m^3/s]
40     B_v = 0;

```

```

41 end
42
43 % Constant [m/s]
44 B_1 = -B_2*(C_p - B*Q_P) + B_2*B*B_v + (z_P + H_v)/2;
45
46 if B_1 == 0
47     % Piezometric head [m]
48     H_P = sqrt(C_4) + z_P + H_v;
49 else
50     % Constant [-]
51     B_B = C_4/B_1^2;
52     if B_1 < 0 && B_B >= 0.001
53         % Piezometric head [m]
54         H_P = -B_1*(1 + sqrt(1 + B_B)) + z_P + H_v;
55     elseif B_1 > 0 && B_B >= 0.001
56         % Piezometric head [m]
57         H_P = -B_1*(1 - sqrt(1 + B_B)) + z_P + H_v;
58     elseif B_1 < 0 && B_B < 0.001
59         % Piezometric head [m]
60         H_P = -2*B_1 - C_4/(2*B_1) + z_P + H_v;
61     elseif B_1 > 0 && B_B < 0.001
62         % Piezometric head [m]
63         H_P = C_4/(2*B_1) + z_P + H_v;
64     end
65 end
66
67 if H_P < z_P + H_v
68     % Piezometric head [m]
69     H_P = z_P + H_v;
70 end
71
72 %% Calculation of flows and vapour sizes
73 % Volumetric flow rate [m^3/s]
74 Q_u_P = (C_p - H_P)/B;
75 % Gas cavity volume [m^3]
76 V_g_P = V_g_P0 + (psi*(Q_P - Q_u_P) + (1-psi)*(Q_P0 - Q_u_P0))*2*dt;
77
78 if V_g_P < 0
79     % Gas cavity volume [m^3]
80     V_g_P = C_3/(H_P - z_P - H_v);
81 end
82
83 end

```

CHARACTERISTIC PLUS

```

1 function C_p = Characteristic_Plus(a, g, A, D, dx, roughness, rho, ...
2     viscosity, alpha, Q_p, H_p, Q, Re_0, i, j, dt, Friction_Type, Q_0, ...
3     f_pre, W, dQ, n_t)
4 %% Calculation of the positive characteristics line.
5 % In "FrictionTerm", "Charact_Line" indicates whether the friction term is
6 % for the positive or the negative characteristics line.
7 Charact_Line = 'Plus';
8

```

```

9 % Pipe constant [s/m^2]
10 B = PipeConst(a, g, A);
11
12 % Friction term [m]
13 J = FrictionTerm(Friction_Type, D, roughness, rho, Re_0, Q_0, Q_p, Q,...
14     viscosity, A, i, j, dx, dt, Charact_Line, g, a, f_pre, W, dQ, n_t);
15
16 % Positive characteristics equation [m]
17 C_p = H_p + Q_p*(B + dx/(a*A)*sind(alpha)) - J;
18 end

```

CHARACTERISTIC MINUS

```

1 function C_m = Characteristic_Minus(a, g, A, D, dx, roughness, rho,...
2     viscosity, alpha, Q_m, H_m, Q, Re_0, i, j, dt, Friction_Type, Q_0,...
3     f_pre, W, dQ, n_t)
4 %% Calculation of the negative characteristics line.
5 % In "FrictionTerm", "Charact_Line" indicates whether the friction term is
6 % for the positive or the negative characteristics line.
7 Charact_Line = 'Minus';
8
9 % Pipe constant [s/m^2]
10 B = PipeConst(a, g, A);
11
12 % Friction term [m]
13 J = FrictionTerm(Friction_Type, D, roughness, rho, Re_0, Q_0, Q_m, Q,...
14     viscosity, A, i, j, dx, dt, Charact_Line, g, a, f_pre, W, dQ, n_t);
15
16 % Negative characteristics equation [m]
17 C_m = H_m + Q_m*(-B + dx/(a*A)*sind(alpha)) + J;
18 end

```

FRICTIONTERM

```

1 function [J] = FrictionTerm(Friction_Type, D, roughness, rho, Re_0, Q_0,...
2     Q_point, Q, viscosity, A, i, j, dx, dt, Charact_Line, g, a, f_pre,...
3     W, dQ, n_t)
4 % The friction term is comprised of three parts, steady state friction, J_s
5 % (only used by "Prescribed_Steady_State_Friction" and
6 % "Steady_State_Friction"), quasi-steady friction, J_q, and unsteady
7 % friction, J_u (for the unsteady friction models). These three are
8 % summarized after the calculation of each part.
9 switch Friction_Type
10     case 'Prescribed_Steady_State_Friction'
11         % Resistance coefficient [s^2/m^5]
12         R = f_pre*dx/(2*g*D*A^2);
13         J_s = R*Q_point*abs(Q_point);
14         J_q = 0;
15         J_u = 0;
16     case 'Steady_State_Friction'
17         % Darcy friction factor, determined for either laminar flow or via
18         % the Colebrook-White equation for turbulent flow [-]
19         f_s = FricFac(D, roughness, rho, Q_0, viscosity, A);
20         % Resistance coefficient [s^2/m^5]

```

```

21     R = f_s*dx/(2*g*D*A^2);
22     J_s = R*Q_point*abs(Q_point);
23     J_q = 0;
24     J_u = 0;
25 case 'Quasi-Steady-Friction'
26     % Darcy friction factor, determined for either laminar flow or via
27     % the Colebrook-White equation for turbulent flow [-]
28     f_q = FricFac(D, roughness, rho, Q_point, viscosity, A);
29     % Resistance coefficient [s^2/m^5]
30     R = f_q*dx/(2*g*D*A^2);
31     J_s = 0;
32     J_q = R*Q_point*abs(Q_point);
33     J_u = 0;
34 case 'Unsteady-Friction-Brunone'
35     % Darcy friction factor, determined for either laminar flow or via
36     % the Colebrook-White equation for turbulent flow [-]
37     f_q = FricFac(D, roughness, rho, Q_point, viscosity, A);
38     % Resistance coefficient [s^2/m^5]
39     R = f_q*dx/(2*g*D*A^2);
40     J_s = 0;
41     J_q = R*Q_point*abs(Q_point);
42     switch Charact_Line
43         case 'Plus'
44             J_u = BrunoneFricp(Q, Re_0, D, j, i, a, dt, dx,g,A);
45         case 'Minus'
46             J_u = BrunoneFricm(Q, Re_0, D, j, i, a, dt, dx,g,A);
47     end
48 case 'Unsteady-Friction-Zielke'
49     % Darcy friction factor, determined for either laminar flow or via
50     % the Colebrook-White equation for turbulent flow [-]
51     f_q = FricFac(D, roughness, rho, Q_point, viscosity, A);
52     % Resistance coefficient [s^2/m^5]
53     R = f_q*dx/(2*g*D*A^2);
54     J_s = 0;
55     J_q = R*Q_point*abs(Q_point);
56     switch Charact_Line
57         case 'Plus'
58             J_u = CBFricp(dt, j, i, D, rho, viscosity, g,A,a,W,dQ,n_t);
59         case 'Minus'
60             J_u = CBFricm(dt, j, i, D, rho, viscosity, g,A,a,W,dQ,n_t);
61     end
62 case 'Unsteady-Friction-VardyBrown'
63     % Darcy friction factor, determined for either laminar flow or via
64     % the Colebrook-White equation for turbulent flow [-]
65     f_q = FricFac(D, roughness, rho, Q_point, viscosity, A);
66     % Resistance coefficient [s^2/m^5]
67     R = f_q*dx/(2*g*D*A^2);
68     J_s = 0;
69     J_q = R*Q_point*abs(Q_point);
70     switch Charact_Line
71         case 'Plus'
72             J_u = CBFricp(dt, j, i, D, rho, viscosity, g,A,a,W,dQ,n_t);
73         case 'Minus'
74             J_u = CBFricm(dt, j, i, D, rho, viscosity, g,A,a,W,dQ,n_t);

```

```

75     end
76     case 'Unsteady_Friction_Zarzycki'
77         % Darcy friction factor, determined for either laminar flow or via
78         % the Colebrook-White equation for turbulent flow [-]
79         f_q = FricFac(D, roughness, rho, Q_point, viscosity, A);
80         % Resistance coefficient [s^2/m^5]
81         R = f_q*dx/(2*g*D*A^2);
82         J_s = 0;
83         J_q = R*Q_point*abs(Q_point);
84         switch Charact_Line
85             case 'Plus'
86                 J_u = CBFricp(dt, j, i, D, rho, viscosity, g,A,a,W,dQ,n_t);
87             case 'Minus'
88                 J_u = CBFricm(dt, j, i, D, rho, viscosity, g,A,a,W,dQ,n_t);
89         end
90     end
91     % Friction term [m]
92     J = J_s + J_q + J_u;
93 end

```

FRICFAC

```

1 function f = FricFac(D, roughness, rho, Q, viscosity, A)
2 %% Calculation of the Darcy friction factor.
3 % Reynolds number [-]
4 Re = rho*D*abs(Q)/(viscosity*A);
5
6 if Re==0
7     % Darcy friction factor for zero flow [-]
8     f = 1;
9 elseif Re>0 && Re<2100
10    %% Laminar flow
11    % Darcy friction factor for laminar flow [-]
12    f = 64/Re;
13 else
14    %% Colebrook-White equation
15    % The friction factor, f, is solved iteratively with ff being the
16    % initial
17    % value, and the accepted error being 1E-12. err is the error compared
18    % with the allow error, and the friction factor is only accepted when
19    % err becomes lower than 1E-12.
20    % Initializing ff [-]
21    ff = 10;
22    % Setting lower error limit [-]
23    err = 0.0001;
24    % Initializing Darcy friction factor [-]
25    f_old = 0;
26
27    while err > 1E-12
28        % Darcy friction factor for turbulent flow [-]
29        f = 1/ff^2;
30        % Result from Colebrook equation [-]
31        ff = -2*log10(roughness/(3.7*D)+2.51/(Re*sqrt(f)));

```

```

32     err = abs(f - f_old);
33     % Darcy friction factor for turbulent flow [-]
34     f_old = f;
35 end
36 end
37 end

```

BRUNONEFRICP

```

1 function h_up = BrunoneFricp(Q, Re, D, j, i, a, dt, dx, g, A)
2 %% Brunone's unsteady friction model
3 % Brunone's unsteady friction is calculated for the positive
4 % characteristics line.
5 if Re < 2100
6     % Vardy shear coefficient for laminar flow [-]
7     C = 0.00476;
8 else
9     % Vardy shear coefficient for turbulent flow [-]
10    C = 7.41/(Re^(log10(14.3/...
11        Re^0.05)));
12 end
13
14 % Brunone's friction coefficient [-]
15 k = sqrt(C)/2;
16
17 % For j = 2, there is no nodes two time steps, so it is not possible to
18 % calculate the acceleration of the volumetric flow rate. It is therefore
19 % set to zero, because two values from steady state would otherwise be
20 % used, which would result in zero for the acceleration term.
21 if j == 2
22     % Unsteady friction term [m]
23     h_up = a*dt*k/(g*A)*(a*sign(Q(i-1,j-1)) ...
24         *abs((Q(i,j-1)-Q(i-1,j-1))/dx));
25 else
26     % Unsteady friction term [m]
27     h_up = a*dt*k/(g*A)*((Q(i-1,j-1)-Q(i-1,j-2))/dt + a*sign(Q(i-1,j-1)) ...
28         *abs((Q(i,j-1)-Q(i-1,j-1))/dx));
29 end
30 end

```

BRUNONEFRICM

```

1 function J_u = BrunoneFricm(Q, Re, D, j, i, a, dt, dx, g, A)
2 %% Brunone's unsteady friction model
3 % Brunone's unsteady friction is calculated for the negative
4 % characteristics line.
5 if Re < 2100
6     % Vardy shear coefficient for laminar flow [-]
7     C = 0.00476;
8 else
9     % Vardy shear coefficient for turbulent flow [-]
10    C = 7.41/(Re^(log10(14.3/...
11        Re^0.05)));
12 end

```

```

13
14 % Brunone's friction coefficient [-]
15 k = sqrt(C)/2;
16
17 % For j = 2, there is no nodes two time steps, so it is not possible to
18 % calculate the acceleration of the volumetric flow rate. It is therefore
19 % set to zero, because two values from steady state would otherwise be
20 % used, which would result in zero for the acceleration term.
21 if j == 2
22     % Unsteady friction coefficient [m]
23     J_u = a*dt*k/(g*A)*(a*sign(Q(i+1,j-1))...
24         *abs((Q(i+1,j-1)-Q(i,j-1))/dx));
25 else
26     % Unsteady friction coefficient [m]
27     J_u = a*dt*k/(g*A)*((Q(i+1,j-1)-Q(i+1,j-2))/dt + a*sign(Q(i+1,j-1))...
28         *abs((Q(i+1,j-1)-Q(i,j-1))/dx));
29 end
30 end

```

CBFRICP

```

1 function J_u = CBFricp(dt, j, i, D, rho, viscosity, g,A,a,W,dQ,n_t)
2 %% Convolution based friction models
3 % The convolution based friction is calculated for the positive
4 % characteristics line (the weighting factor W(tau) defines if it is Vardy
5 % & Brown's unsteady friction model being used or another).
6 if j > 2
7     % Unsteady friction term [m]
8     J_u = 16*viscosity*dt*a*sum(dQ(i-1,n_t-j+2:n_t-1).*...
9         W(1,1:j-2))/(D^2*rho*A*g);
10 else
11     % Unsteady friction term [m]
12     J_u = 0;
13 end
14 end

```

CBFRICP

```

1 function J_u = CBFricp(dt, j, i, D, rho, viscosity, g,A,a,W,dQ,n_t)
2 %% Convolution based friction models
3 % The convolution based friction is calculated for the positive
4 % characteristics line (the weighting factor W(tau) defines if it is Vardy
5 % & Brown's unsteady friction model being used or another).
6 if j > 2
7     % Unsteady friction term [m]
8     J_u = 16*viscosity*dt*a*sum(dQ(i-1,n_t-j+2:n_t-1).*...
9         W(1,1:j-2))/(D^2*rho*A*g);
10 else
11     % Unsteady friction term [m]
12     J_u = 0;
13 end
14 end

```